DOCTOR OF PHILOSOPHY

Ultrafast Ionisation Dynamics Induced by Short Proton Pulses

Coughlan, Mark

Award date:
2018

Awarding institution:
Queen's University Belfast

Ultrafast Ionisation Dynamics Induced by Short Proton Pulses

A thesis presented upon application for admission to the degree of

Doctor of Philosophy

in the School of Mathematics and Physics by

Mark Edward Coughlan
MSci (Hons) 2013

Queen's University Belfast
Northern Ireland

July 31, 2018

Abstract

This work presents experimental results obtained using the TARANIS laser at Queen's University Belfast of transient absorption spectroscopy of dynamics induced by bursts of radiation, predominantly ions, from high-power laser-solid interactions. The absolute measurement of proton bursts as short as 3.7 ± 0.7 ps is reported, enabled by the ultrafast decay pathways available to excited electrons in the formation of self-trapped excitonic states.

The role of defects in the recovery of an induced opacity is examined in borosilicate glass. Here the recovery time of the opacity is measured to be orders of magnitude greater than the proton pulse duration, with a decay constant of over 550 ps. This long recovery time is attributed to the presence of interstitial energy levels due to defects created by the multicomponent structure of the glass.

Ultrafast pulsed-ion radiolysis is performed on H_2O to investigate the formation of solvated electrons. Significant delay in the formation of these aqueous electrons is observed to occur under proton irradiation compared to X-rays/electrons. Molecular Dynamics simulations suggest that this is due to the formation of nanoscale cavities around the proton track in the Bragg region due to the significantly higher energy deposition in this region that does not occur for X-rays and electrons.

The optical streaking technique is finally applied to investigate shifts in polarisation caused by irradiation of lithium niobate crystals. Two different oscillations are observed, firstly high frequency polarisation changes due to the arrival of relativistic electrons from the laser-target interaction followed by much lower frequency oscillations induced by the proton burst.

Contents

Chapter 1

Introduction

The aim of this thesis is to show that the short pulse durations and high degree of synchronicity between pump and probe pulses inherent to laser-driven ion acceleration allows the exploration of ionisation dynamics within condensed matter and liquid water, investigating the response of these materials to radiation on sub-nanosecond timescales.

Since the advent of the laser in the 1960s, a focus of research has been both to increase the power and reduce the duration of laser pulses [1–3]. Very short pulse durations have many benefits in science, not only does it allow for high laser intensities and the study of non-linear relativistic effects [4, 5], it also permits the observation of very short timescale interactions in matter through the use of probe pulses, either using the laser directly to observe transitions in biomolecules or from secondary radiation such as the short attosecond pulses developed through high harmonic generation schemes[6, 7]. In terms of radiation chemistry, there is much interest in understanding the effects of ionising radiation in matter – from cell recovery after undergoing hadron therapy in medicine to the damage caused to electrical components used for space technol-

ogy. Much of the work surrounding these areas focuses on the long term effects such as cell death or investigating the effect of radiation on structural integrity, but it is equally important to understand radiation reactions and their effects on much shorter timescales, be it the production of short lived reactive species in water, or the response of materials used in semiconductor technologies.

1.1 Pulsed Radiation Interactions with Matter

Understanding the effects of ionising radiation on matter has been a focus of research for many decades. In the past, many of these ion reaction studies have been performed in water using pulsed-ion radiolysis [8–10]. This technique typically involves the use of radio frequency (RF) particle accelerators in conjunction with the addition of chemical scavengers. There are however some drawbacks to this technique. Firstly, chemical scavenging requires the addition of substances which will react in some measurable way to the absorption of the ion energy such as photo-emission or the production of measurable reactive species. The addition of these substances is also not straightforward if one were to study the effect of radiation on solid matter. Secondly, for higher temporal resolution experiments, this technique has a high level of uncertainty as the concentration of scavenger required is at a level where the scavenger itself can take part in the radiolysis process [11, 12]. These measurements have also been limited by some of the pulse properties available from conventional RF accelerators; although they are capable of producing stable, high energy pulses, this is typically at the cost of long pulse durations with pulses shorter than 100 ps not routinely available [13]. Although there are still many hurdles to overcome, such as increasing the maximum proton energy and improving beam quality, laser-driven ion acceleration [14–16] has the advantage of offering significantly

shorter pulse durations with bunches in the order of a few picoseconds [17] with low transverse and longitudinal emittance [18]. The short pumping time enabled by these few-ps proton bunches allows for unprecedented observation of ultrafast dynamics within materials previously masked by longer interaction times.

Conversely for electrons, ultrashort pulses of GeV energy from linear accelerators are routinely achieved, with sub-picosecond high-energy (>150 MeV) electron beams emerging over the last few years [19]. However in both RF proton and electron generation schemes there is significant levels of timing jitter to optical probe pulses due to the electron/ion and probe sources being coupled electronically. Generating electron bunches through laser wakefield acceleration is an increasingly popular research field [20]. Using this technique high quality electron beams can be produced with GeV energy and few-femtosecond duration [21–23], however the main drawback to the use of electrons as an ionisation source compared to protons are in their interactions themselves with the material, such as the high degree of scattering the electrons will experience passing through the material. This will be discussed in greater detail in subsequent chapters.

1.2 Outline of Thesis

A brief outline of the chapters comprising this thesis is given below. Although in broad terms the work falls under one core experimental technique, the various materials examined exhibit widely different responses. The following chapters generally discuss one sort of material or response each.

Chapter 2 - High Power Laser-matter Interactions

This chapter provides an overview of the laser theory necessary for comprehension of the work contained in the subsequent thesis. An emphasis is placed on topics relevant to the generation of protons via Target Normal Sheath Acceleration. The chapter concludes with an overview of the core experimental method relevant to the thesis, any alterations to this method in relation to the study of other samples are discussed within their relevant chapters.

Chapter 3 - Ultrafast Recovery of SiO_2

Presented in this chapter are experimental results obtained measuring the pulse duration of the laser-driven proton burst. The ultrafast recovery of SiO_2 enabled an absolute measurement of 3.5 ± 0.7 ps. This measurement and the electron dynamics within irradiated SiO_2 is discussed along with methods of inhibiting this recovery, to this end a closer look at the ionisation dynamics in aerogel is included in the discussion.

Related publication:

- B. Dromey, **M. Coughlan**, L. Senje, M. Taylor, S. Kuschel, B. Villagomez-Bernabe, R. Stefanuik, G. Nersisyan,L. Stella, J. Kohanoff, M. Borghesi, F. Currell, D. Riley, D. Jung, C.-G. Wahlström, C.L.S. Lewis & M. Zepf, Picosecond metrology of laser-driven proton bursts, *Nature Communications*, 7:10642, DOI: 10.1038/ncomms10642, 2016.

Chapter 4 - Role of Defects in the Recovery of Borosilicate Glass

This chapter presents observations of a transient opacity in borosilicate glass (BK7), exposing the glass to similar few-ps proton bursts as in chapter 1, the

recovery of the material is orders of magnitude greater than the measured pulse duration. Possible mechanisms behind this result are discussed relating to the inhibition of the relaxation time for excited conduction band electrons.

Related work in preparation:

- **M. Coughlan**, L. Senje, M. Taylor, G. Nersisyan, D. Jung, H. Donnelly, N. Breslin, F. Currell, C.-G. Wahlström, L. Stella, J. Kohanoff, M. Zepf and B. Dromey, Ultrafast ion induced dynamics in borosilicate glass, 2018.

Chapter 5 - Observation of Solvated Electrons in Liquid Water

This chapter will focus on the formation of solvated electrons in liquid water after ionisation by protons. In comparison to the previous chapters focusing on solid samples, this work highlights the versatility of the optical streaking technique applying it to radiation chemistry investigations.

Related publication:

- L. Senje, **M. Coughlan**, D. Jung, M. Taylor, G. Nersisyan, C. L. S. Lewis, F. Currell, M. Zepf, and B. Dromey, Experimental investigation of picosecond dynamics following interactions between laser accelerated protons and water, *Appl. Phys. Lett.*, 110-104102, 2017.

Related work in preparation:

- **M. Coughlan**, L. Senje, H. Donnelly, N. Breslin, G. Nersisyan, F. Currell, C.-G. Wahlström, M. Zepf, B. Dromey, Electron solvation dynamics in H_2O during ultrafast pulsed-ion radiolysis, 2018.

Chapter 6 - Ionisation Dynamics of Lithium Niobate

Unlike the previous chapters, the response of Lithium Niobate to these few-ps proton pulses is profoundly different. This chapter discusses observations of ionisation induced dynamics on the response of Lithium Niobate to these short proton pulses.

Related work in preparation:

- **M. Coughlan**, H. Donnelly, N. Breslin, L. Senje, M. Taylor, G. Nersisyan, D. Jung, M. Zepf, B. Dromey, Induced polarisation shifts in lithium niobate when irradiated by few-picosecond proton pulses, 2018.

Chapter 7 - Conclusions and Outlook

A summary of the findings contained within this work are outlined in chapter 7 alongside a discussion of ideas for further developing the research topics covered in the previous chapters.

1.3 Role of the Author

The work presented in this thesis was predominantly obtained from experimental work. All of the experimental work and subsequent analysis was conducted under the supervision of Dr. B. Dromey and Prof. M. Zepf.

This thesis contains results obtained from a number of experiments carried out at Queen's University Belfast using the TARANIS laser facility between 2014 and 2017. On each of the experiments the author was part of a team with responsibilities that involved implementing the experimental setup, alignment

and optimisation of optical components and diagnostic apparatus, operation of CCD cameras alongside associated software, target alignment, sample preparation and other general day-to-day experimental duties. In particular the author ran the optical streaking diagnostic, development of the water cell and has led the analysis of the borosilicate glass, H_2O and $LiNbO_3$ samples.

Analysis of the proton pulse duration measurement in SiO_2 covered in chapter 3 was performed by Dr B. Dromey with contribution by the author. Analysis of data contained in the subsequent chapters was performed by the author under the supervision of Dr B. Dromey.

Chapter 2

Ions Accelerated from Ultrafast Laser-matter Interactions

The aim of this thesis is to report on investigations of proton-induced ionisation dynamics within various forms of matter. However, in order to provide a comprehensive report of the results contained within this work it is necessary to provide a background on key elements of theory relevant to the investigation of proton interactions with matter and ultrafast laser science. This chapter will introduce concepts and notation relating to laser-driven proton acceleration and short pulse laser-matter interactions.

Section 2.1 introduces a theoretical and historical background to obtaining the short, high-intensity laser pulses used in the generation of laser-driven protons, including energy transfer mechanisms between the laser pulse and generated plasma.

Section 2.2 and 2.3 provide a brief overview of the various forms of laser-driven ion acceleration with a focus on the target normal sheath acceleration mechanism used in the experiment. The latter section discusses how protons interact

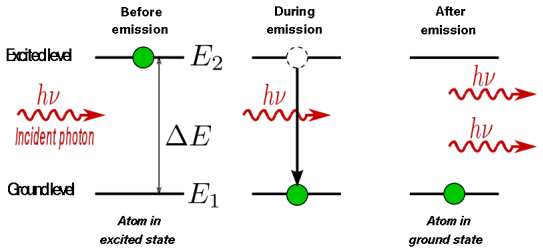

Figure 2.1: Diagram describing Stimulated Emission of Radiation

with matter and induce the ionisation dynamics which are observed in the material.

The core experimental technique is discussed in section 2.4, including an overview of the TARANIS laser facility where the experiments were performed. A discussion on the optical probing techniques is included alongside key concepts permitting the observation of these ionisation dynamics on ultrafast timescales.

2.1 Short-pulse Laser Technology

In 1916, Albert Einstein outlined the process of stimulated emission of radiation [24], a mechanism (shown in figure 2.1) which forms one of the fundamental basics for the operation of a laser. It wasn't until more than 40 years later however, that the first working laser was built by Theodore Maiman in 1960 [25] based on a ruby crystal. Laser pulse intensities have increased dramatically since then (as shown in figure 2.2). Within a decade following Maiman's first laser there was a rapid rise in laser intensity through the invention of Q-switching and mode-locking, peaking around $10^{15}\,\mathrm{W/cm^2}$ by the mid-1980s.

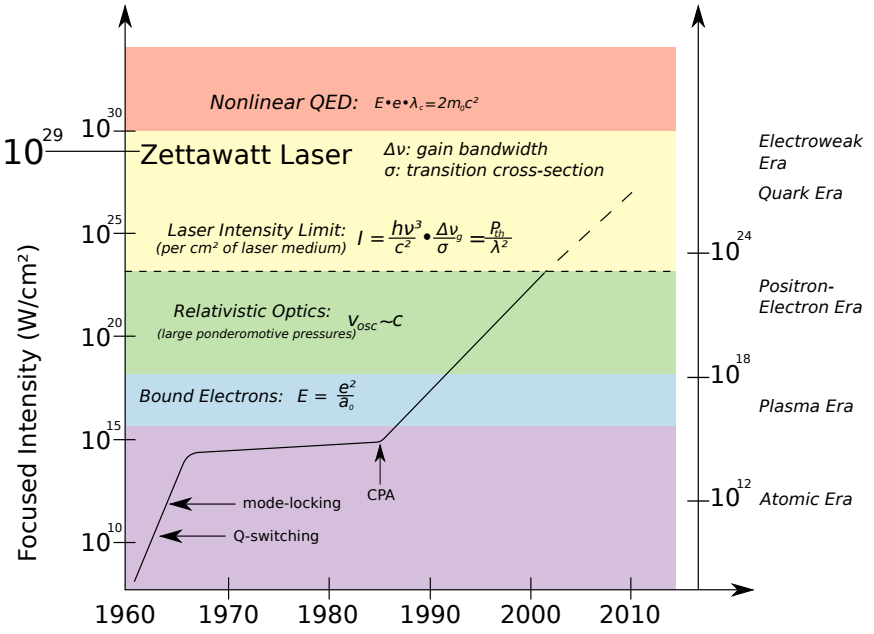

Figure 2.2: The progression of laser intensities achieved over the last several decades. Notable improvements were enabled through the introduction of Q-switching, mode-locking and chirped pulse amplification (Adapted from [26]).

2.1.1 Chirped Pulse Amplification (CPA)

As more progress was being achieved in laser development, it soon became clear that higher peak-power lasers were required to advance the field of research. Scientists were already using pulsing techniques to achieve what was then the highest intensities possible, however eventually the amplification rods were being damaged by a few pulses of the beam. Chirped pulse amplification was developed to overcome this issue and push pulsed intensities further. CPA was first demonstrated in 1975 by Strickland *et. al.* [27], based on a similar technique originally used to enhance radar transmission [28]. A schematic showing general layout of a CPA laser is shown in figure 2.3.

The main principle of CPA involves stretching a short, sub-picosecond pulse to around a nanosecond before being amplified. This allows much greater powers to be achieved by avoiding damage to the optical components. The pulse is

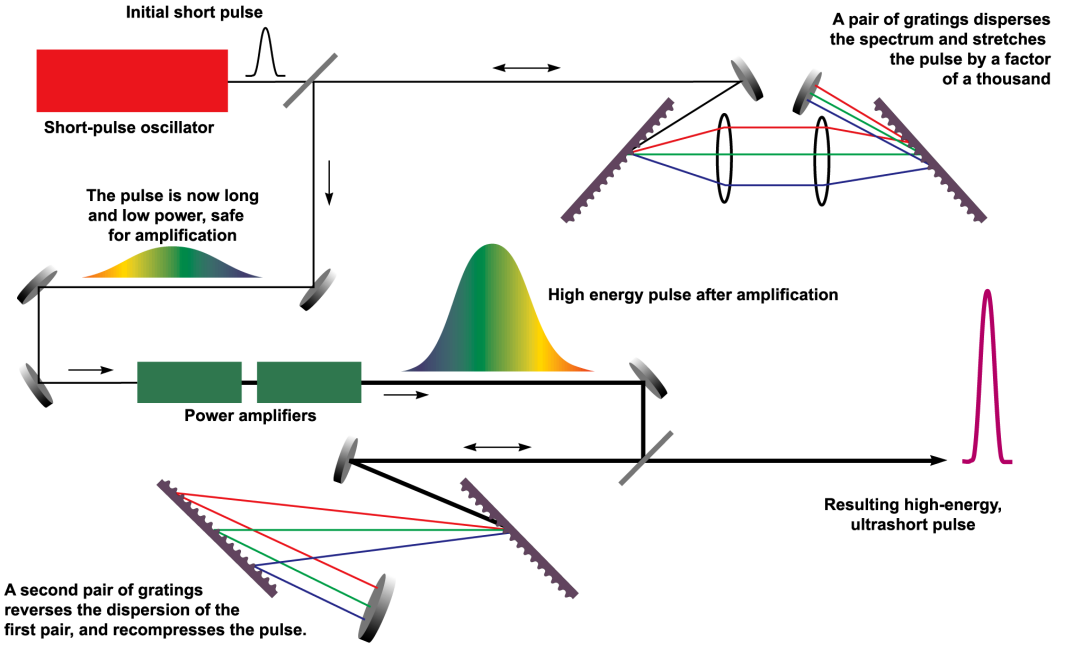

Figure 2.3: Sketch of the typical components of the CPA technique. Modified version from [29].

stretched using a pair of diffraction gratings, where longer wavelengths emerge before shorter wavelengths, therefore travelling different distances and stretching the pulse in time. In this configuration the laser is said to be 'chirped'. The stretched pulse is now able to travel through the amplifier without risk of damage to the rod. After amplification, the chirped pulse is compressed in a process opposite to the stretcher, which again results in a short pulse, comparable in length to its original duration. Since the advent of CPA, laser intensities have been increasing by a factor of ten every few years, now laser systems are capable of producing beams containing tens of joules in a few tens of femtoseconds, enabling peak powers in the petawatt region with intensities of around 10^{21} Wcm^{-2}.

2.1.2 Laser-plasma Absorption Processes

This section will discuss absorption processes related to the generation of proton bursts via laser-solid interactions. A plasma is typically modelled as consisting of ions and free electrons, however as current laser intensities are still not sufficient for their electric fields to act directly on the plasma ions, energy transfer processes occur through interaction with the electrons in the plasma. Generally electrons will be excited by an intense laser field and transfer their energy to the plasma via collisions. The intensity of a laser is usually described by the normalised vector potential a_0,

$$a_0 = \frac{v_{max}}{c} = \frac{eA_0}{\omega m_e c^2} \tag{2.1}$$

where A is the vector potential of the laser field and the other symbols have their usual definitions. When $a_0 > 1$ the interaction is treated relativistically as the velocity of the electron approaches the speed of light, however in experiments the electric field of the laser is not usually measured directly, intensity of the laser pulse is instead calculated based on a measured focal spot size, pulse duration and energy. The intensity of the wave can be expressed more easily for experimental purposes using the magnitude of the Poynting vector $\mathbf{S}$, which represents the directional energy flux density of an electromagnetic wave,

$$\mathbf{S} = \frac{1}{\mu_0}\mathbf{E} \times \mathbf{B} \tag{2.2}$$

where μ_0 is the vacuum permeability, $\mathbf{E}$ is the electric field and $\mathbf{B}$ is the magnetic field. As it is an electromagnetic wave, $\mathbf{E} \perp \mathbf{B}$ and through substitution using Maxwell's equations $\mathbf{E}$=$\mathbf{B}$/c the magnitude of the cycle-averaged Poynting

vector becomes

$$\langle \mathbf{S} \rangle = \frac{1}{2} \epsilon_0 c E_0^2 = I \tag{2.3}$$

which links amplitude of the electric field to the intensity of the laser I. After substituting with equation 2.1, the laser intensity can now be expressed as

$$I_0 \lambda^2 \approx \left[1.37 \times 10^{18} \frac{\mathrm{W}}{\mathrm{cm}^2} \mu\mathrm{m}^2 \right] a_0^2 \tag{2.4}$$

Resonance Absorption

At oblique laser incidence, there will be a component of the electric field vector that drives electron oscillations along the direction of the plasma density gradient. This oscillation will create fluctuations in the local charge density which allows the laser to drive these oscillations resonantly where the laser frequency matches the plasma frequency. An electron plasma wave is then driven into the plasma and the energy from this wave is absorbed by the plasma through collisions or wave-breaking [30, 31].

Vacuum (Brunel) Heating

For steep plasma gradients, where the amplitude of the electron oscillations are greater than the plasma scale length, resonance absorption will no longer apply. Introduced by Brunel in 1987 [32], vacuum heating involves electrons at the edge of a steep plasma-vacuum interface being accelerated by the laser field into the vacuum. When the laser field reverses a half-cycle later, the electrons are driven back into the plasma. However, they are now screened to the effects

of the driving laser pulse by the plasma and can therefore travel deeper without being dragged out again by the laser field and will then go on to take part in collisions with atoms and ions to heat the plasma [33].

$\mathbf{j} \times \mathbf{B}$ Heating

In the $\mathbf{j} \times \mathbf{B}$ heating regime, electrons are directly accelerated by the laser field. At relativistic intensities ($a_0 \geq 1$) the electron motion is dominated by the $\mathbf{v} \times \mathbf{B}$ term of the lorentz force equation

$$f_x = -\frac{m_e}{4}\frac{\partial v^2(x)}{\partial x}(1 - \cos(2\omega t)) \tag{2.5}$$

where the first term describes the electron motion in the direction of laser propagation and the second under the fast oscillating vector potential. It is important to note that this force will always act in the forward direction and $\mathbf{j} \times \mathbf{B}$ heating is mostly independent of the laser polarisation, except for circularly polarised light where it will no longer work due to the lack of a fast oscillating component to the electric field.

2.2 Laser-driven Ion Acceleration

As previously discussed in chapter 1, the accelerating field of a conventional RF accelerator is ultimately limited by the dielectric breakdown of the materials making up the acceleration tube, which places a limit on the acceleration that can be applied over a given area. To avoid this breakdown, electric fields are limited to around 100 MV/m [34], which leads to the very long accelerators required to reach high particle energies.

Alternatively, ion acceleration using high-intensity laser pulses has been an active area of research spanning several decades. Many theoretical mechanisms have been introduced over these years, some of which have been verified experimentally. As current laser intensities are not yet capable of directly accelerating protons (from equations 2.1 and 2.4 requires $a_0 \approx 2000$ or intensities $I_0\lambda^2 > 10^{24}\,\mathrm{Wcm^{-2}\mu m^2}$) [33], most mechanisms are therefore a result of charge separation, where strong electric fields are generated by electrons when they are separated from the plasma ions due to the ponderomotive force of the laser. These accelerating fields can reach several $\mathrm{TV\,m^{-1}}$, orders of magnitude greater than conventional RF accelerators.

This section is mainly concerned with the Target Normal Sheath Acceleration (TNSA) mechanism as it was used solely in this body of work, however a brief overview of other methods and their unique characteristics will also be included.

2.2.1 Target Normal Sheath Acceleration (TNSA)

Target Normal Sheath Acceleration (TNSA) is a laser-driven ion acceleration method that uses the laser pulse to indirectly accelerate protons from a foil target. First outlined in 1986 by Gitomer *et. al.* at the Los Alamos National Laboratory [35], the technique was developed further in the early 2000s [17, 18, 36]. Initial experiments found that most of the ions detected by the spectrometer were protons, which did not change when using different target materials. This was later attributed to the presence of a thin layer of hydrocarbon contaminants on the surface of the target, originating either from an oil coating caused by the vacuum pump or water vapour in the target chamber. It was concluded that the fast protons were caused by the presence of hot electrons, created by the interaction of the laser beam with the target surface.

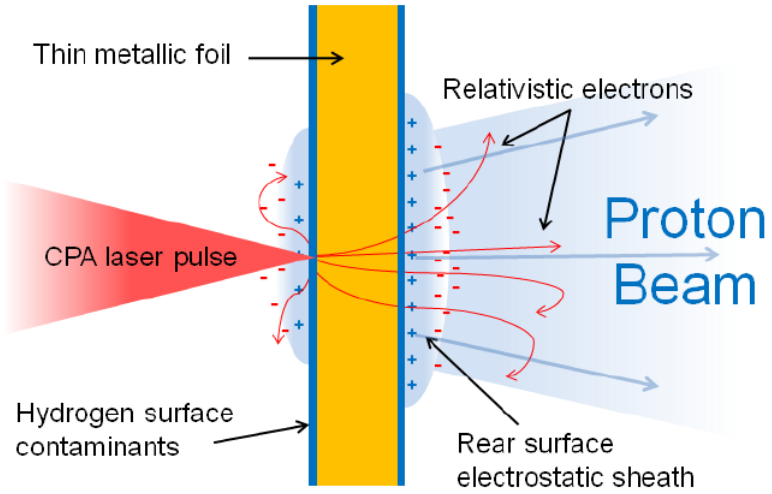

Figure 2.4: Proton acceleration via target normal sheath acceleration. Taken from [37].

When an intense ($10^{18}\,\mathrm{W\,cm^{-2}}$) laser pulse interacts with a few µm thick solid target. The front side of the target is rapidly ionised to form an expanding plasma which partially absorbs the main pulse to create hot electrons through resonance absorption and $\mathbf{j}\times\mathbf{B}$ heating. The electrons are accelerated to relativistic energies and pass through the target foil to form an electric cloud or "sheath" on the rear side. A charge separation is formed, creating a high electric field also called a sheath field, normal to the rear surface. The induced charge separation field has a typical length of a few microns with a strength of several $\mathrm{TV\,m^{-1}}$ [38–40]. A schematic of this process is shown in figure 2.4. The hydrogen ions (protons), usually from surface contaminants, have the highest charge/mass ratio of the plasma ions and are most effectively accelerated by the strong electric fields produced, causing the ions to be accelerated over a length of a few microns normal to the rear surface of the target [37]. As the accelerated ions originate from the cold, unirradiated side of the target, the resulting proton burst has a very low transverse and longitudinal emittance, of the order of < 0.004 mm mrad and $< 10^{-4}$ eV s respectively [41].

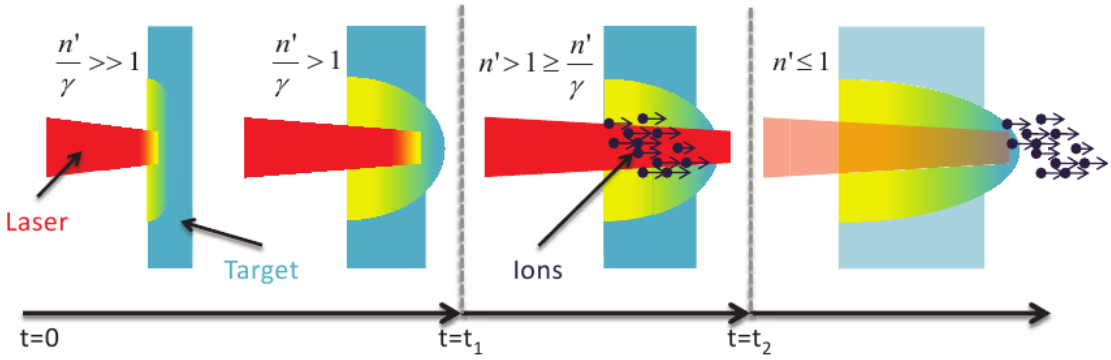

Figure 2.5: Diagram illustrating Break-out Afterburner process. Taken from [42]. Before t=t_1 the target is volumetrically heated, all electrons become hot. After t=t_1 the target becomes relativistically transparent to the laser and continuously transfers energy to the hot electrons, maintaining the charge separation field.

2.2.2 Break-out Afterburner (BOA)

BOA was first identified using particle-in-cell (PIC) simulations by Yin *et. al.* [43]. In the BOA regime the target is rapidly ionised by the laser and similarly to TNSA, relativistic electrons are produced that travel through the target to form a sheath field on the rear side. However, in contrast to TNSA, where the laser energy is absorbed by electrons in a small volume at the surface of the target, in the BOA regime the target becomes relativistically transparent to the laser light. This enables the rapid heating of electrons in the total volume beneath the laser spot [44]. This rapid heating also results in self-cleaning of the target - removing the surface contaminants that would normally be accelerated as protons in TNSA. If the target is sufficiently thin (nm-scale), the laser will accelerate all electrons to relativistic energies, therefore the electric field experienced by the ions due to the space charge separation is significantly higher than that of TNSA, causing the ions to be accelerated to much higher energies.

2.2.3 Radiation Pressure Acceleration (RPA)

Simulations show that for laser intensities above 10^{23} W/cm^{-2} TNSA is no longer the dominant acceleration and may be replaced by RPA. When the high-intensity pulse interacts with an ultrathin (<100 nm) target, the ponderomotive pressure of the laser pulse sustains a charge separation capable of rapidly accelerating ions [15, 45, 46]. Although these intensities are currently unobtainable with today's laser technology, studies have shown that the use of a circularly polarised laser pulse will suppress the generation of hot electrons necessary for TNSA [47] due to the lack of a fast oscillating component of the ponderomotive force, this would result in the electrons instead being adiabatically compressed by the slowly varying ponderomotive force of the laser. The compression layer will eventually reach the end of the target and the whole volume under the laser focus will be accelerated as a single plasma slab to approximately the same final velocity. The main advantages of RPA when compared with TNSA would lie in the much shorter ion bunch durations (tens of femtoseconds) [45] and monoenergetic beams with higher conversion efficiency from the laser to ion energy [15].

2.3 Proton Interactions with Matter

The deposition of energy by heavy particles has certain unique properties compared to gamma or electron radiation. X-rays, for example, will typically deposit most of their energy at the surface of a material and then gradually lose energy. Protons and other heavy particles interact through electronic collisions and lose more and more energy as they slow down in the material. This results in their characteristic dose deposition profile (shown in figure 2.6 for 250 MeV

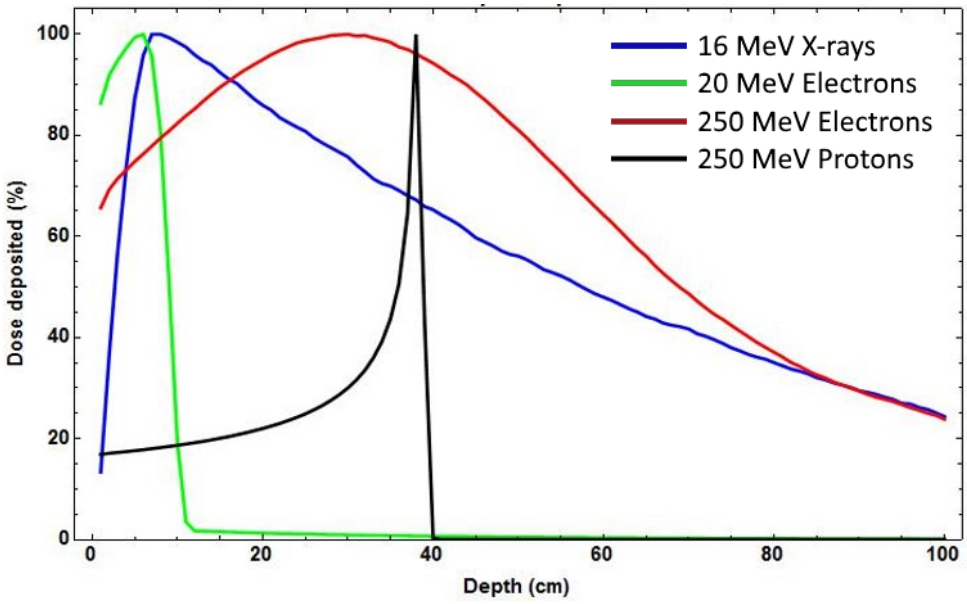

Figure 2.6: Dose-depth curves for various forms of radiation in water. Adapted version from [48].

protons) and they will deposit a small amount of energy until close to the end of their range in the material, as their velocity decreases they undergo a larger amount of electronic interactions resulting in a large deposition of dose in a small volume. This region is known as the Bragg peak and can be controlled by changing the initial energy of the particles, it has many benefits in cancer treatment as it enables a high dose to be delivered to the cancerous cells while also minimising damage to surrounding healthy tissue.

2.3.1 Energy Loss Mechanisms

Generally there are two processes by which particles lose energy in a material. This is highlighted in figure 2.6. The first is a catastrophic energy loss, where the particle will deposit all of it's energy in a single collision, resulting in a high dose near (or at) the surface of the material, in the figure this is represented by X-rays and electrons. Heavier particles however, experience a more gradual

energy loss as they continuously lose energy as the particle moves through the material. This section will discuss the latter, looking at how protons transfer energy to the media they are interacting with.

Stopping Power

Stopping power an important term in radiation physics and describes the energy lost by a charged particle as it passes through a material. It is equal to the loss of energy E per unit length x

$$S(E) = \frac{dE}{dx} \tag{2.6}$$

The total stopping of a charged particle is the sum of the energy lost over a unit distance caused by its interactions with electrons, nuclei and other radiative energy losses. Electronic stopping involves the slowing down of an ion due to inelastic collisions between the ion and electrons in the material, it is dominant for a wide energy range and will be the focus of this section. Nuclear stopping is negligible except for at very low energy ($< 1\,\mathrm{MeV}$) and radiative loss does not dominate until GeV proton energies [49, 50].

In general charged particles interact and lose energy via Coulomb interactions, Figure 2.7 shows illustrations of various proton interaction mechanisms which will be discussed in this section in slightly more detail.

Coulomb Interactions

The most common form of energy loss at non-relativistic energies involves electromagnetic interaction between the proton and the atoms in the material,

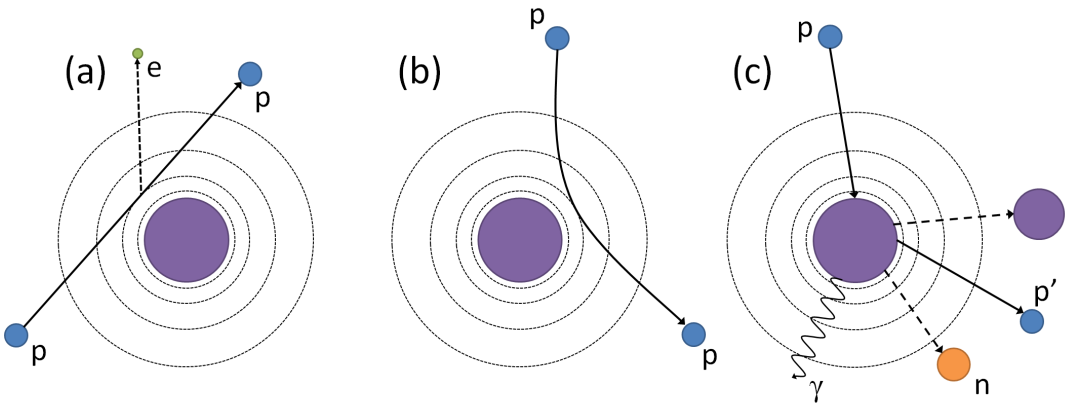

Figure 2.7: Schematic of various energy loss mechanisms of protons. (a) Inelastic Coulomb interaction, (b) Elastic Coulomb scattering, (c) Inelastic interaction with nucleus and generation of secondary particles. Adapted version of [51].

Coulomb interactions form the core mechanism behind the slowing of a charged particle as it moves through a material and can be separated into two categories.

Inelastic scattering (outlined in figure 2.7a) involves transfer of energy between the proton and electron through collisions or the Coulomb force. As the Coulomb force can act over a distance it is not necessary for the proton to make a direct collision with the electron to impart energy on it, however the result is the same. Some energy may be transferred to the electron to excite it to a higher energy state but if enough energy is transferred, the electron can be removed from its orbital and the atom becomes ionised, this mechanism is responsible for the quasi-continuous energy loss of the proton as it travels in the material.

Elastic scattering describes coulomb interactions between the proton and the nucleus of the atom (a sketch is shown in figure 2.7b) Due to the range of the Coulomb force, energy transfers from the proton to the nucleus resulting in a change in the trajectory of the proton.

Nuclear Interactions involve collisions with the atomic nuclei (as shown in figure 2.7) however at non-relativistic energies these collisions are quite rare and do not contribute much to the total energy loss [52].

2.3.2 Proton Range and Straggling

The range of a proton in matter depends on its initial energy and the material itself that the proton is passing through and can be calculated by integrating the reciprocal of the stopping power in equation 2.6

$$\Delta x = \int_0^{E0} \frac{1}{S(E)} dE \tag{2.7}$$

The energy lost by a 10 MeV proton as function of its distance into a borosilicate glass sample is shown in figure 2.8. As the proton nears the end of its trajectory, the energy loss reaches a maximum and then near-instantly drops to zero. This maximum is referred to as the Bragg peak, in this case it lies at approximately 600 µm into the BK7 glass. Not all 10 MeV protons will travel exactly the same distance into the glass however. Due to the statistical nature of collisions, some protons will undergo more than others, experiencing a slight change in their energy loss or trajectory resulting in a fluctuation in the range, known as straggling. This effect is highlighted in figure 2.9 where Energy-Depth curves are plotted for approximately 10,000 protons with an initial energy of 10 MeV.

Initially all of the protons have the same starting energy and trajectory, however as they propagate into the glass, they begin to lose energy at different rates, this results in a spreading of the bunch in time as protons will begin to reach a specific depth at slightly different times. Towards the end of their trajectory the pulse width has broadened to > 2 ps due to the straggling alone.

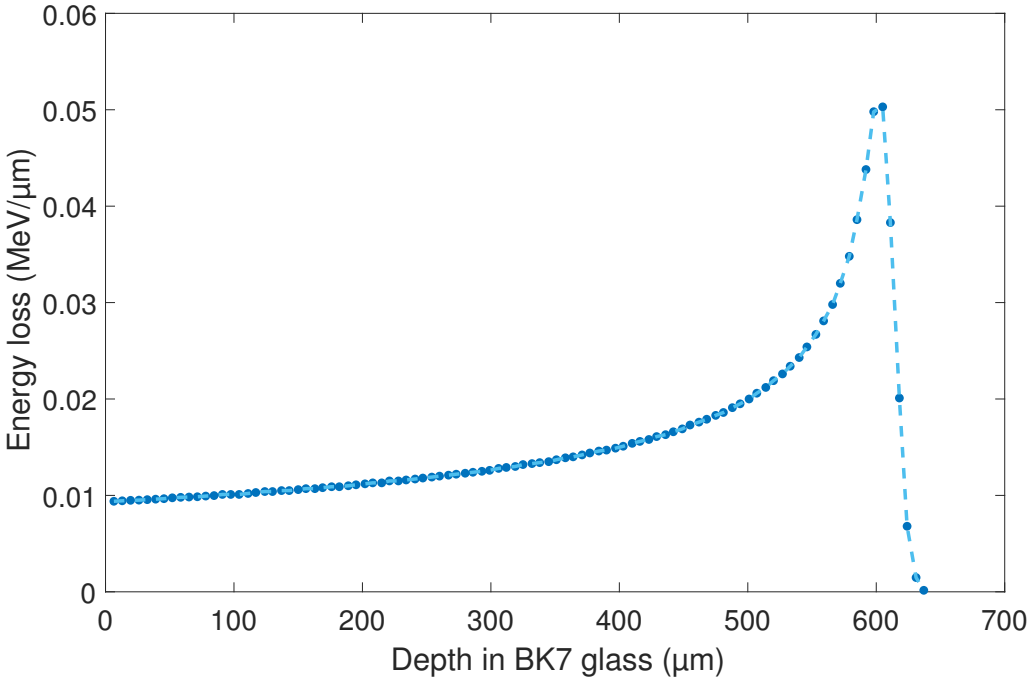

Figure 2.8: Plot showing the energy lost by 10 MeV protons as they propagate into a BK7 glass sample with the characteristic Bragg peak located at approximately 600 µm. Proton stopping data was obtained through calculations using SRIM [53].

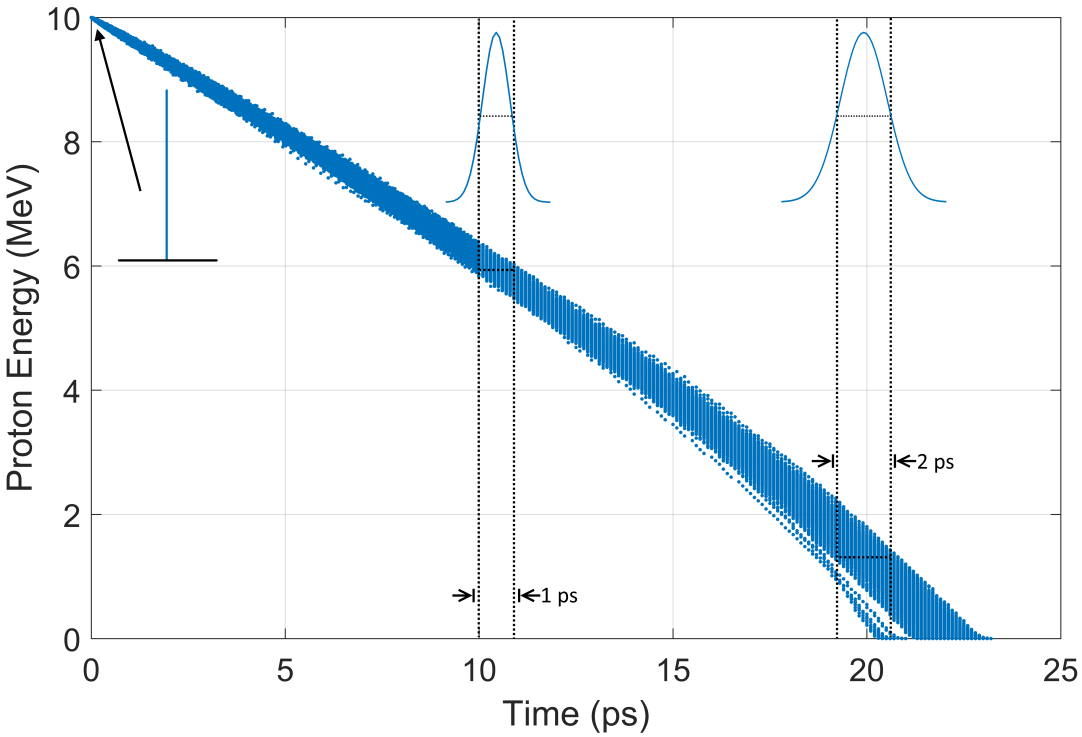

Figure 2.9: This plot uses data obtained from SRIM calculations to show the temporal spreading of the pulse due to straggling within the sample. As all protons start with the same initial properties (energy, position e.t.c) the pulse expands from a theoretical delta spike to $> 2\,\mathrm{ps}$ as it propagates through the glass sample.

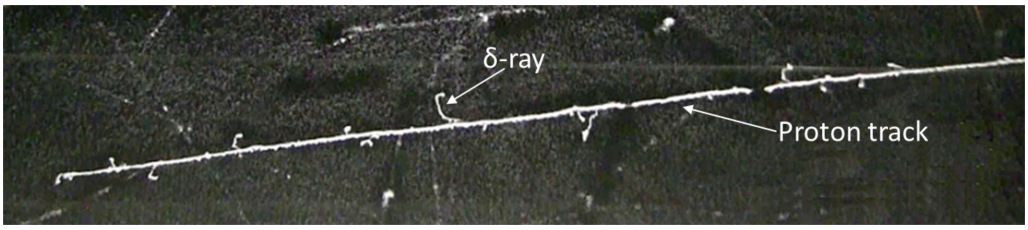

Figure 2.10: Image of a proton track in a a cloud chamber. Tracks of secondary particles known as δ-rays can be seen propagating away from the core proton track. Taken from IAEA [54]

2.3.3 Track Formation and Generation of Secondary Electrons

As the proton propagates through condensed matter, initially a highly structured set of nm-scale tracks of ionisation damage is created along the proton trajectory. As the proton propagates into the material, the ion mainly interacts with valence band and core electrons, imparting energy through the previously discussed interaction mechanisms. If the atom is ionised and an electron is ejected, these energetic electrons (also called δ-rays) can travel several millimetres away from the core of the proton track and induce secondary ionisations [51], further exciting electrons and leaving behind positive holes (an example of a proton track in a cloud chamber is shown in figure 2.10). The proton tracks and generated secondary particles in turn generate steep energy density gradients over nanometre distances. In dielectric materials, when an electron is excited into the conduction band it can then be classed as free and is able to diffuse throughout the material. As the dynamic recovery phase of a solid begins immediately after irradiation, the highly localised gradients start to seed a rapid diffusion of the excited electron population into the surrounding, unperturbed material [55].

2.4 Methodologies

This section will discuss the core experimental method used in this experiment for observation of ultrafast dynamics within materials. Any alterations to the main method are discussed in the relevant results chapters.

2.4.1 The TARANIS Laser Facility

Since installation in 2006, the TARANIS (Terawatt Apparatus for Relativistic and Nonlinear Interdisciplinary Science) laser facility at QUB has been involved in a number of ion acceleration experiments. The TARANIS laser is a hybrid Ti:Sapphire-Nd:glass system that operates using the principle of CPA outlined earlier. Capable of producing laser intensities up to $10^{19}\,\mathrm{W/cm^2}$ at a wavelength of 1053 nm and pulse durations between a nanosecond and 700 femtoseconds [56]. The creation of these pulses involve a number of different stages, a schematic showing the layout of TARANIS is contained in figure 2.11.

The TARANIS system begins with a commercial Ti:Sapphire Mira oscillator that generates a train of 120 fs pulses at 1053 nm. The pulse is stretched by a factor of 10^4 by a pair of diffraction gratings in a double-pass stretcher, resulting in a nanosecond long chirped pulse. The regenerative amplifier initially delivers 0.6 mJ pulses using a Ti:Sapphire crystal optically pumped by a commercial Coherent Evolution Nd:YLF laser. The next stage involves the use of amplification rods of increasing diameter (9 mm, 25 mm and 50 mm) to amplify the pulse into the terawatt region. Before the third set of rods, the beam is split in two before passing through two separate pairs of 50 mm amplifiers, allowing two separate pulses to be produced, each with energies of around 20 J. After compression, the pulses can deliver $\sim$10 J to the target with a typical duration

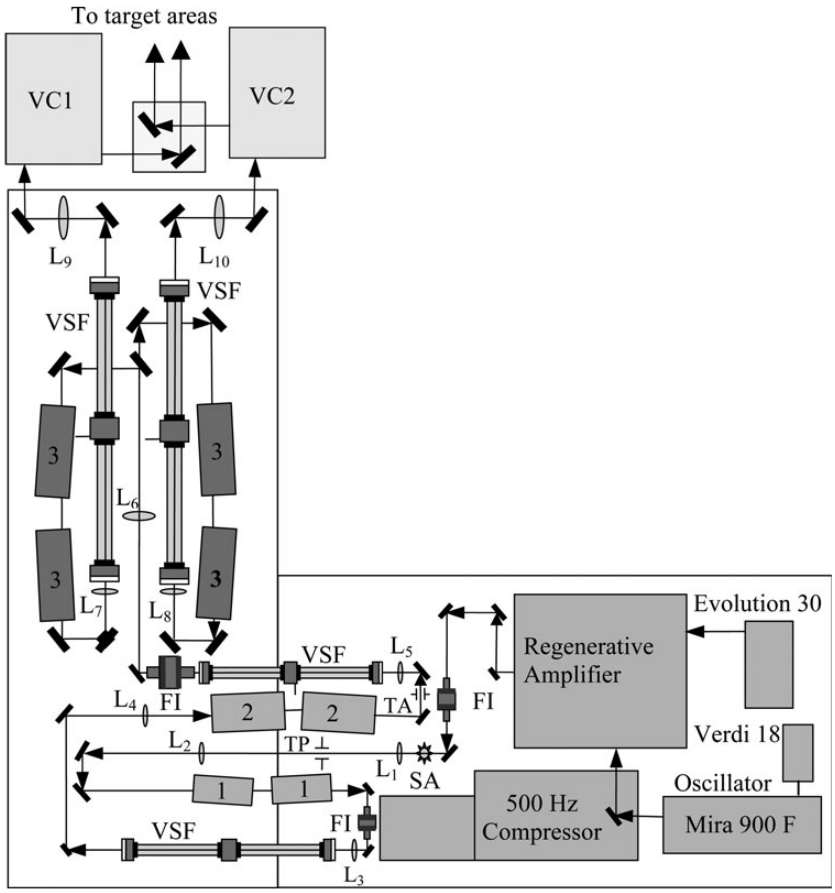

Figure 2.11: Layout of TARANIS laser. FI Faraday isolator; VSF vacuum spatial filter; TA Teflon aperture; TP Teflon pinhole; SA serrated aperture; 1, 2, 3 - laser heads with Nd:Glass rods of 9 mm, 25 mm, and 50 mm diameter, respectively; L1L2, L3L4, L5L6, L7L9, L8L10 relay imaging telescopes, VC1, VC2 vacuum compressors. Taken from Dzelzainis *et. al.* [56].

of 700 fs [56].

The flexibility of TARANIS allows for a combination of pulses to be delivered into the target area. A short and long pulse can be used, or two short pulses. In addition to this it is possible to extract a pulse after the 25 mm amplification rods to compress into a separate probe pulse for use in optical probing techniques.

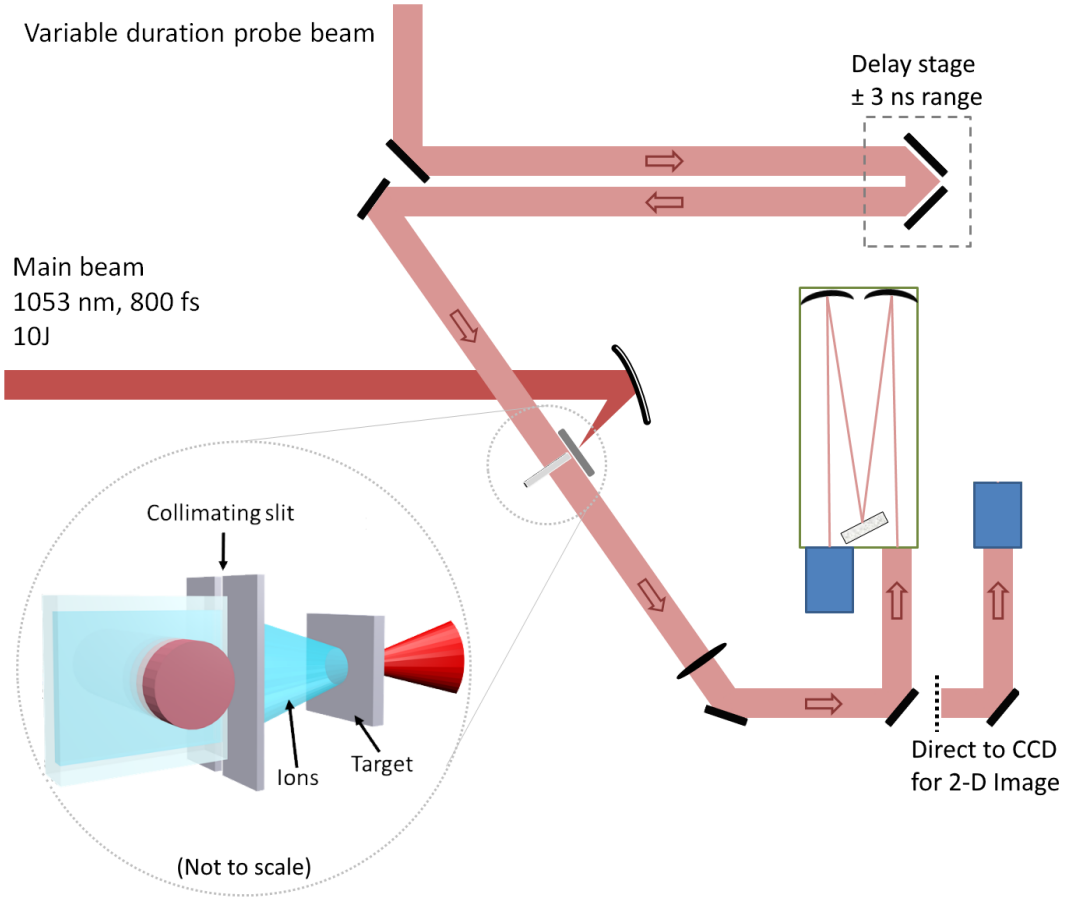

Figure 2.12: Sketch of the typical experimental setup (not to scale). Protons are generated via the TNSA mechanism, which propagate 5.0 ± 0.5 mm through vacuum and are collimated to a width of 500 µm. The probe back-illuminates the sample and the interaction region is imaged onto the entrance of a 1 m imaging spectrometer at 12× magnification. Alternatively the interaction region can be sent directly to a CCD for a 2-D image of the opacity generated in the sample.

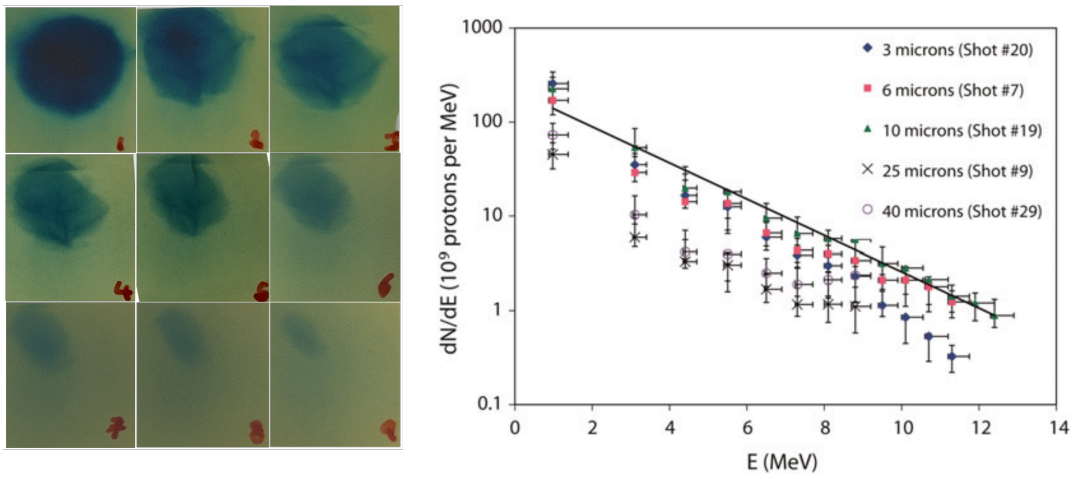

Figure 2.13: **Left**: Typical RCF data obtained using HD-V2 Radiochromic film. Layers are numbered 1–9. Each film in the stack acts as a filter for the following layers, with Layer 1 corresponding to proton energies >2 MeV and layer 9 to >9.5 MeV. **Right**: Plot showing typical proton spectra obtained using the TARANIS laser system for different target thicknesses [56].

2.4.2 Experimental Technique

The TARANIS laser was used to deliver high energy pulses to a 12 µm thick aluminium target to generate protons via the TNSA mechanism. The protons were accelerated to an endpoint energy of 10.0 ± 0.5 MeV measured using stacks of radiochromic film, an example shown in figure 2.13. The generated proton burst then propagated 5 mm in vacuum, collimated to a width of 500 µm using a 1 mm thick aluminium slit before reaching the sample. Low energy protons and electrons were also removed by placing a 50 µm thick piece of aluminium foil in front of the sample. A schematic showing the typical experimental setup is shown in figure 2.12. The sample was then back-illuminated using the probe beam and the illuminated region imaged either directly onto a CCD for 2D imaging of the interaction or into a 1 m imaging spectrometer.

2.4.3 Target Alignment

To enable high ion energies to be produced it was important that the plane of the target foil was as close to the focus plane of the main laser beam as possible. This was achieved using an alignment system outlined in figure 2.14.

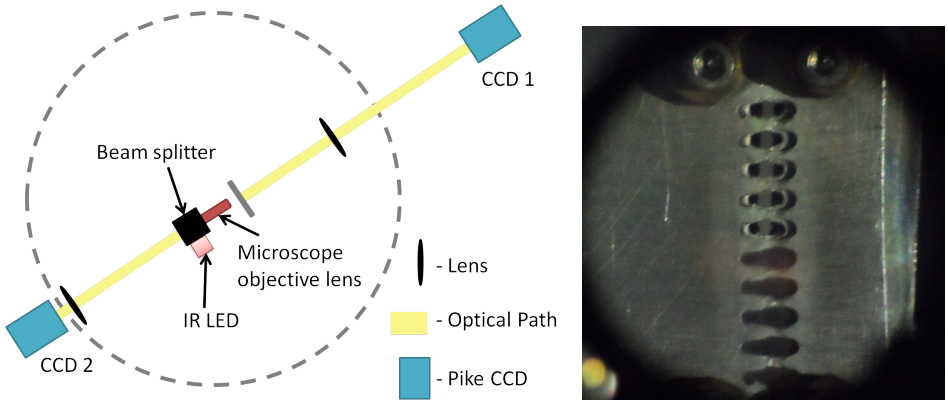

Figure 2.14: Diagram and view through lens for target alignment.

The first step to target alignment was to macroscopically move the target foil into an approximate plane of focus. This was done by viewing the target plate through a lens using CCD 1 (as shown in figure 2.14). As the target was on a motorised X-Y-Z stage, it's position could be altered easily using a motor controller.

The alignment system consisting of the IR-LED, beam splitter and objective lens were placed on a motorised stage alongside the sample mount, this allowed the sample to be driven in and out of the laser/ion beam, while the camera outside the chamber remained fixed. The camera permitted real time readouts and was initially used to find the focal spot of the laser by using the motorised stage to adjust the focusing plane of the objective. When the focal plane of the laser was found, the target plate was inserted and back-illuminated using an IR-diode through a beam splitter, where the target could then be moved, using a separate motorised stage, into the focal plane of the laser. A second camera

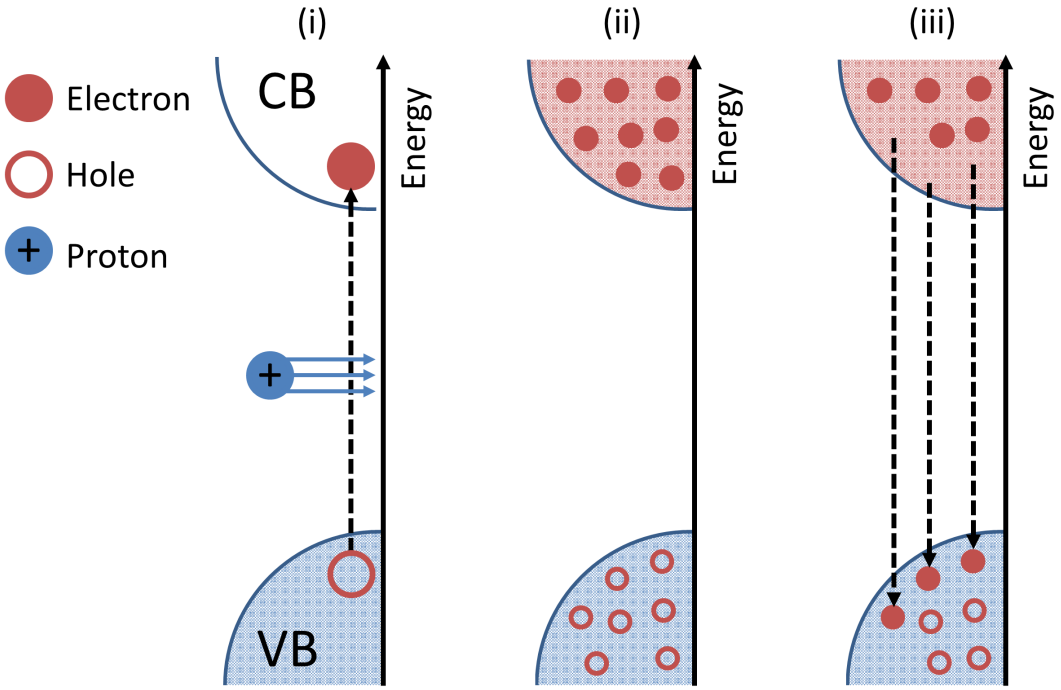

Figure 2.15: Schematic outlining carrier generation in a solid via proton irradiation. (i) The proton imparts energy to electrons in the material, if enough energy is transferred they will be excited across the optical gap into the conduction band. (ii) These excited electrons can remain in the conduction band for a period of time, while in the conduction band they are classed as free electrons and can undergo free-free absorption of optical radiation. (iii) after a time Δt, the excited electrons decay through various channels to the valence band.

was placed outside the chamber to observe the macroscopic movement of the target plate.

2.4.4 2-D Imaging and Optical Streaking

Imaging directly onto the CCD provides a 2D snapshot of the generated opacity as seen in figure 2.16 taken with the transform limited 470 fs pulse duration. It is possible to observe the evolution of opacity by taking several of these snapshots, delaying the probe for each image, essentially adding (or subtracting) path length to the probe beam before interaction with the sample in the chamber.

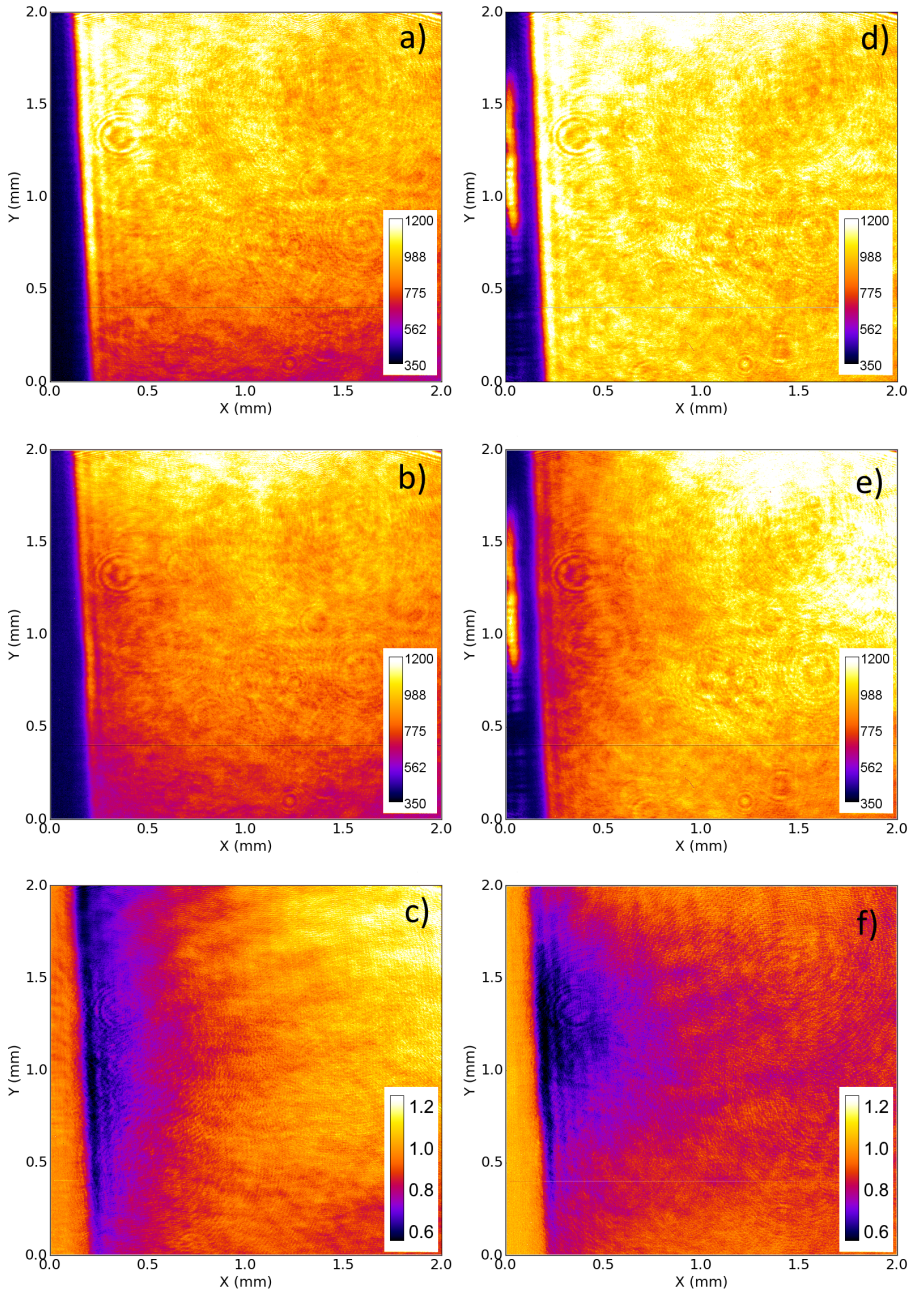

Figure 2.16: Examples of 2D images obtained during the investigation of soda-lime glass. Final images (c) and (f) show relative transmission of the probe during the ion interaction compared to the sample probed beforehand. (a), (b), (d) and (e) correspond to an individual laser shot and the proton burst is incident from the left hand side. (c) is the result of $b \div a$ and shows the onset of the opacity just as the protons begin to enter the glass. (f) is the result of $e \div d$ and shows the region 200 ps later when the protons have propagated further into the glass generating an opacity further into the sample. The relative delays are controlled using a delay stage.

For each shot the path length could be changed and the depth of the opacity in the sample could be observed to get an initial understanding of evolution time scales. This method provides a good initial indication for the level of opacity generated in the various samples that were studied and is useful for determining the instantaneous spatial profile of the proton pulse. However as profile of the probe is due to fluctuations, when looking at a large area such as in the 2D images, small variations can appear as false opacity when looking at relative transmission. Also due to the nature of laser driven proton acceleration, comparisons of the generated transient opacity on a shot-by-shot basis are very difficult. Variations in endpoint proton energy and flux can vary as much as 10%. To enable an accurate and reliable measurement of the opacity it is therefore necessary to perform the analysis on a single shot basis. As discussed earlier, the probe line on TARANIS contains a small compressor to achieve a transform limited (TL) probe pulse duration of 470 fs. Bypassing this compressor entirely allows a maximum chirped pulse duration of 1.4 ns, whereas durations between 200 ps and the TL pulse duration can be obtained by changing the distance between the diffraction gratings in the small compressor (as shown in figure 2.19). The optical streaking technique relies on the use of a chirped probe pulse [57], in essence, to encode the evolution of the opacity in the frequency spectrum of the pulse, a sketch of this mechanism is shown in figure 2.17.

Creating an Optical Streak

To highlight the evolution of opacity across an optical streak, images are taken of the interaction region using the probe pulse without also firing the main laser pulse to produce radiation, these shots are called probe only or PO images. On main shots when both laser pulses are fired, an optical streak of the region

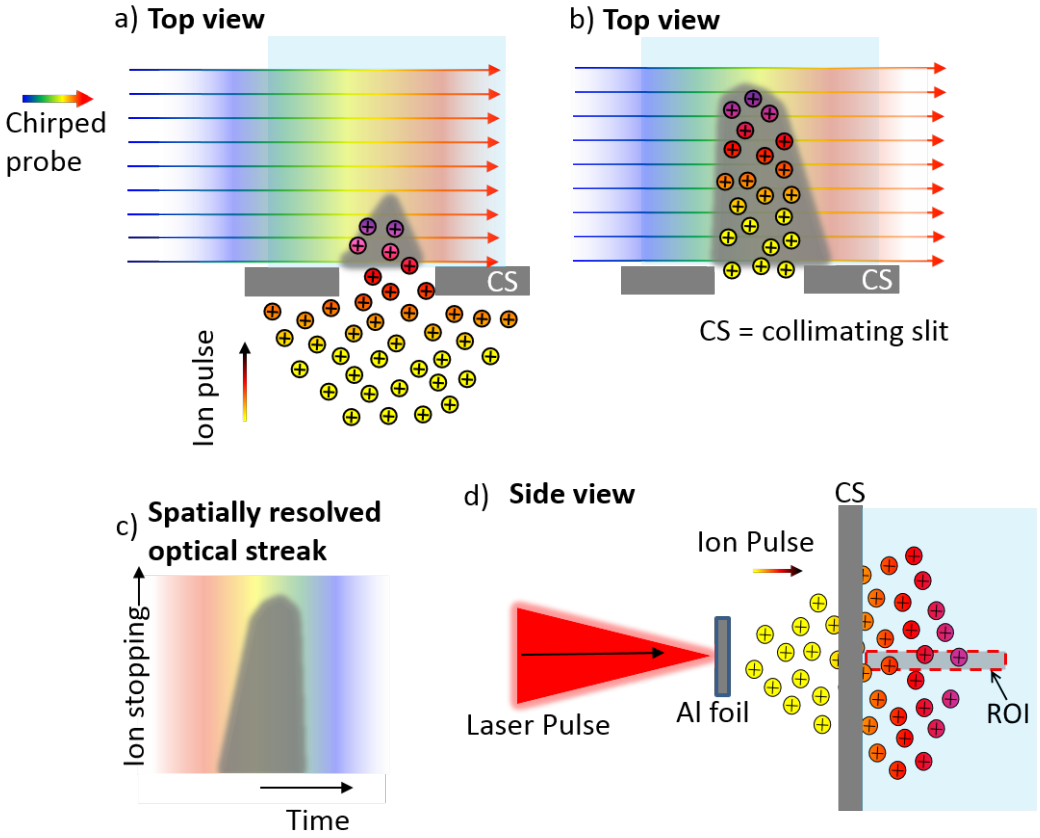

Figure 2.17: Schematic overview of the optical streaking method. In (a) and (b) the protons enter the sample after passing through the collimating slit (CS) and begin to deposit energy in the sample. The spatially resolved optical streak shown in (c) is obtained using a 1 m imaging spectrometer. The region of interest (ROI) shown in (d) is a 10 µm slice along the central axis of the proton burst that is imaged onto the entrance slit of the imaging spectrometer.

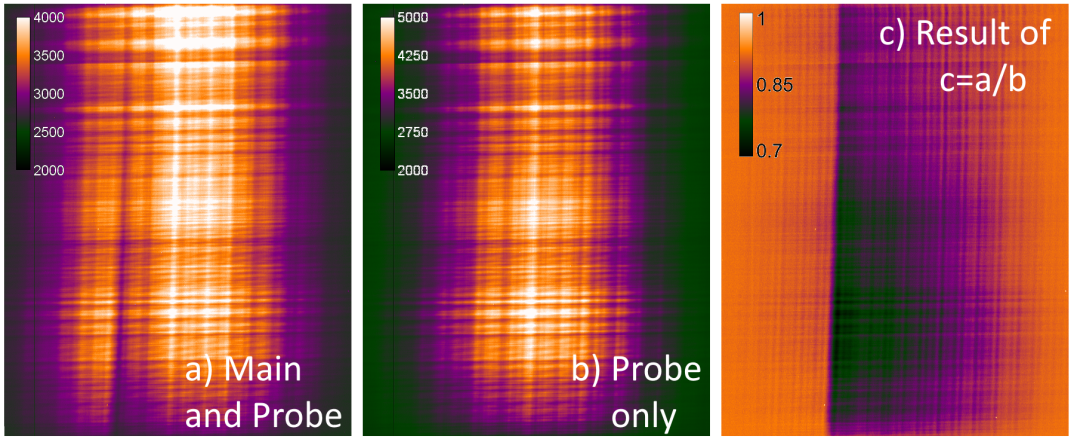

Figure 2.18: Final optical streaks presented in this thesis originate from the comparison between a probe-only image showing normal transmission of the probe through the sample and an image taken when the main pulse is fired to generate protons.

is obtained with opacity information encoded in it. Figure 2.18 shows how the final streak is produced. Each final image shows the evolution of opacity generated in the sample compared to a reference probe-only streak.

Increasing the distance between the gratings in the compressor from the TL pulse duration will increase group-delay dispersion (GDD) and can be used to provide larger pulse durations. The GDD β induced by a pair of gratings as in figure 2.19 is given by [3]

$$\beta = \frac{L_g \lambda^3}{\pi c^2 d^2} \left[1 - \left(\frac{\lambda}{d} - \sin\gamma \right)^2 \right]^{-\frac{3}{2}} \tag{2.8}$$

where L_g is the grating separation, λ is the central wavelength, d is the grating constant and γ is angle of incidence of the beam onto the grating. Knowing the value of GDD from the grating separation and the TL duration τ_0 allows the pulse duration τ to be calculated [58]

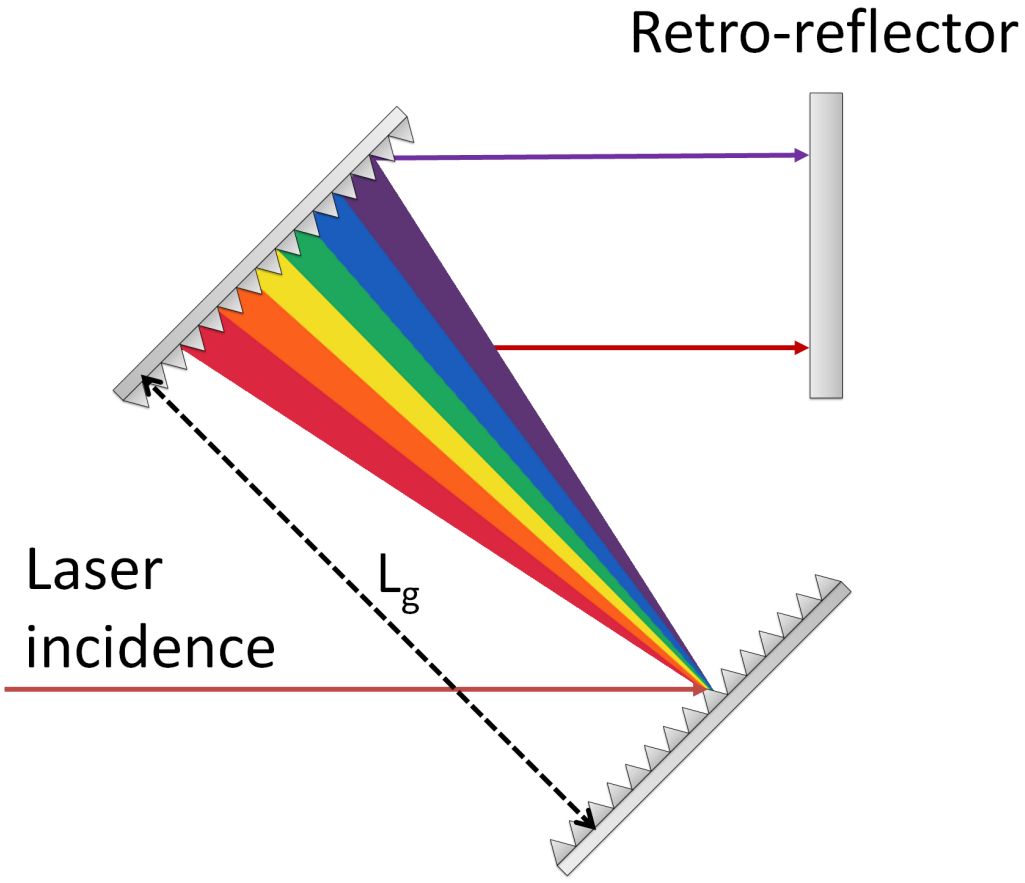

Figure 2.19: Schematic showing the layout of diffraction gratings in the probe compressor of TARANIS, showing the beam direction and the grating separation L_g.

$$\tau = \tau_0 \sqrt{1 + \left(\frac{\beta}{\tau_0} 4 \ln 2\right)^2} \tag{2.9}$$

The Wigner distribution [59] shown in figure 2.20 represents the temporal and spectral domains of the pulse simultaneously and was used to calculate the frequency distribution of the 470 fs TL pulse duration from TARANIS [60]. When the pulse is stretched to 200 ps by increasing the grating separation, the frequency components are now spread over a larger temporal window due to group delay dispersion (as shown in 2.20b) however this does not result in an increase of the temporal resolution of the TL pulse at a given frequency as the intensity distribution conversely narrows with increasing pulse width as shown in 2.20c and has also previously been verified by Polli et al. [57]. Although the plots of which are not included here, this is also the case for each of the probe pulse durations used in the following experimental chapters and preserves the TL pulse duration serving as one of the fundamental resolution limits for the experiment, the other being the resolution of the imaging spectrometer which is determined by the grating type, slit width and detector pixel size. A list of resolutions for various probe durations is included in table 2.1. It is important to note that for all of the pulse durations listed except for the 1 ns probe, the factor limiting the resolution of the measurement is the TL pulse duration as it is the larger of the two at 0.47 ps.

2.4.5 Transient Absorption Spectroscopy

The study of ionisation dynamics in matter generally relies on the radiation producing some measurable change within the material. For pulsed-ion radiolysis in water, chemical scavengers are added to the water to measure the final reaction products from the ionising radiation. In optical streaking, the absorption

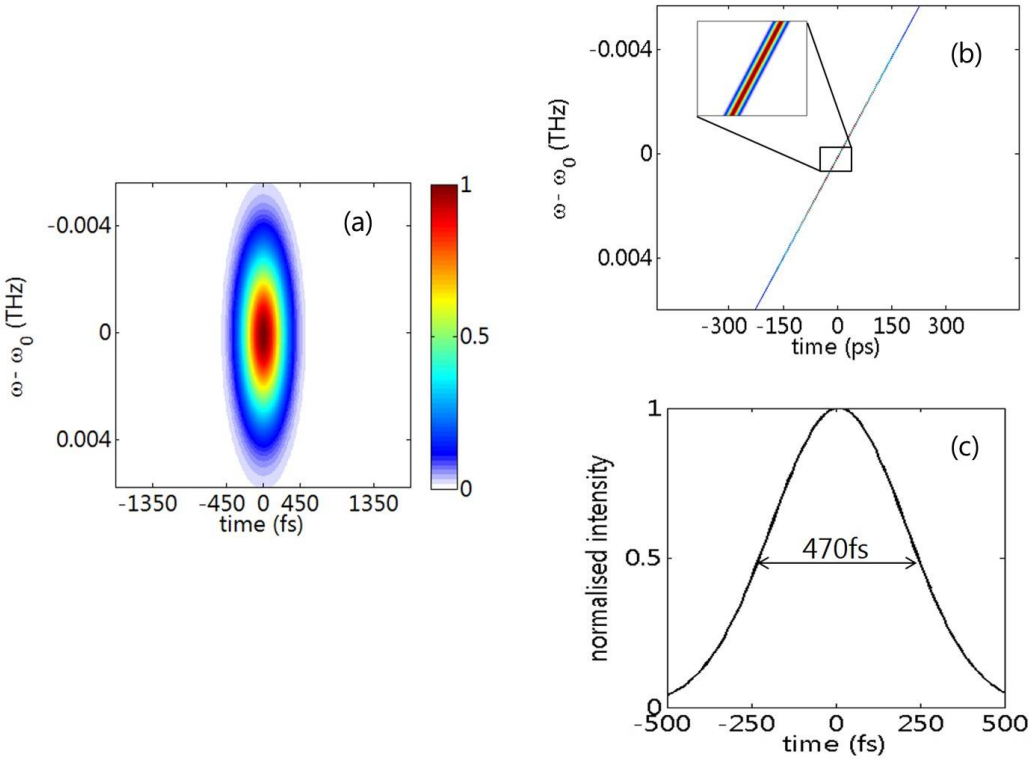

Figure 2.20: (a) Wigner distribution of the 470 fs transform limited pulse duration from the TARANIS probe line. (b) shows the distribution for the chirped 200 ps probe duration, the inset of (b) shows the intensity distribution in a zoomed region around the central frequency ω_0. (c) is a lineout of the chirped probe pulse taken at ω_0 showing that the 470 fs FWHM pulse duration is maintained, this is true for any frequency component of the distribution. Taken from [60].

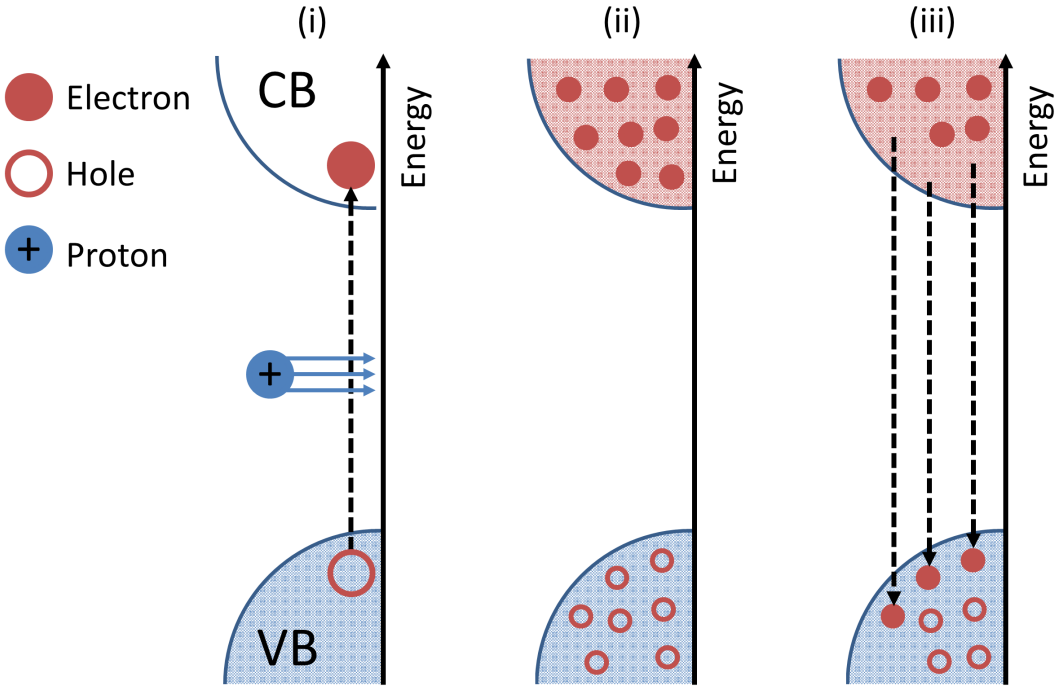

Figure 2.21: Schematic outlining carrier generation in a solid via proton irradiation. (i) The proton imparts energy to electrons in the material, if enough energy is transferred they will be excited across the optical gap into the conduction band. (ii) These excited electrons can remain in the conduction band for a period of time, while in the conduction band they are classed as free electrons and can undergo free-free absorption of optical radiation. (iii) after a time Δt, the excited electrons decay through various channels to the valence band.

Probe Duration (ps)	Minimum Resolution (ps/pixel)
50	0.09
100	0.18
200†	0.37
1000†	2.44

Table 2.1: Table showing resolution limits of the spectrometer imaging system for various probe pulse durations. †denotes pulse durations discussed in the results of this thesis.

of a synchronised probe beam is used to examine these ionisation dynamics. As protons traverse the material they generate tracks of a highly structured and inhomogeneous dose distribution, generating steep energy density gradients. In dielectric materials, this leads to electrons being excited into the conduction band, where they essentially become free and are then able to diffuse throughout the material. Once the electron is excited into the conduction band, its lifetime in this state can be measured through the free-free absorption of optical probing radiation, a schematic of this process is shown in figure 2.21.

2.4.6 Proton Energy Bandwidth Selection

As has already been outlined, to observe ultrafast dynamics within a material it is critical to have a pump pulse shorter than the lifetime of the species under investigation. As pulses shorter than 100 ps are not routinely available from radiofrequency accelerators, this investigation takes advantage of the ultrafast acceleration phase of protons via the TNSA interaction.

As already outlined in section 2.3.2, protons will continue to travel further into a material until they lose all of their energy, this gives them a defined range for a specific proton energy; For example in borosilicate glass (BK7), a 10 MeV proton will travel (on average) approximately 600 µm into the glass before losing

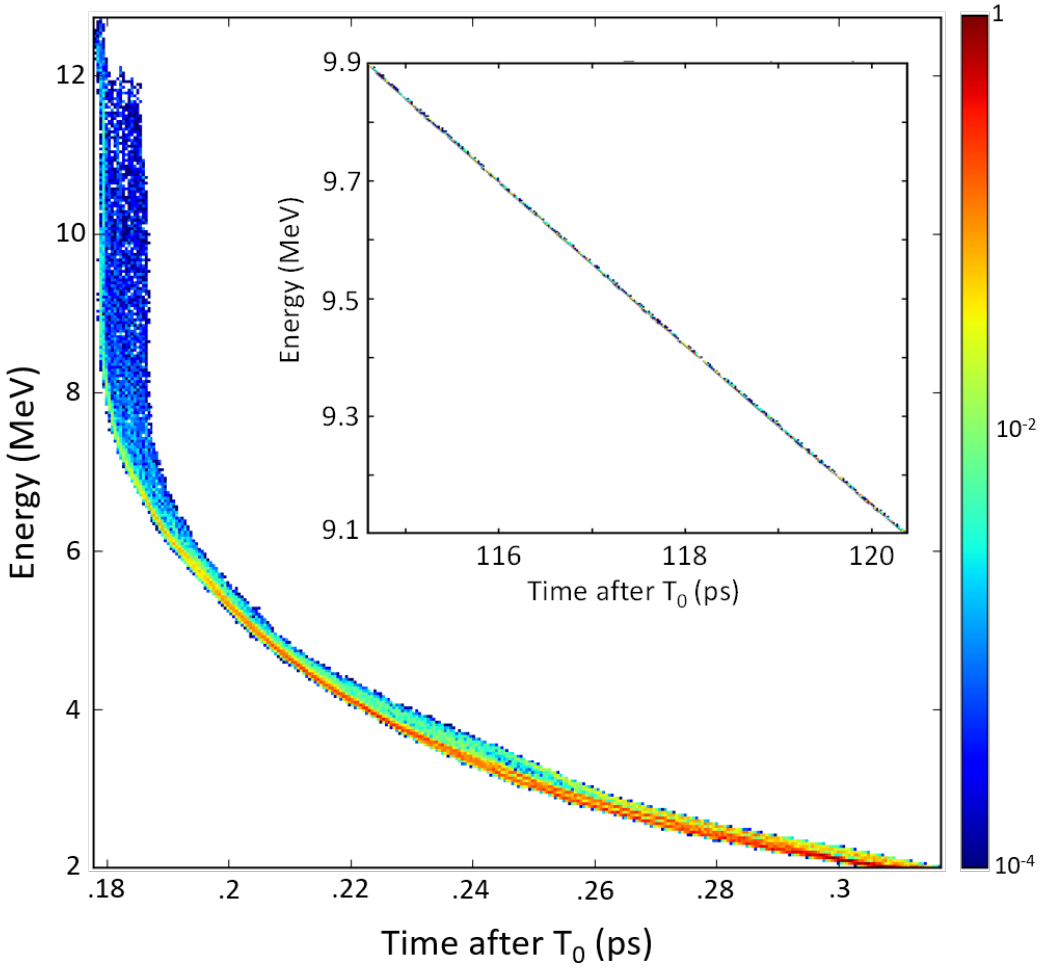

Figure 2.22: Velocity dispersion of protons generated via TNSA for an initial pulse duration of 10 fs. After propagating 8 µm in vacuum the total pulse width has stretched by a factor of ten. Inset figure shows pulse width of $9-10$MeV protons has stretched to >5 ps after travelling 5 mm. Courtesy of Stephan Kuschel.

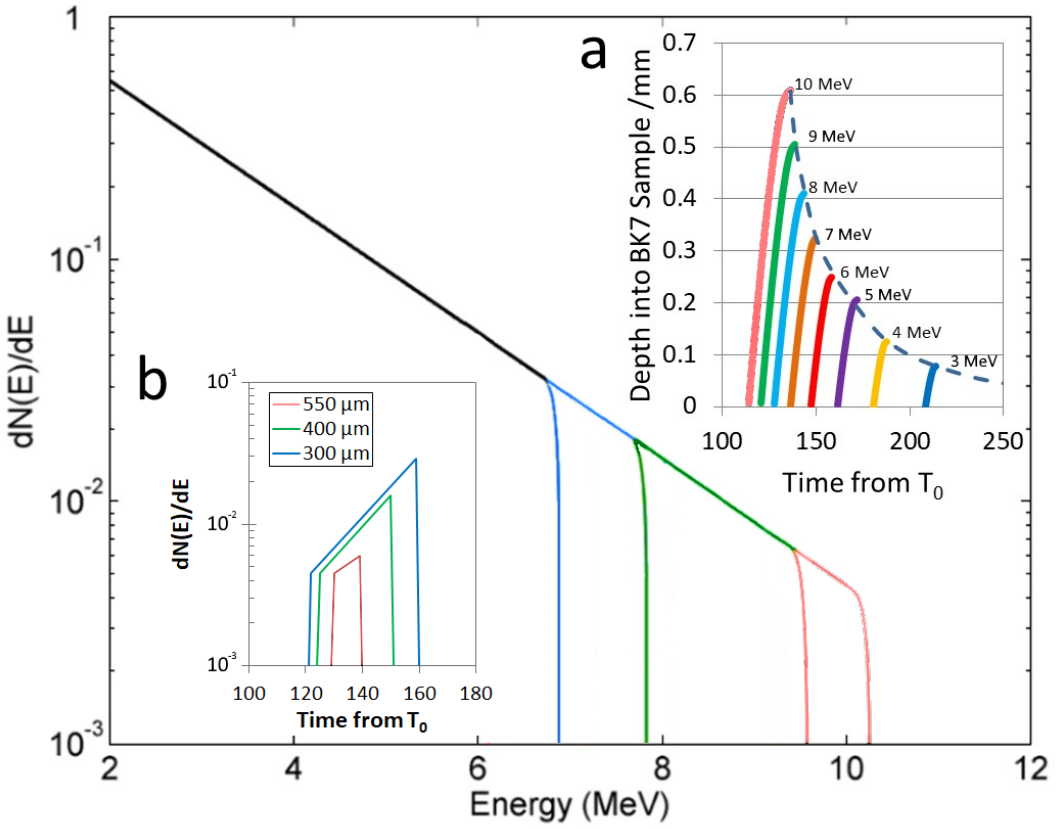

Figure 2.23: Schematic of a typical TNSA spectrum with a high-energy cutoff at 10 MeV the coloured lines represent cutoff regions corresponding to energy ranges shown in inset (b). Inset (a) shows the overall propagation and arrival times of protons in BK7 glass for energies up to 10 MeV obtained from SRIM calculations [53]. The large temporal spread is due to different propagation times across vacuum stretching the pulse in time. Inset (b) shows the arrival time for energy bandwidths remaining in the borosilicate glass at three different depths including the propagation time across 5 mm of vacuum. Here T_0 refers to the time that the protons were generated. This illustrates the successive narrowing of the pulse from lower energy proton stopping as it propagates into the sample.

all of its energy. Due to the nature of proton generation via TNSA however, the generated proton spectrum is not monoenergetic but will instead contain a wide range of energies with a sharp cut-off as shown in figure 2.23. This wide energy spectrum experiences significant velocity dispersion as shown in figure 2.22, where vacuum propagation over 6 µm stretches the pulse by a factor of ten from its initial 10 fs duration. Even when looking at a narrower energy spread, after 5 mm of travel a 9-10 MeV energy slice will have a temporal width of just over 5 ps as shown in the inset of figure 2.22. There is a relatively easy way to overcome this however, which is to use the nature of proton stopping in matter as a form of energy filtering to recover the initial short pulse durations.

Figure 2.23 contains a schematic of a typical TNSA energy spectrum with a high energy cut-off at 10 MeV Figure 2.23a shows the pulse profile from the arrival times and propagation depths of protons in 1 MeV energy steps. The first of the 10 MeV protons arrive approximately 115 ps after the laser pulse due to the 5 mm of vacuum propagation followed by lower energy protons that arrive over the next 150–200 ps. Therefore close to the front surface of the glass the total interaction time with the proton pulse is relatively long however this narrows significantly at greater depths as the highest energies will propagate the greatest distances. The inset of 2.23b shows how the initial short pulse duration could be retrieved inside the sample through successive stopping of lower energy protons.

Chapter 3

Ultrafast Ionisation Dynamics in SiO_2: The Self-trapping Process

---

The study of how protons and other forms of heavy particle radiation interact with bulk materials is a vast research area. From cancer therapy to various industrial applications, many studies focus on the generation of these particles or the macroscopic damage caused by the radiation. It is equally important, however to understand these mechanisms on the nanoscale, as it is here where fundamental processes occur that lay the groundwork for the material response to the radiation. These processes that occur on femtosecond and picosecond timescales have yet to be fully examined with proton radiation due to the aforementioned RF accelerator methods providing long pulse durations, masking these ultrafast dynamics within the material.

This chapter will examine how the ultrafast decay pathways available to electrons when excited in the conduction band (by laser-driven proton bursts) permit direct observation and measurement of short, few-ps proton pulses. In order to observe ionisation dynamics on the order of 10s of picoseconds it is neces-

sary to start off with an even shorter pumping time, in this respect the use of laser-driven protons with their short bunch durations have a large advantage compared to traditional RF acceleration schemes. The short bunches enable observation of ultrafast dynamics within the material that would otherwise be masked by the much longer pump pulses used previously. The ultrafast response of SiO_2 will be examined, showing that the rapid decay channels available in the material permit direct measurement of the TNSA proton pulse duration and in doing so set a benchmark for the proton pulse characteristics discussed in subsequent chapters.

3.1 The Role of Electron Diffusion in the Recovery of SiO_2

Earlier in chapter 2, the interaction and deposition of energy by protons was discussed. When compared to electron or photon irradiation schemes, although these methods can produce short pulses the major difference with protons is the steep energy density gradients induced in track region and the resulting holes generated by electron excitation that drive electron diffusion up to tens of nanometres in the unperturbed material surrounding the track [55]. This initial nanostructured dose distribution evolves over hundreds of picoseconds, driven by electron diffusion within the material.

Previous studies into the generation of electron-hole plasmas and induced defects have been performed in SiO_2 using multiphoton ionisation with intense femtosecond lasers [61–63]. The studies revealed an ultrafast decay channel available to the excited conduction band electrons through the formation of self-trapped excitons (STEs). This formation process occurred within 150 fs after irradiation. Before this the electrons would be able to take part in free-free

absorption of optical radiation, placing a limit on the lifetime of an observable opacity.

The STE generation process is only dominant for electron densities $<10^{19}\,cm^{-3}$, however the peak density around proton tracks is on the order of $10^{22}\,cm^{-3}$, this is comparable to electron-hole plasma conditions and should prevent the formation of self-trapped excitons [63]. To investigate this in more detail a simple model was produced (shown in figure 3.2) which tracks the evolution of electron density in a $1\,\mu m^2$ area of SiO_2 following irradiation by protons. It is important to mention that this simple model tracks diffusion only and does not include any inhibiting factors such as random structural defects or the presence of electron trapping sites but instead is intended to only illustrate how the electron density transitions from an electron-hole plasma ($N_e \gtrsim 10^{22}\ cm^{-2}$) to free electron gas conditions ($N_e \lesssim 10^{19} cm^{-2}$) [64–66]. The model clearly shows that for a flux of 50 tracks per μm^2 (expected at the highest proton energies), an initially inhomogeneous electron density distribution is created at the time of initial track formation, as the density gradients drive electrons into the surrounding bulk medium, the electron density falls rapidly and begins to homogenise to free-electron gas conditions within a few hundred femtoseconds (this is shown in figure 3.2a and b). If the electron density remains high, this can affect the lifetime of the formed self-trapped excitons. Increasing the number of tracks (i.e as shown in figure 3.2c and d) results in a much more homogeneous dose distribution being created, after a few hundred femtoseconds the high density in the local area maintains electron-hole plasma conditions. At this high density a near-continuous ionisation of the forming excitons is taking place, maintaining a population of electrons in the conduction band and extending the duration of the opacity in SiO_2 [67].

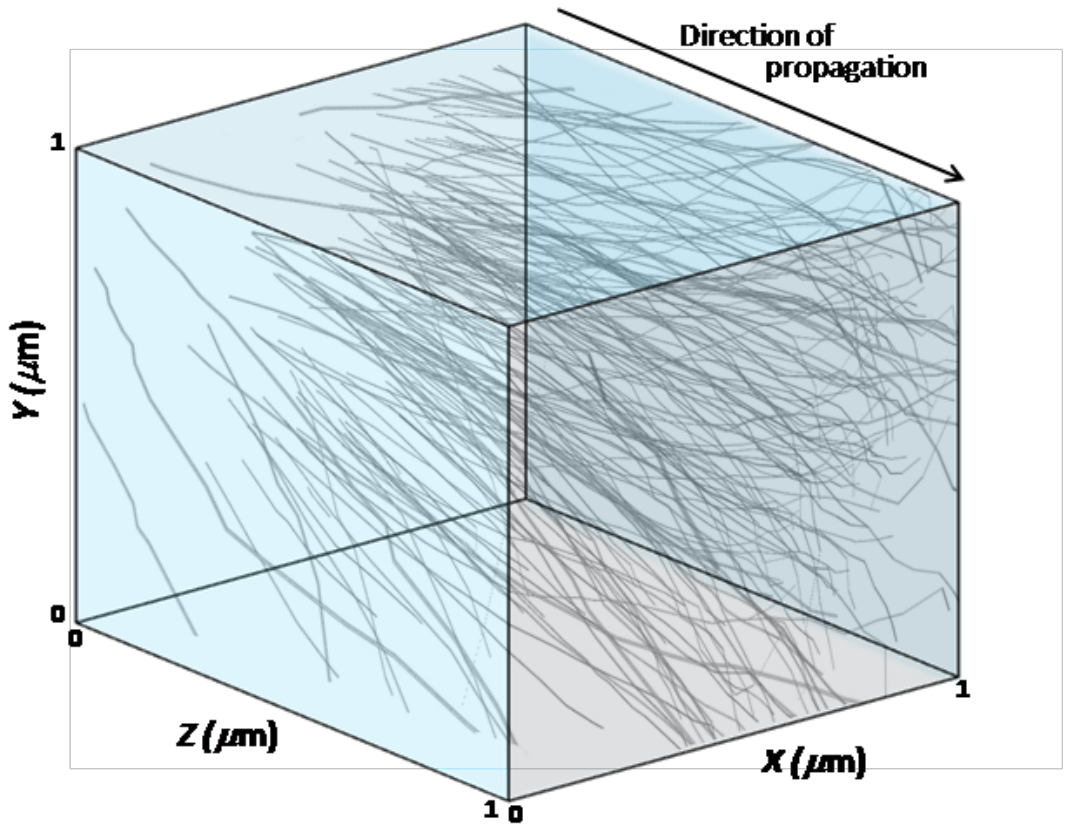

Figure 3.1: 3-D plot of nanoscale ionisation tracks generated in a 1 µm^3 volume of SiO_2. Obtained using a combination of SRIM [53] and FLUKA [68, 69] simulations to calculate track location and ionisation radius.

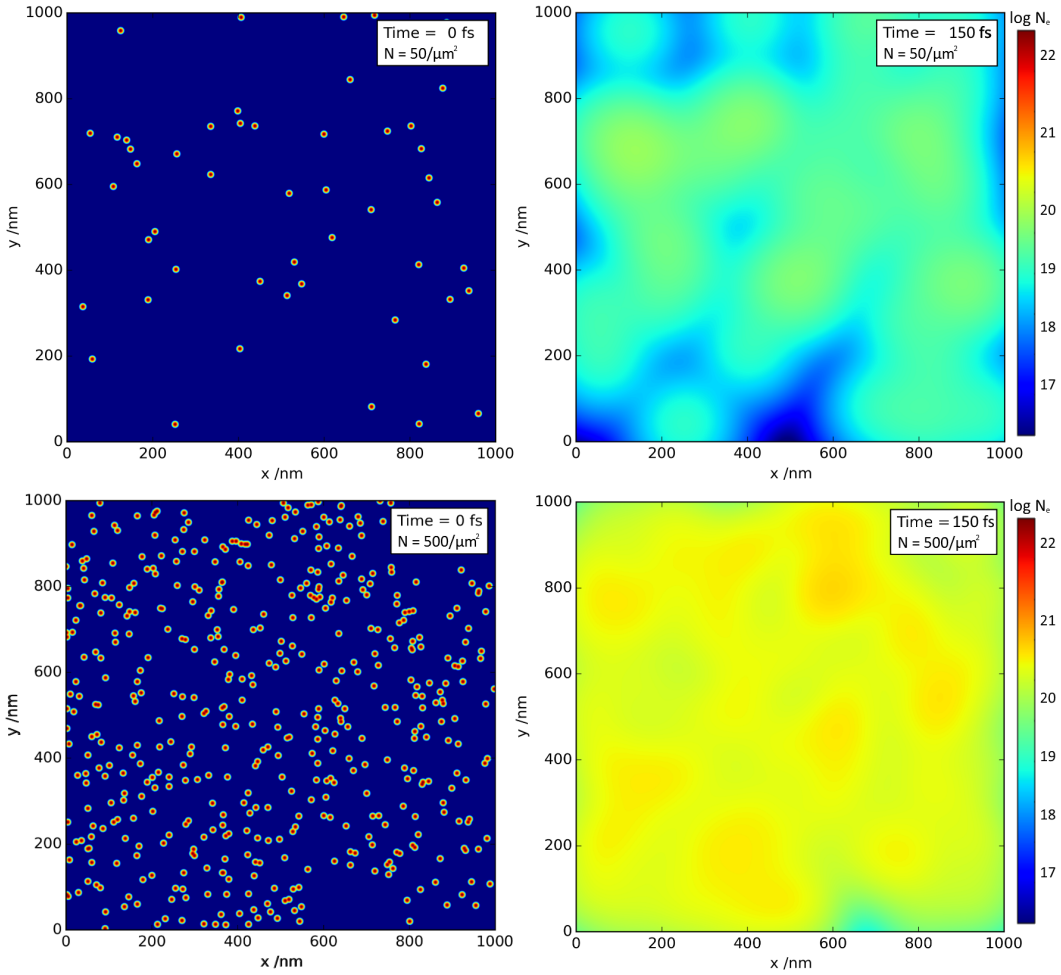

Figure 3.2: Modelling rate of electron diffusion in SiO_2 prompted by proton tracks. (a) and (b): Electron density plots showing diffusion of the electron population with a proton track density of $50\,/\mu m^2$. Plots (c) and (d) show electron diffusion for an initial track density of $500\,/\mu m^2$. Diffusion rates for electrons obtained from Osmani et al [65, 66].

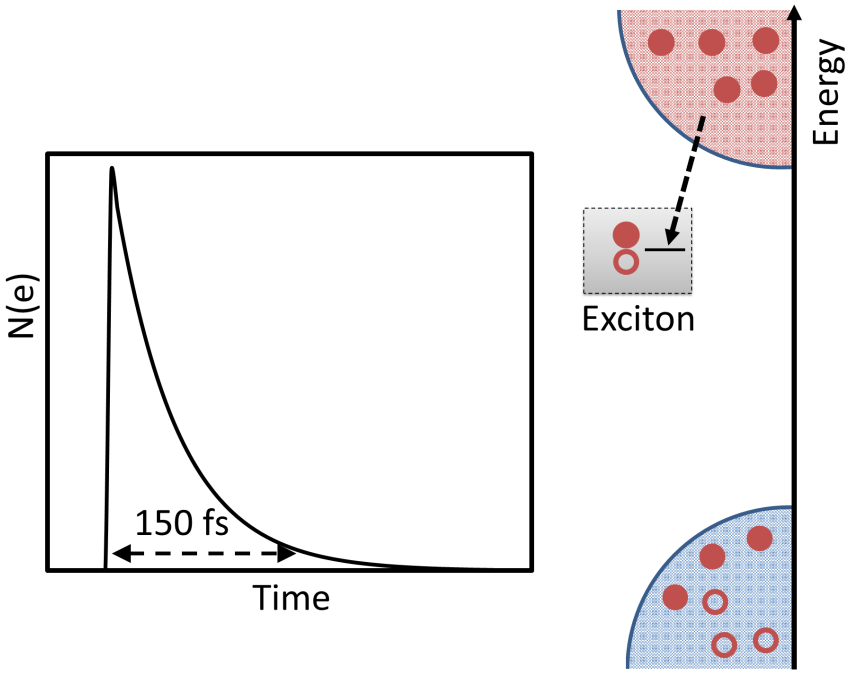

Figure 3.3: Relaxation dynamics of excited electrons in SiO_2. Exciton formation enables an ultrafast electron relaxation pathway for conduction band electrons with a formation time of ≈150 fs [61, 70].

3.2 Ion-induced Ultrafast Dynamics in SiO_2

Amorphous silicon dioxide is ubiquitous and forms a key component in many technologies e.g. cores and claddings for fibre optics used in telecommunication and satellite technology, chromatography [71], microelectronics [72] and is used as the gate layer in 90% of all metal-oxide semiconductor devices [73]. In the laboratory it is used in optical windows and many transmissive or reflective optical components. As a result it is a material which has been studied extensively. Many of these studies have examined defect formation and absorption bands resulting from exposure to ionising radiation as this can affect the optical or electronically insulating properties of the material, leading to device malfunction or failure. Building on past photoexcitation studies, this section will discuss the use of the optical streaking technique introduced earlier

in chapter 2 to perform transient absorption spectroscopy by observing the evolution of an ion-induced opacity in high-purity amorphous SiO_2 (fused silica) and present experimental observations of the ultrafast recovery of SiO_2 when exposed to ionising radiation, demonstrating how this can be used to perform pulse metrology for short bursts of laser-driven protons.

As previously discussed, the experimental technique relies on the excitation of electrons across the optical gap of SiO_2, the free-free absorption of these carriers enables an opacity to be observed when optically probed with $\approx$1 eV radiation (1053 nm). This opacity will exist for a period of time until the material has recovered, and the electrons are no longer present in the conduction band. For SiO_2 in particular, a specific ultrafast decay pathway is available to the excited conduction band electrons through the formation of self trapped excitons (STEs), a schematic of which is shown in figure 3.3. A STE is essentially a bound electron-hole pair, which are attracted to each other via the Coulomb force.The STE has been extensively studied for it's role in the relaxation time of laser-irradiated glass [70] and was first experimentally verified by Tanimura et. al. in 1983 [74]. The formation time of these STEs is on the order of 150 fs after excitation and once formed, removes the electron from the conduction band where it is no longer considered free and therefore not capable of absorbing optical radiation from the probing pulse [61, 62].

Figure 3.4a shows a typical experimentally obtained optical streak of the opacity generated in SiO_2 which is in excellent agreement with Monte-Carlo based modelling shown in figure 3.4b. It is clearly shown in both the experimental and modelled data that the duration of the induced opacity gets shorter with respect to depth due to the stopping of lower energy protons in the material. A lineout of the raw experimental data taken at a depth of 530 µm is shown in figure 3.4c, this depth corresponds to a proton energy of 9.7 ± 0.5 MeV and

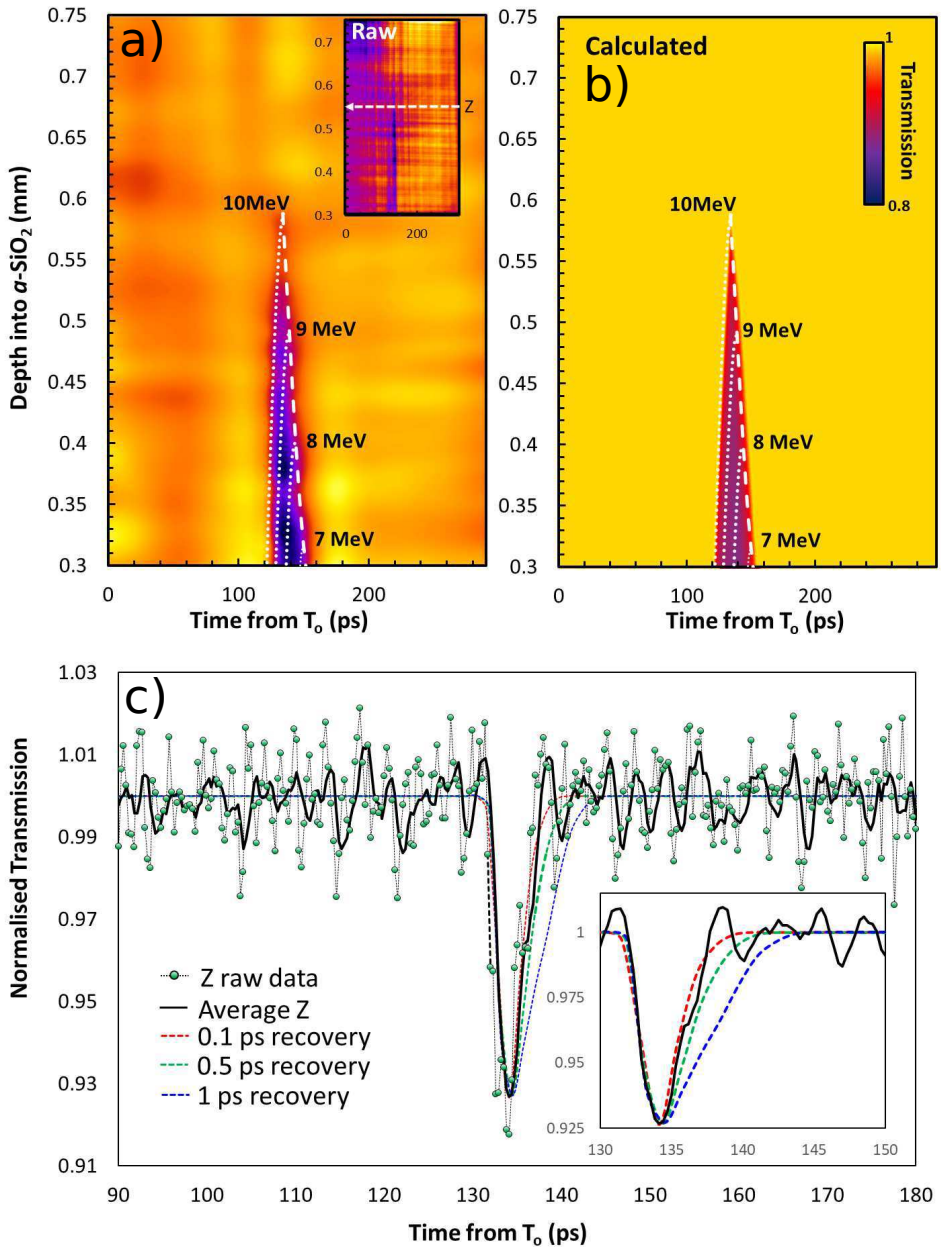

Figure 3.4: Optical streaking data of ion-induced opacity in SiO_2. (a) Optical streak of opacity generated by a TNSA proton pulse. A gaussian blur has been performed on the image for presentation purposes, raw image shown as inset. (b) Model of the expected evolution of the induced opacity in SiO_2 for a material recovery time of 150 fs. The model tracks energy deposited in the material by protons (assuming an initial exponentially decaying energy spectrum with high-energy cutoff at 10 MeV through stopping obtained from SRIM [53]. The opacity generated is assumed to be directly proportional to the amount of energy deposited. A decay constant is then applied (in this case 150 fs) to model the experimental data. (c) Lineout of raw data taken at Z – 530 µm of optical streak shown in (a), the observed FWHM pulse duration of the opacity is 3.5 ± 0.7 ps. The inset of (c) shows a comparison between the observed opacity and modelled data for different response times of the detector.

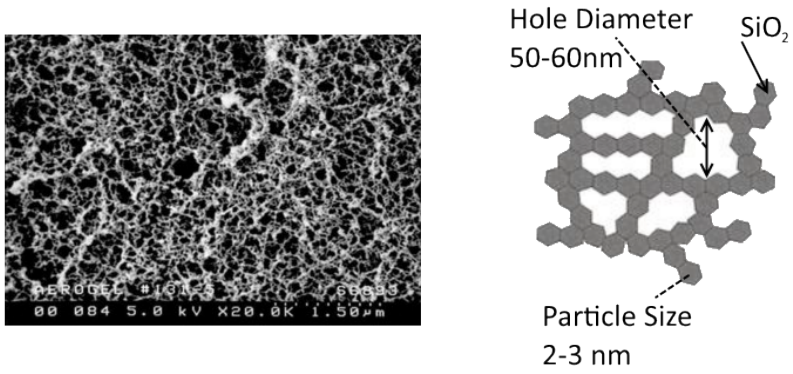

Figure 3.5: Micrograph of aerogel structure (taken from [75]) accompanied by schematic indicating the dimensions of the nanostructure within a typical aerogel.

shows a FWHM pulse duration of 3.5 ± 0.7 ps alongside a best-fit for the detector response of 0.5 ps which matches well with the TL 470 fs probe pulse duration outlined in chapter 2.

3.3 Inhibiting the Diffusion Using Aerogels

A method of inhibiting the rate of electron diffusion experimentally was through the use of aerogel samples. The following section will discuss experimental observations of an ion-induced opacity in silica aerogel and compare these findings to the previously observed ultrafast recovery in SiO_2.

3.3.1 Silica Aerogel

Despite the name, Aerogel (shown in figure 3.5) is a solid synthetic material with a very low solid density (typically $< 0.1\,\mathrm{g/cm^2}$) that does not resemble a gel. Silica aerogels in particular have grown in popularity due to their high porosity, optical transmission ($\approx 99\%$ in visible), surface area ($1000\,\mathrm{m^2/g}$) and extremely

low thermal conductivity ($< 0.01\,\mathrm{W/m\,K}$) [76]. An aerogel is created through sol-gel polymerisation; molecules react with each other to form a network of larger molecules suspended in a liquid solution. The mixture is then critically heated so that the liquid is evaporated without damaging the aerogel structure, leaving behind the macromolecular network of silica. This takes the form of a matrix of SiO_2 strands with a very low density–around 3% of the total material volume [77].

Measuring Opacity in Aerogel

The strands of SiO_2 create a nano-structured network which allows for the examination of the role of electron diffusion on the recovery time of the opacity. The network restricts the available pathways for electron diffusion, so the rapid evolution of the electron density as in amorphous SiO_2 is inhibited, maintaining a higher electron temperature in the surrounding solid material. This process is reflected in the optically streaked data showing much larger recovery times of the generated opacity in the aerogel samples that were examined.

Experimentally obtained optical streaks of opacity in aerogel are shown in figures 3.6 and 3.7 including a side-by-side comparison with the recovery of amorphous SiO_2 and one of the aerogel samples. It is quite clear from the figures that the lifetime of the opacity has been extended orders of magnitude beyond the recovery of amorphous SiO_2 and the proton pulse duration of 3.5 ps. One of the advantages of the optical streaking technique is the flexibility it allows for probe durations, the fused silica investigation was performed mainly using a 200 ps probe however it became quite clear that the evolution of the opacity in the aerogel would not be fully resolved within this pulse, the investigation was then performed using a 1.4 ns probe which provided a large enough temporal

window to fully observe the recovery. Additionally the presence of a second rising edge of the opacity was found in many of the optical streaks in aerogel (an example is clearly visible in figure 3.6a), this observation was attributed to opacity produced by the prompt electrons that are generated during the TNSA interaction and appears as a step-like feature approximately 120 ps before the arrival of fastest energy protons, consistent with the delay due to the propagation across the 5 mm of vacuum between target and sample for the relativistic electrons and the ≈10 MeV energy protons. The generation of opacity from the prompt electrons is believed to be enabled by the aerogel structure as the ionisations from the electrons are able to generate and maintain an excited population long enough to be detected as an opacity whereas this has not been the case in the fused silica.

3.3.2 Comparison to SiO_2

The large increase in the recovery time in the aerogel sample compared to the ultrafast recovery in SiO_2 led to a more in-depth investigation of multiple aerogel samples. As the density of aerogel is essentially governed by the hole diameter, therefore lower density samples will have strands of SiO_2 which are further apart than that of higher density samples. A range of different density samples were examined from 0.04–0.26 g/cm^3, lineouts showing the recovery of these samples is shown in figure 3.6. A plot of the recovery time for various density samples is shown in figure 3.8, which contains data of the recovery time for various density aerogel samples, a clear trend can be seen that as the aerogel density increases the recovery time of excited conduction band electrons rapidly decreases. A more in-depth invesitigation is required to provide a definitive conclusion, including longer probing windows to resolve the full recovery of the

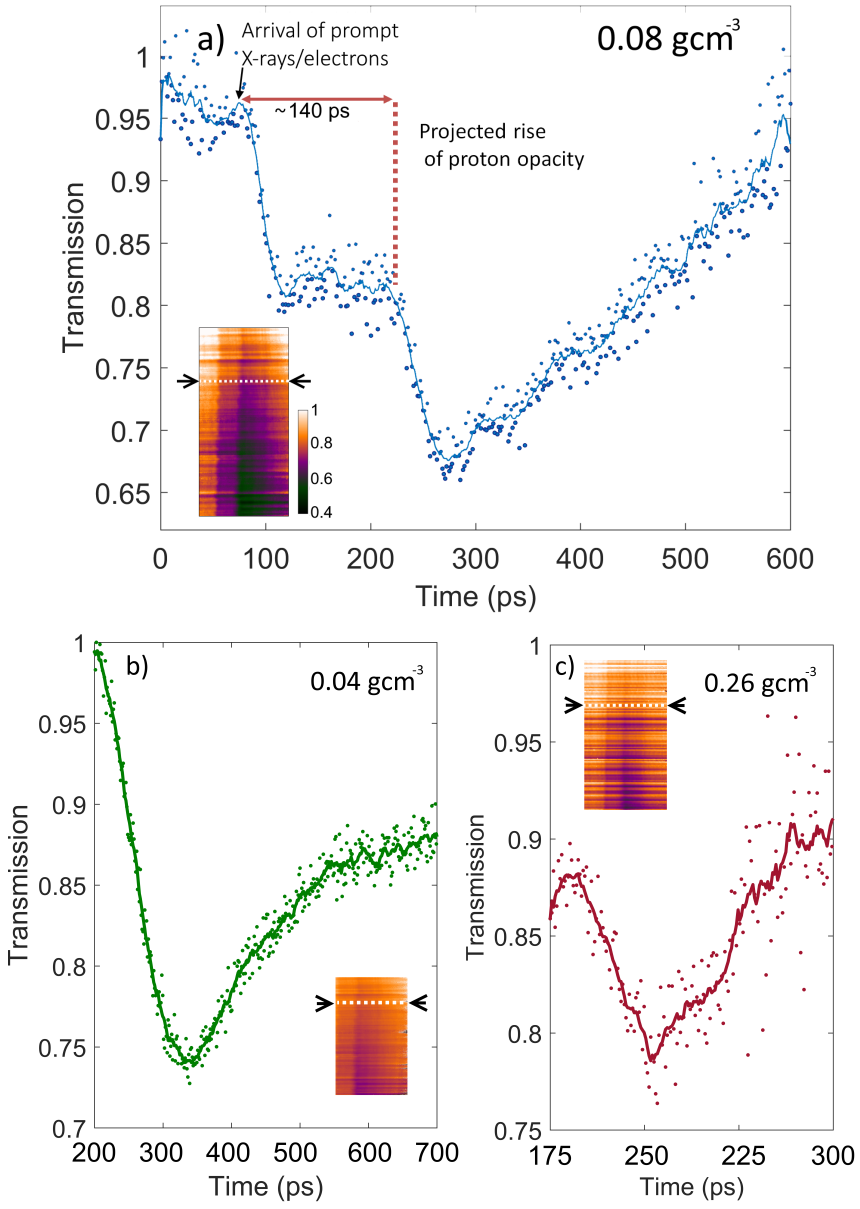

Figure 3.6: Experimental data showing optically streaked images of an ion-induced opacity in a range of aerogel samples. Inset images show the experimentally obtained optical streak with arrows and dotted line indicating the location where the lineout was taken, these have been smoothed with a 4-pixel nearest-neighbour median filter for presentation, lineouts taken from raw image. (a) Opacity in $0.08\,\mathrm{g/cm^{-3}}$ aerogel, in addition to the proton generated opacity there is a step-like feature originating from relativistic electrons created during the TNSA interaction. (b) Opacity in $0.04\,\mathrm{g/cm^{-3}}$ aerogel, this sample exhibited the longest recovery of ≈470 ps (c) Opacity in $0.26\,\mathrm{g/cm^{-3}}$ shows the fastest recovery of the examined samples of 120 ps

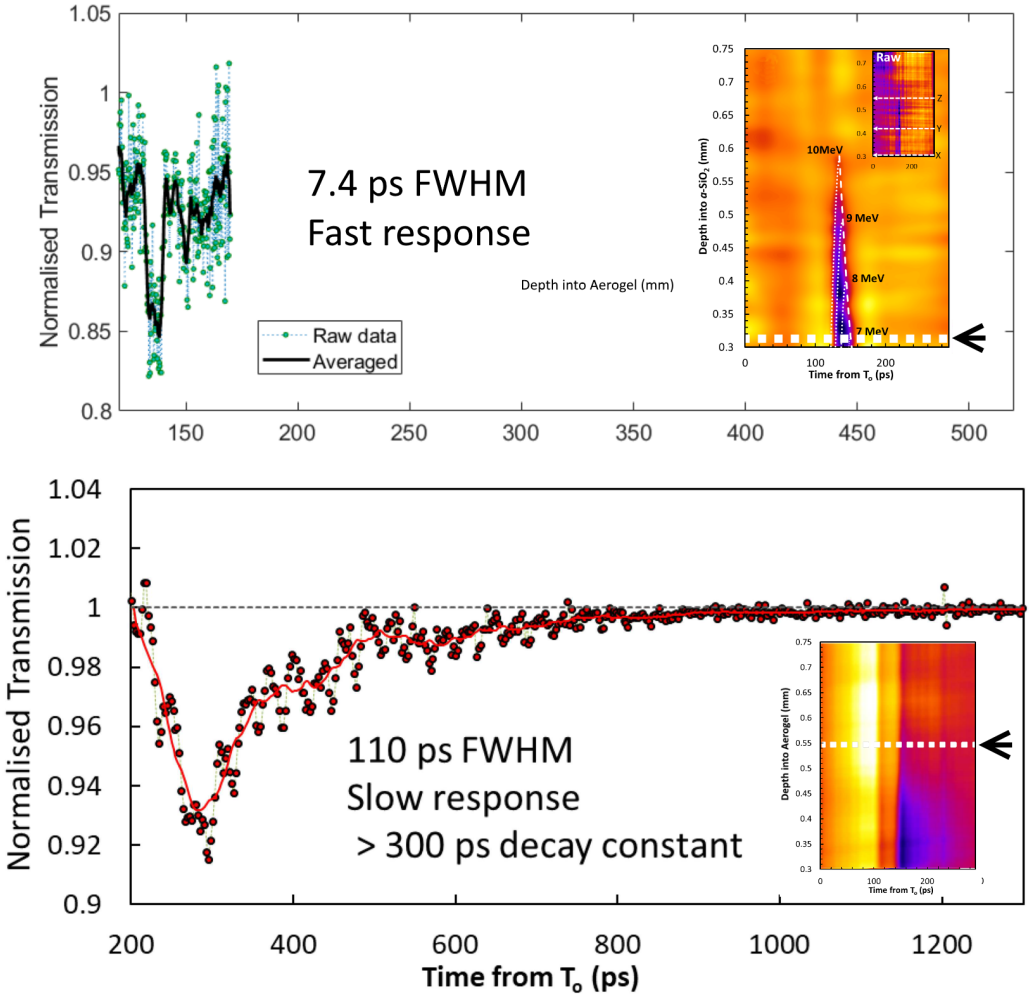

Figure 3.7: Comparison of optically streaked data. **Top** shows data from figure 3.4c of fused silica (amorphous SiO_2), it appears compressed because it is set to the same x-axis scale as **bottom** the optical streak for 0.09 g/cm^3 aerogel which was obtained using a 1 ns probe duration. Gaussian blur performed on images for presentation, all lineouts are taken from the raw image.

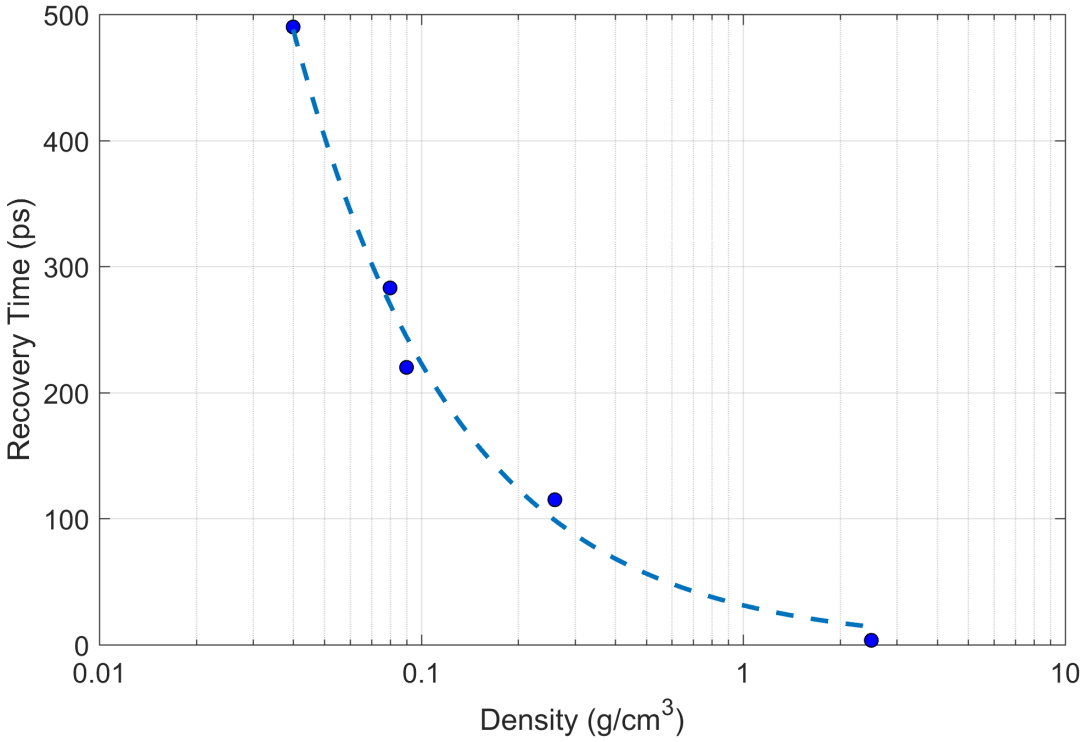

Figure 3.8: Lifetime of the observed opacity in aerogel samples of varying density using data from the previous figures. Also included is the pulse duration measurement in fused silica at a density of 2.66 g/cm^3.

lower density aerogel samples. The possibility of electrons escaping the strands of SiO_2 would lead to an reduction of the recovery time, especially in the more dense samples where the strands are more tightly packed. At the time of writing this thesis a model is under development but not yet complete.

3.4 Summary

In this chapter the evolution of a proton-induced opacity was observed and characterised in various forms of SiO_2. This resulted in the first experimental single shot proton pulse duration measurements enabled through the ultrafast electron de-excitation pathways in SiO_2 Proton pulses as short as 3.5 ps were observed and the ultrafast recovery was attributed to the formation of self-

trapped excitonic states around 150 fs after initial excitation.

Further investigation led to the study of silica aerogel under identical proton pulse conditions to examine the role of electron diffusion on recovery time of the induced opacity. It was found that the opacity lasted orders of magnitude greater in the various aerogel samples than that of amorphous SiO_2 or indeed the measured proton pulse duration. Additionally opacity was generated by the hot electrons from the TNSA interaction arriving before the protons interact with the aerogel sample. An investigation into the recovery of various densities of silica aerogel has indicated a clear trend; i.e. lowering the density of aerogel and hence inhibiting the electron diffusion results in an extension in the recovery time of the opacity, this sample size is relatively small however and may benefit from further examination in future experiments. Additionally, future experiments are planned to be carried out using multiple wavelength probes. On TARANIS for example, frequency quadrupling the fundamental 1053 nm probe would enable direct probing of the lifetime of the self-trapped exciton at 263 nm. This would provide greater insight into the results presented here for the solid SiO_2 sample. Comparison between exciton generation in SiO_2 and the various aerogel densities could help to explain the differing recovery times, i.e. direct observation of STE suppression.

Chapter 4

The Role of Defects in the Extended Recovery of Borosilicate Glass

---

Borosilicate glass (BK7), although mainly composed of SiO_2 has a much lower purity and contains many other oxide compounds, the largest of which being boron oxide (10–20%, full compositional details are available in [78]). It is an extremely common form of glass and is generally chosen as a cheaper alternative to quartz (SiO_2) for cases where purity is not of such great importance. It does however have a high resistance to thermal shock and can be used in a variety of applications due to a high transmission over a broad spectral range 350 nm–2000 nm.

Lately BK7 and other glass composites have become an area of great interest for use in optical waveguides [79], as a result laser-induced defect formation has been studied in great detail. In these studies the photoexcitation of electrons is conducted through the use of tightly focused, short laser pulses and the relaxation of these excited electrons is measured through defect centres in the

material using spectroscopy of their characteristic absorption bands [80–83]. Similar studies have been performed using electron excitation [84] and heavy particle radiation [85, 86] however to date this has yet to be studied using short bursts of protons.

In chapter 3 the ultrafast response of SiO_2 enabled the absolute measurement of the proton pulse duration as 3.5 ps. Using identical proton pulse conditions as in the SiO_2 investigation, this chapter will investigate the evolution of an ion-induced opacity in materials of much lower purity, namely BK7, discussing the vastly extended recovery times of the opacity in the material, far beyond the initial few-ps proton pulse duration.

4.1 Observation of an Ion-induced Opacity in Borosilicate Glass

During the experiment, one the first investigations into the response of BK7 to proton radiation was undertaken using the same 200 ps probe duration as the optical streaks of fused silica and is included here to give an indication of the much longer recovery time of the induced opacity compared to the SiO_2 sample. Figure 4.1 contains an example of the optical streak, including a lineout showing the evolution of the opacity at multiple depths. The white overlay represents calculated proton trajectory curves in BK7 and it clearly indicates that opacity is still existing in the sample beyond the duration of the proton interactions. In addition to the long recovery time, the plot clearly shows a very low transmission of the probe in the sample induced by the proton burst which is maintained for over 150 ps, beyond the observable window of the 200 ps probe. The transmission drops to 46% at the lowest observable depths but gradually increases further into the sample.

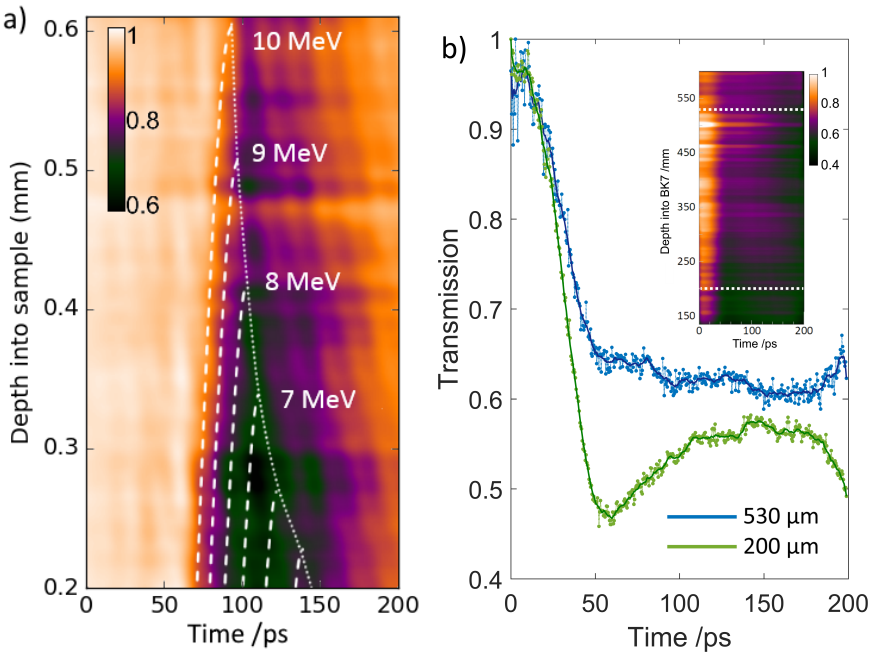

Figure 4.1: Experimentally obtained optical streaking data of opacity in BK7 obtained using a 200 ps probe. (**a**) White dotted overlay shows calculated proton trajectory curves using SRIM. (**b**) Temporal delay of probe has been altered so that rise of opacity starts at the beginning of the observation window, lineouts taken at two depths in the glass clearly indicate the glass does not recover within the 200 ps probe window. A gaussian blur has been performed on the images for presentation, any lineouts have been obtained from the raw image.

It is clear however from this preliminary investigation that (as with the aerogel samples in chapter 3) a longer probe duration is required to fully resolve the dynamics within the glass.

4.1.1 Extended Recovery Beyond the Proton Pulse Duration

Extending the probe duration to a nanosecond permitted observation of the complete recovery of the BK7 glass sample. Figure 4.2 shows data from the experimentally obtained optical streak using the 1 ns probe pulse with lineouts taken at three separate depths to show the evolution of the opacity in different regions of the sample. The data follows the trend indicated in the 200 ps probe

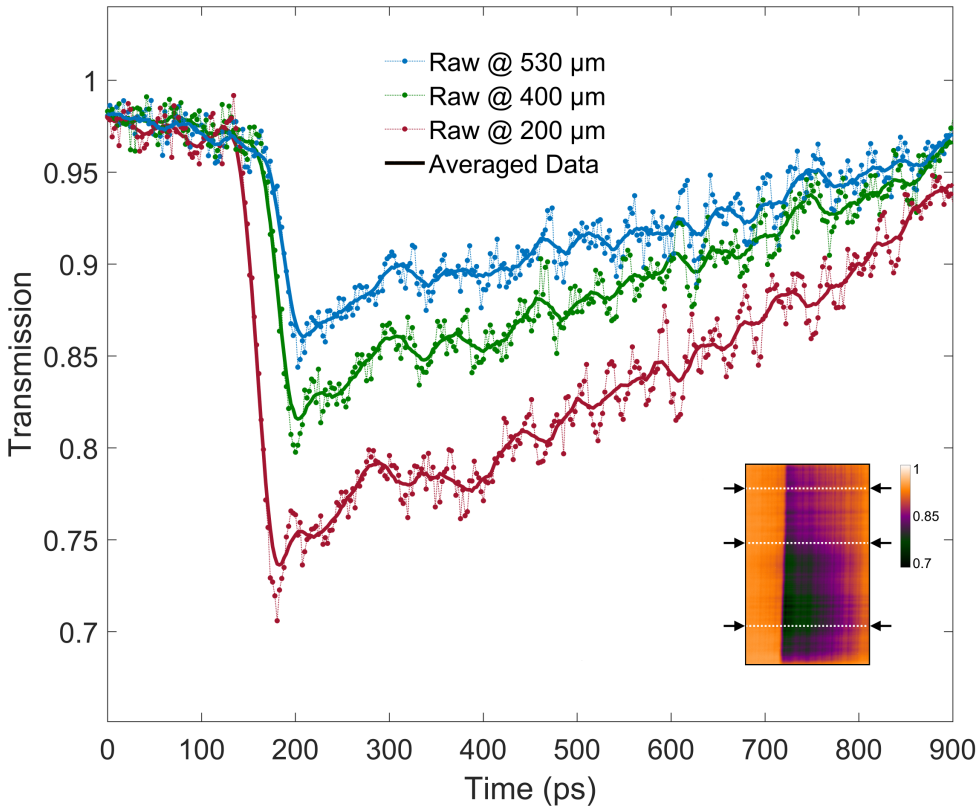

Figure 4.2: Optical streaking data obtained experimentally for BK7 using a 1 eV optical probe. The inset graphic shows the optically streaked image with arrows indicating the location of the lineouts taken. Raw data plotted as points, solid lines denote averaged values. A gaussian blur has been performed on the images for presentation, any lineouts have been obtained from the raw image.

data showing the greatest drop in transmission at low depths in the and a gradual increase towards the end of the maximum observable depth in the glass. At 200 µm where the opacity is at the highest level protons with an energy of 5 MeV and above traverse this region. Due to stopping of lower energy protons in the material, this energy bandwidth narrows further into the sample as discussed in the previous chapters. The decay constant (τ_D, hereby noted as the time taken for the opacity to drop to $1/e$ or $\approx 36.8\%$ of its initial value) remains consistent at the three depths indicated in the figure at 620 ± 10 ps but the total recovery time (τ_R, the time taken for the opacity to recovery by 95% of it's initial value) gradually decreases with depth into the sample. This will be examined in slightly more detail in the following section.

4.1.2 Flux-dependent Response

Due to the nature of proton stopping in matter, proton flux will gradually decrease further into the glass. Figure 4.3 compares the observed recovery time in BK7 to the relative flux of protons, here 1 represents the flux at a depth of 250 µm when the full recovery is able to be observed. As the relative flux decreases, so does the recovery time of the opacity. This indicates two things: firstly the increased flux as expected would lead to a greater number of electronic excitations, resulting in a lower transmission of the probe through the sample and secondly even though a larger initial opacity takes longer to recover than a smaller generated opacity, the rate of recovery is fairly consistent. This would suggest that the recombination processes dictating the recovery are slowing down the decay of electrons to the conduction band.

Previous investigations into the photoexcitation and recovery of BK7 have shown much longer recovery times of up to several nanoseconds [82] however

this could be due the fundamental difference in the nature of the radiation methods used as photoexcitation will produce an extremely homogeneous excitation profile and as previously discussed in chapter 3 inherently leads to a longer relaxation time of the excited electron density.

This alone however does not explain the extremely long lifetime of opacity in comparison to the few-picosecond electron pumping time from the protons. There is an additional mechanism present in materials of low purity (especially multicomponent glasses such as BK7) in the form of intrinsic defects and impurities acting as trapping centres for excited electrons.

4.2 Discussion

This section will provide a brief summary of the key atomic features of glass to provide context for discussion of the recombination of excited electrons. While a detailed account of the atomic structure is beyond the scope of this thesis, it is well covered in literature [87–89].

4.2.1 Defects

The main difference between glass and a crystal is the lack of long range order present in the atomic structure, an example of this is shown in figure 4.4, highlighting the difference between crystalline and amorphous SiO_2. Borosilicate and other silica-based glasses contain additional compounds that modify the atomic network (shown in figure 4.4c). BK7 contains two main types of additions, 'glass forming' ions such as boron that can form part of the main atomic network and 'modifying' ions (typically sodium and aluminium) that

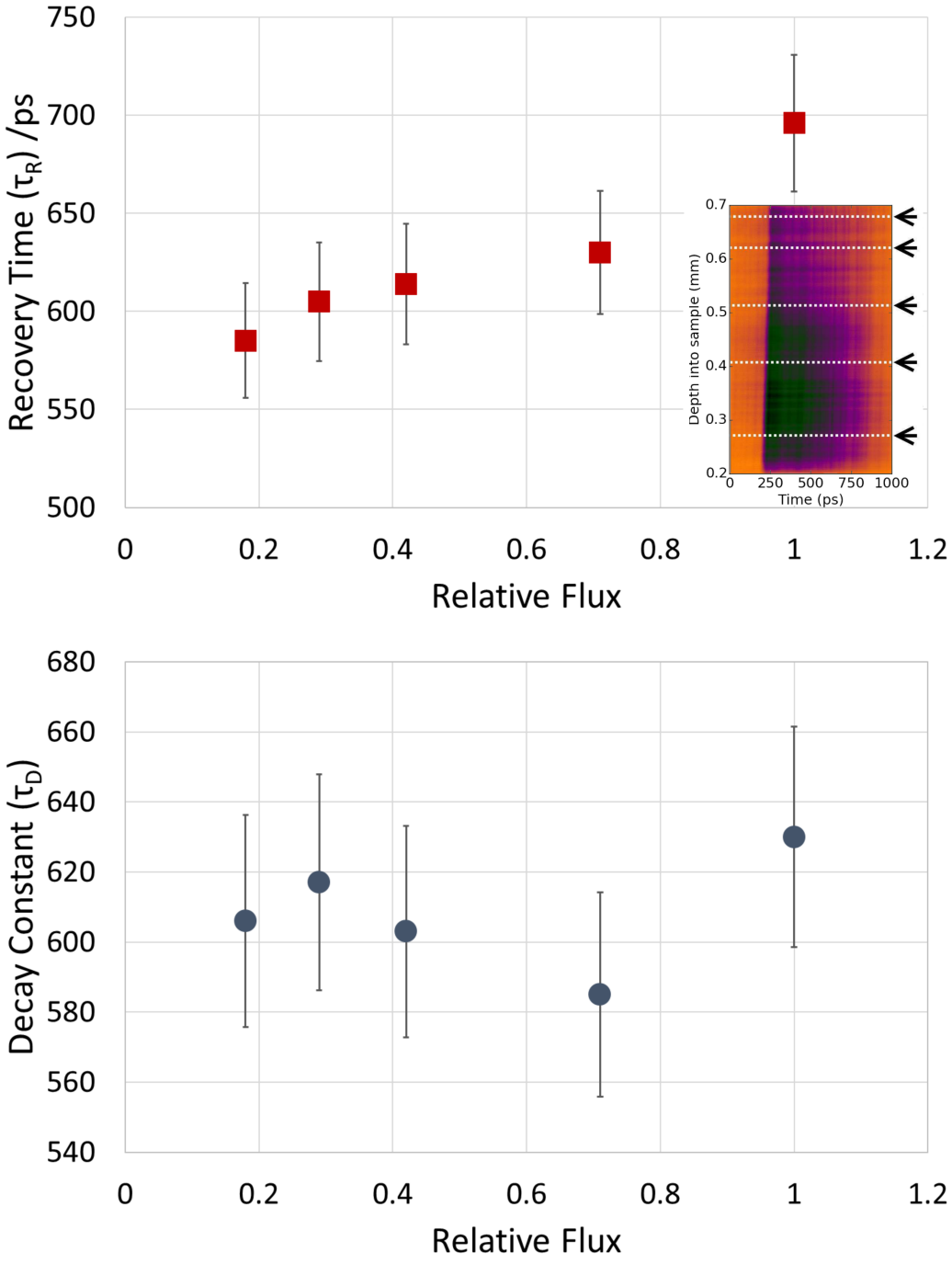

Figure 4.3: Plot showing the effect of proton flux in the recovery of an ion-induced opacity in borosilicate glass. Relative flux here is taken in comparison to the flux at an energy of ≈6 MeV ($10 \pm 2 \times 10^{11}\,\mathrm{cm}^{-2}$).

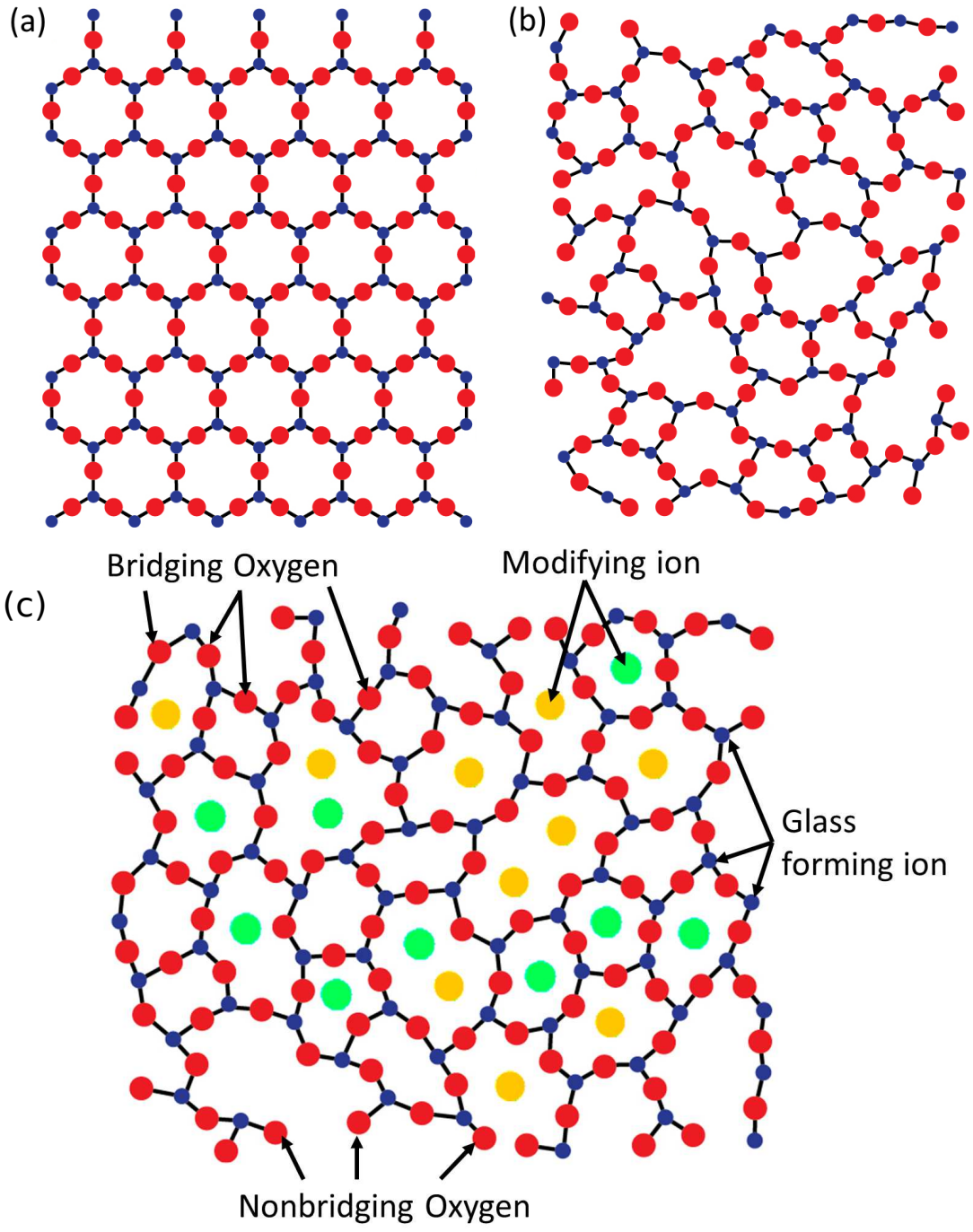

Figure 4.4: Schematic illustration showing the typical structures of the (**a**) long range order in crystalline SiO_2 and (**b**) short range order in a glass. (**c**) shows a modified form of si2lica glass with impurities added to interfere with the formation of the atomic structure. Adapted from [90].

interfere with the atomic structure but do not form part of the glass network. The glass will also contain a mixture of bridging and nonbridging oxygen atoms; a bridging oxygen is bonded to two network forming ions (e.g. Silicon) forming a bridge, whereas a nonbridging oxygen is only bonded to one network forming ion. These additional modifiers are added to provide the glass with specific properties, e.g. the addition of boron gives a high resistance to thermal changes and chemical corrosion, whereas the addition of sodium oxide lowers the melting point of soda-lime glass. Although these additions to the glass provide unique benefits in the applications for the glass, the increase in the complexity of the material introduces a much greater probability for these defects to occur [91].

The concept of energy bands was originally introduced to model electron-hole formation in crystals, however it can also be applied to glasses due to the short-medium range order that it possesses [17, 92]. Modifications are required to the model as instead of bands (i.e. in crystals) a glass will contain levels distributed in energy due to the defect sites and impurities in the material [93], an example of the band structure for glass is shown in figure 4.5. The energy gap between the conduction and valence bands now contain many interstitial levels that are able to trap either electrons or holes during the recombination process. Due to the increased complexity of the material caused by the additional ions and compounds, defect sites are much more prevalent in a glass such as BK7, especially compared to the fused silica discussed in chapter 2. These can then act as trapping sites in the recombination process of excited electrons with holes and typically are divided into four main categories, which are also illustrated in figure 4.6 [87, 89, 94].

- **Vacancies** are caused when an atom is absent from its expected position. Depending on the charge of the atom will be attracted or repulsed. In

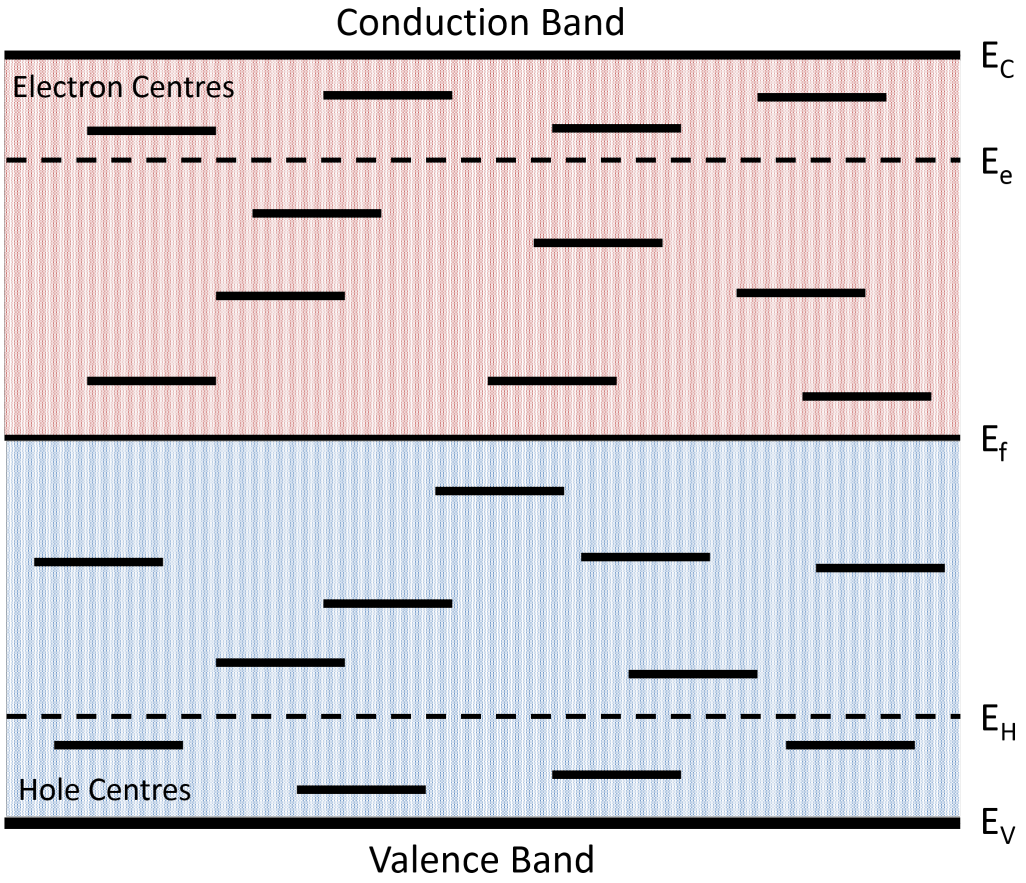

Figure 4.5: A typical energy level diagram of an amorphous material. The interstitial energy levels are the result of defects in the material forming trapping sites for electrons and holes (adapted from [92]).

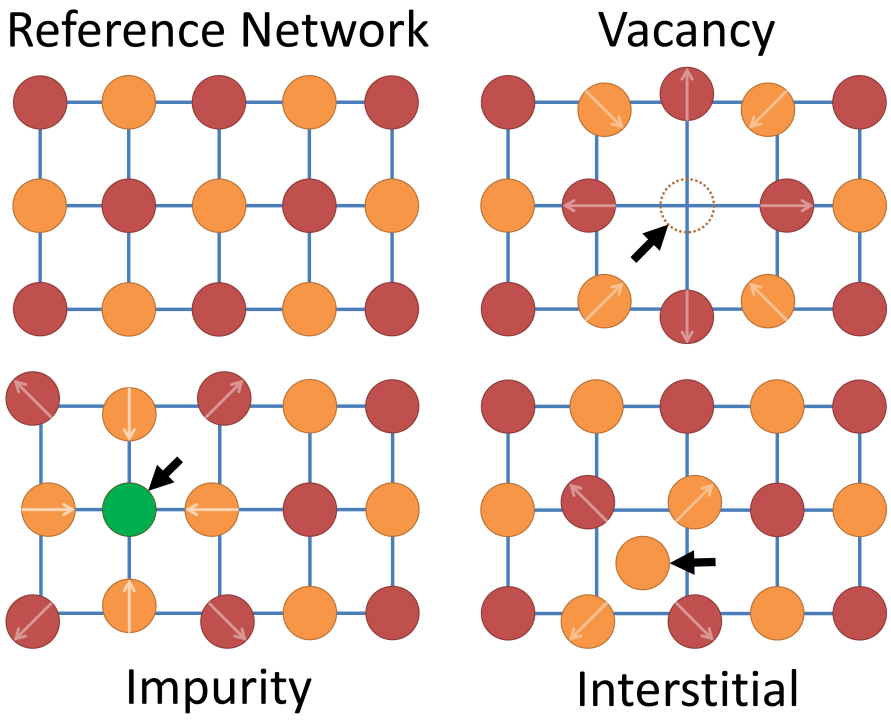

Figure 4.6: Schematic illustration of common categories of defects found in a crystal or glass atomic structure. For the purpose of explanation, the red atoms are considered positively charged (cations) and the orange negative (anions).

figure 4.6 the missing orange anion creates a positive charge relative to the lattice. This results in attraction of the surrounding orange anions and a repulsion of the nearby positive red cations.

- **Impurities**: atoms or compounds present in the glass that were not added intentionally distorts lattice. If the charge of the impurity is even slightly different to the normal atom it will result in a deformation of the lattice.
- **Substitutional** defects are similar to impurities, these are created when a different atom is present to what is generally in the surrounding network.
- **Interstitials** are created when atoms take a position that is normally unoccupied in the structure of the glass (e.g. between lattice positions). This creates a distortion in the local potential as the nearby atoms are repulsed.

In the majority of borosilicate glasses the most common form of defect is the boron-oxygen hole centre (BOHC) [95, 96], this is a result of a boron-oxygen pair becoming dislocated from the lattice which acts as a trapping site for generated holes.

4.2.2 Electron Recombination and Recovery of the Opacity

The experimental observations carried out in this thesis originate from an opacity generated in the material due to an excited electron population in the conduction band, the lifetime of which is essentially dictated by the recombination processes available to these electrons. In chapter 2, the formation of self-trapped excitons $\approx 150\,\text{fs}$ after excitation provided a fast decay channel for these excited electrons so that they no longer contributed to the free-free absorption of

the probe pulse. BK7, due to it being a multicomponent glass contains many defects both inherent to the glass and those induced under irradiation which results in a complex energy level structure similar to that shown in figure 4.5. The electron-hole pairs that are generated by the interaction can recombine in several different ways; direct (or band-to-band) recombination involves the excited electron moving from its state in the conduction band to the associated empty state in the valence band. If this decay pathway is not preferred (e.g. due to a large band gap) recombination will takes place in multiple steps via interstitial energy levels if they are available. These recombinations within the band gap are known as 'trap assisted' or Shockley-Read-Hall (SRH) processes and involve the excited electrons decaying from the conduction band then becoming trapped in the interstitial levels created by defects. This process is the dominant recombination mechanism for indirect band gap materials [97, 98]. Previous studies directly probing some of the defect centres in BK7 found that absorption took place over several nanoseconds [82]. When compared to the results shown here, it is possible that the extremely long recombination time would be responsible for the extended recovery of the opacity as electron decay would be inhibited due to electron/hole trapping in the interstitial levels, leaving a continued excited electron population in the conduction band.

Although the observations made in this thesis do not include an opacity on the order of nanoseconds this could be due to the differences between photoexcitation and proton radiation. As has already been discussed photoexcitation produces a homogeneous dose profile across the sample whereas proton irradiation generates a highly structured energy deposition due to the tracks that are created in the material, this is especially the case at higher energies where the proton flux decreases. This could lead to an explanation as to why the recovery times increase at lower depth as the proton dose distribution begins to

homogenise due to the much higher flux in that volume of the sample.

Finally, opacity in an additional multicomponent glass was briefly examined. Soda-lime glass (also known as float glass) is abundant with impurities, containing many more compounds than BK7 and at higher concentrations (mainly 12% Na_2O, 10% CaO). Therefore the amount of defects and trapping sites would be much greater. The optical streak of opacity generated in the soda-lime glass is shown in figure 4.7 alongside a comparison to the BK7 data. It clearly shows that the transmission of the generated opacity is much less than in BK7 and the lifetime extends beyond the observable window of the nanosecond probe pulse.

4.3 Summary

This chapter has investigated the response of borosilicate glass to few-picosecond proton bursts through the observation of a proton-induced opacity. It was found that the recovery time of BK7 is orders of magnitude longer than the pulse duration and previously observed opacity in SiO_2. This is believed to be related to electron trapping in the interstitial levels within the band gap of the material caused by defects both induced by the proton pulse and those inherent to the multicomponent structure of the material.

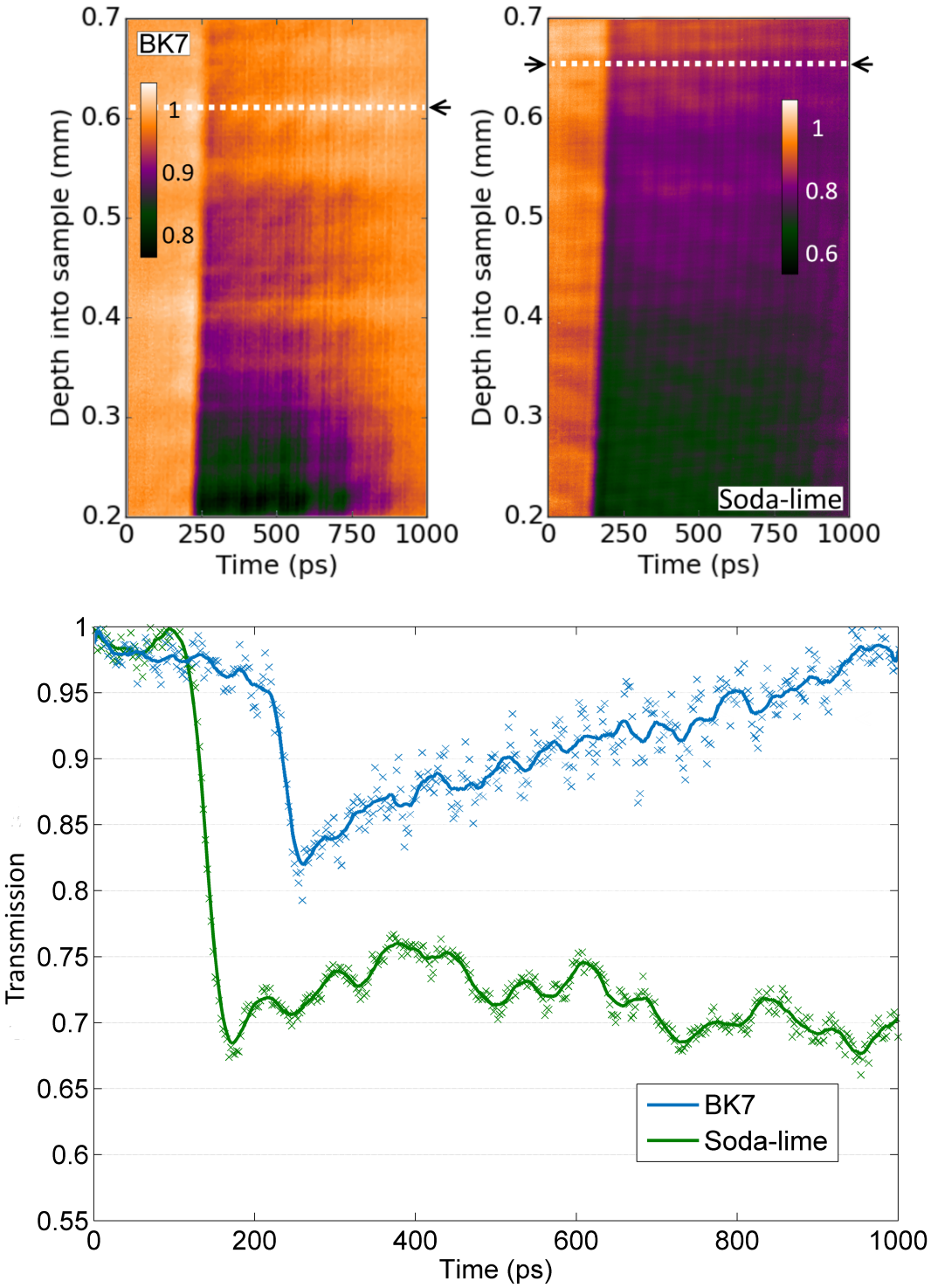

Figure 4.7: Experimental data showing evolution of opacity in BK7 and Soda-lime glass. The lineouts are taken at slightly different depths to account for for the difference in stopping of protons due to the densities of the two glass samples. A gaussian blur has been performed on the images for presentation, any lineouts have been obtained from the raw image.

Chapter 5

Electron Solvation Dynamics in H_2O During Ultrafast Pulsed-ion Radiolysis

---

Previous chapters have exclusively focused on the observation of ion-induced dynamics within solid materials. In chapter 3 ultrafast trapping processes in the formation of self-trapped excitons enabled observation of the TNSA proton pulse duration. One of the advantages to the optical streaking technique is the ability to use a wide variety of samples with minimal work required for implementation. This chapter will examine another trapping mechanism–the formation of solvated electrons in liquid water after irradiation using identical proton pulse conditions as outlined in the previous investigations.

5.1 The Solvated Electron

Initially discovered in 1962 by Hart and Boag [99], the solvated (or hydrated) electron has been extensively studied in the past several decades due to its im-

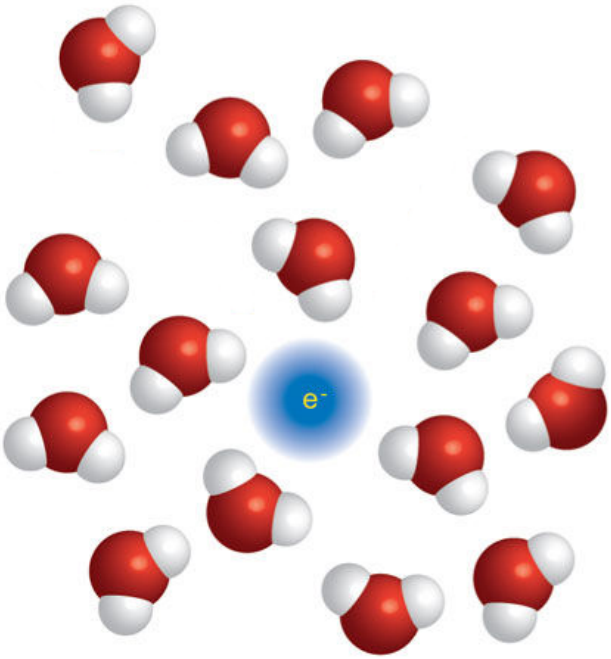

Figure 5.1: Schematic of solvated electron. Free electrons are generated through the interaction of ionising radiation with water. The surrounding water molecules then move to trap the electron through dipolar interactions.

portance in many applications from nuclear reactors to biology and medicine [100]. A large area of focus lies in the role of the solvated electron in the radiation chemistry of water and radiation therapy. These studies are typically performed with either electrons or ions sourced from radiofrequency accelerators in combination with chemical scavenging techniques, where radiolytic yields are examined in the water after exposure to the ionising radiation [9, 12, 101]. Although an effective technique there are some drawbacks to the chemical scavenging method, mainly the requirement for the addition of substances which allow the concentration of radiolytic yields to be determined and for picosecond timescales there is an added degree of uncertainty due to the concentration of scavenger that is required [9]. The merits of laser-driven ion acceleration have already been discussed in the previous chapters alongside the optical streaking technique, however the major advantage here lies in the ability to study the

ionisation dynamics of pure water with few-picosecond resolution.

Observation of the solvated electron dynamics is enabled due to its wide absorption band, the high absorptivity of which makes it easy to detect even at low concentrations [12, 102, 103]. Their formation process begins with the interaction between ionising radiation (e.g. protons, but also X-rays and electrons) and water molecules. As the protons propagate into the water, they deposit energy by ionising the water molecules, producing a radical ion and a free electron

$$H_2O \xrightarrow{\text{radiation}} H_2O^+ + e^-$$

Through dipolar interactions the free electron is captured by the water, becoming solvated (as in figure 5.1).

$$e^- + H_2O \longrightarrow e_{aq}$$

The production of the solvated electron (e_{aq}) can lead to many different reactions producing free radicals, some of which are

$$H_2O\cdot^+ \longrightarrow H^+ + HO\cdot$$

$$e_{aq} + e_{aq} + 2\,H_2O \longrightarrow H_2 + 2\,OH^-$$

$$HO\cdot + HO\cdot \longrightarrow H_2O_2$$

The formation of the solvated electron is the prototypical process for radiation chemistry in water. Study of their formation is important to understand the effects of ionising radiation in the treatment of cancer, as the majority of energy deposited in a cell by radiation is absorbed by water. The free radicals which are produced can react chemically with DNA, leading to damage of the DNA strands and possible cell death.

5.2 Experimental Results

5.2.1 Required Modifications to the Experimental Setup

To enable the investigation of liquid water, slight modifications were required to the experimental setup. Replacing the solid materials with a water cell resulted in changes to the geometry of the setup previously outlined in chapter 2. The main change was the increase in propagation distance of the proton burst before reaching the water cell, resulting in an increase in the arrival time of the protons relative to the prompt electrons and X-rays as well as the introduction of a 200 µm teflon window that the protons travel through before interacting with the water. This teflon window results in a filtering of proton energies below $\approx 5\,\mathrm{MeV}$. A sketch of the water cell is contained figure 5.2.

5.2.2 Examining the Rising Time of the Opacity

The focus of this chapter is of the formation of solvated electrons. This is investigated through transient absorption spectroscopy using the 1053 nm probe of TARANIS with a chirped pulse duration of 1 ns. Figures 5.3a and 5.3b show experimentally obtained optical streaks of opacity generated in water by proton

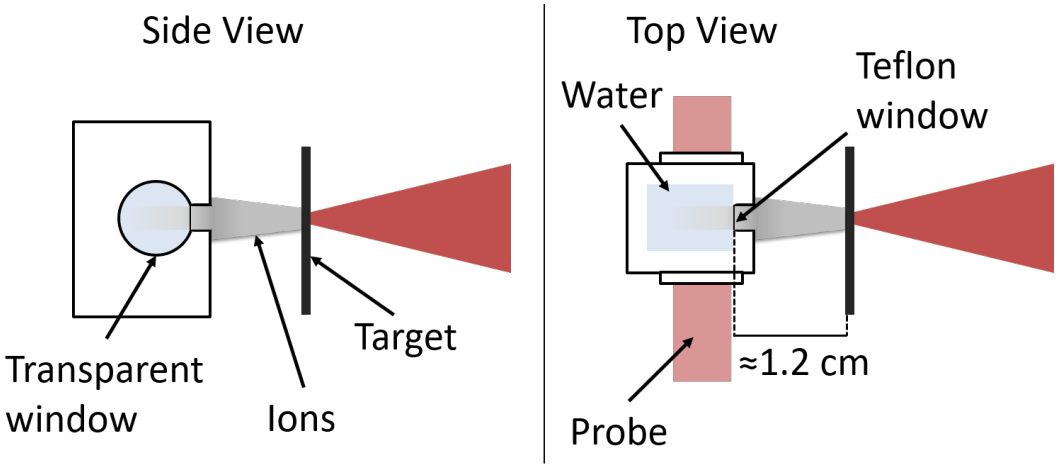

Figure 5.2: Schematic of water cell used in experiment. Everything is identical to the setup outlined in chapter 2 except for a change in the target–sample geometry. Due to the dimensions of the water cell the protons propagate a distance of 1.2 cm in vacuum before reaching a 200 µm teflon window.

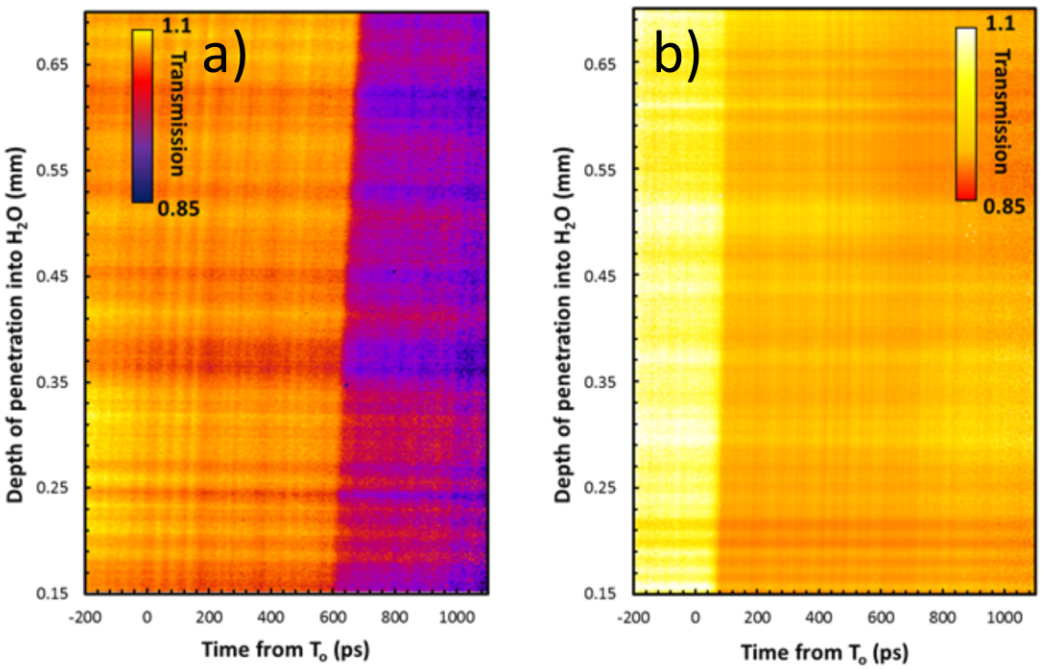

Figure 5.3: Experimentally obtained optical streaks of opacity in water. (a) from interaction with the proton pulse and (b) from electron/X-ray interactions only. A gaussian blur has been performed on the images for presentation.

interactions and prompt electrons/X-rays respectively (here the production of TNSA protons was suppressed due to the presence of a laser pre-pulse), where the difference in the start of the opacity is caused by the difference in the arrival times of the relativistic electrons/X-rays and much slower protons after propagating the 1.2 cm of vacuum and the teflon window. Lineouts of the two images (shown in figure 5.4) reveal a significant increase in the onset of opacity caused by the proton interactions compared to the electron/X-ray signal. The rising time of the opacity caused by protons (ΔDp) is on the order of >190 ps while <10 ps for the electrons/X-rays only (ΔDx). Here the rise time of the induced opacity is measured after the expected arrival time of the proton pulse which was obtained using time of flight calculations for the expected proton energies.

5.2.3 The Role of LET in the Formation of Solvated Electrons

Investigations into ion-induced shockwaves caused by high LET of heavy particle radiation (typically carbon, $\approx 900\,\mathrm{eV\,nm^{-1}}$) have been predicted theoretically and studied for the thermomechanical damage that can be inflicted to DNA [104, 105]. The shockwaves are formed due to the very quick energy deposition of the heavy particles (around 50 fs after the ion passes), this rapid deposition of dose imparts a large thermal energy to the surrounding water molecules and the high energy gradients generate a strong explosion as the water molecules are pushed radially outwards from the proton track. Recent Molecular Dynamic (MD) simulations show evidence of this process in the Bragg region of protons in water, these plots are shown in figure 5.7. Surrounding a 1 MeV proton track outside the Bragg region there is negligible change in the local density of the water, however in the area around an 80 keV proton

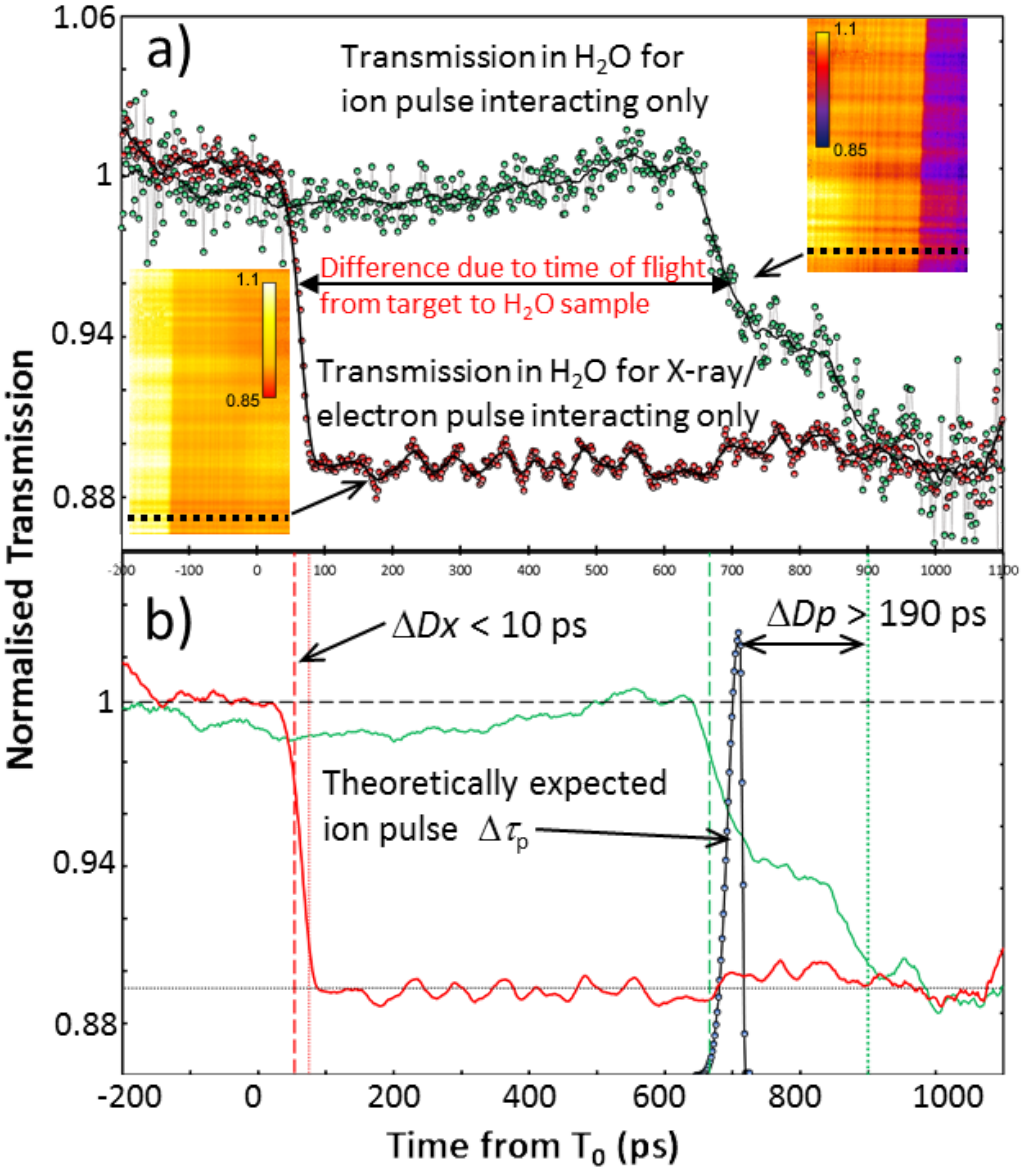

Figure 5.4: Comparison between opacity generated by the proton interaction and X-ray/electrons. Lineouts are taken at the dashed lines of the inset images at a depth of 200 µm, images are the same as those in figure 5.3. A gaussian blur has been performed on the images for presentation, any lineouts have been obtained from the raw image.

in the Bragg region a large thermal spike is observed in a 2 nm region and is shown in figure 5.6. This temperature imparts a large kinetic energy to these molecules (compared to the binding energy of a solvated electron of ≈3.7 eV), which evolves over tens of picoseconds. Meanwhile a cavity begins to form as the water molecules travel outwards from the track region over ≈ 230 ps, the size of which is approximately a factor of ten larger than the size of a water molecule at 2.75 Å. A combination of these two phenomena result in a delay in the solvation process of the generated free electrons in water. The high initial energy of the water molecules will prevent solvated electrons from forming as it is much greater than their binding energy, the subsequent motion of the bulk H_2O around the Bragg region of the proton track removes water molecules in the local area further inhibiting the formation of solvated electrons as there is an absence of molecules for trapping of the free electrons to occur, resulting in the gradual onset of opacity as observed in figures 5.3 and 5.4. A schematic of this process is shown in figure 5.5.

Outside the Bragg region of the proton tracks, significantly less energy is lost to the surrounding water molecules (similar to electron/X-ray irradiation). This does not result in the formation of a cavity, enabling the trapping processes to occur unhindered and solvated electrons to form, as is seen in the very sharp rising time of opacity generated by the electron and X-ray interactions.

Stopping in the material has been discussed in previous chapters as a way to filter proton energies. Similarly in water – observations at greater depth correspond to higher maximum proton energies. The LET for a range of initial proton energies is shown in figure 5.8 indicating significant variation in the LET inside and outside of the Bragg region. This is also represented in the observed experimental data of opacity generated by the protons. Lineouts of the data taken at different depths into the sample show significant variation in the onset

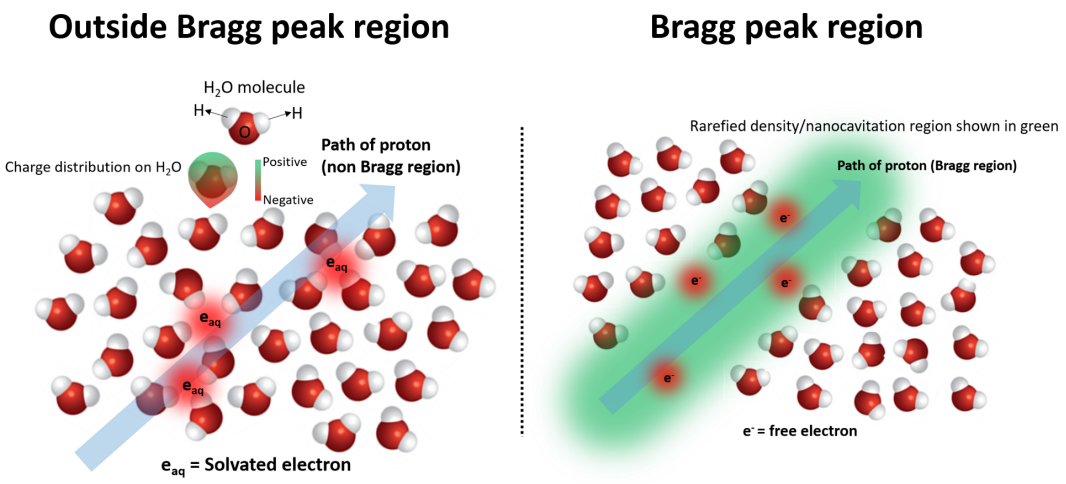

Figure 5.5: Schematic of cavity formation in H_2O. Outside the Bragg region, the low LET radiation does not produce a cavitation, enabling the formation of solvated electrons from the free electrons created during the interaction. In the Bragg region however, a cavity is produced by the high LET radiation removing water molecules from the local area and inhibiting the formation of solvated electrons.

of the opacity from 230 ps at the lowest observable depths (and highest LET) to $\approx$ 50 ps at the greatest depths (i.e. lowest LET).

5.3 Summary

In this chapter, transient absorption spectroscopy has been used to study the formation of solvated electrons in liquid water. Differences in the rising time of opacity has been investigated between proton and X-ray/electron irradiation, where proton irradiation shows dramatic increase in the onset of opacity compared to electrons and X-rays only. Classical Molecular Dynamics simulations indicate the formation of nanoscale cavities around the Bragg region of the proton track which is expected to evolve over several hundred picoseconds and would inhibit the formation of the solvated electrons due to both the large initial energy generated by the thermal spike in the water and the resulting bulk

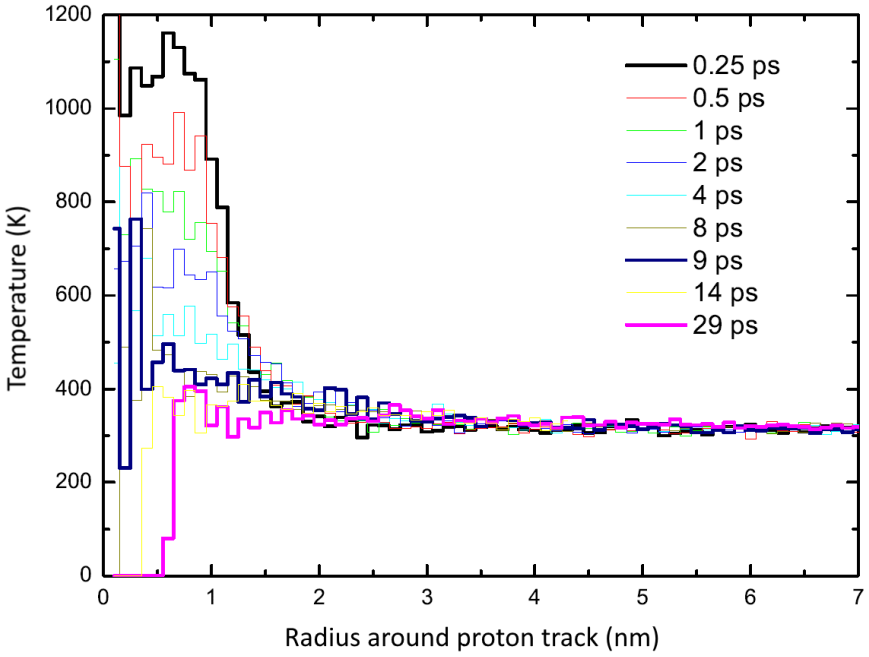

Figure 5.6: Temperature as a function of radius around the track of an 80 keV proton in the Bragg region obtained from Classical Molecular Dynamics simulations. Courtesy of P. de Vera.

movement of water molecules away from the proton track.

Additionally a large variation in the onset of opacity was observed in the optically streaked proton data. At low depths in water the largest rising time of opacity was observed, conversely at the greatest depth in water the fastest rise time was observed, approaching the fast (<10 ps) onset of opacity in the electron and X-ray data.

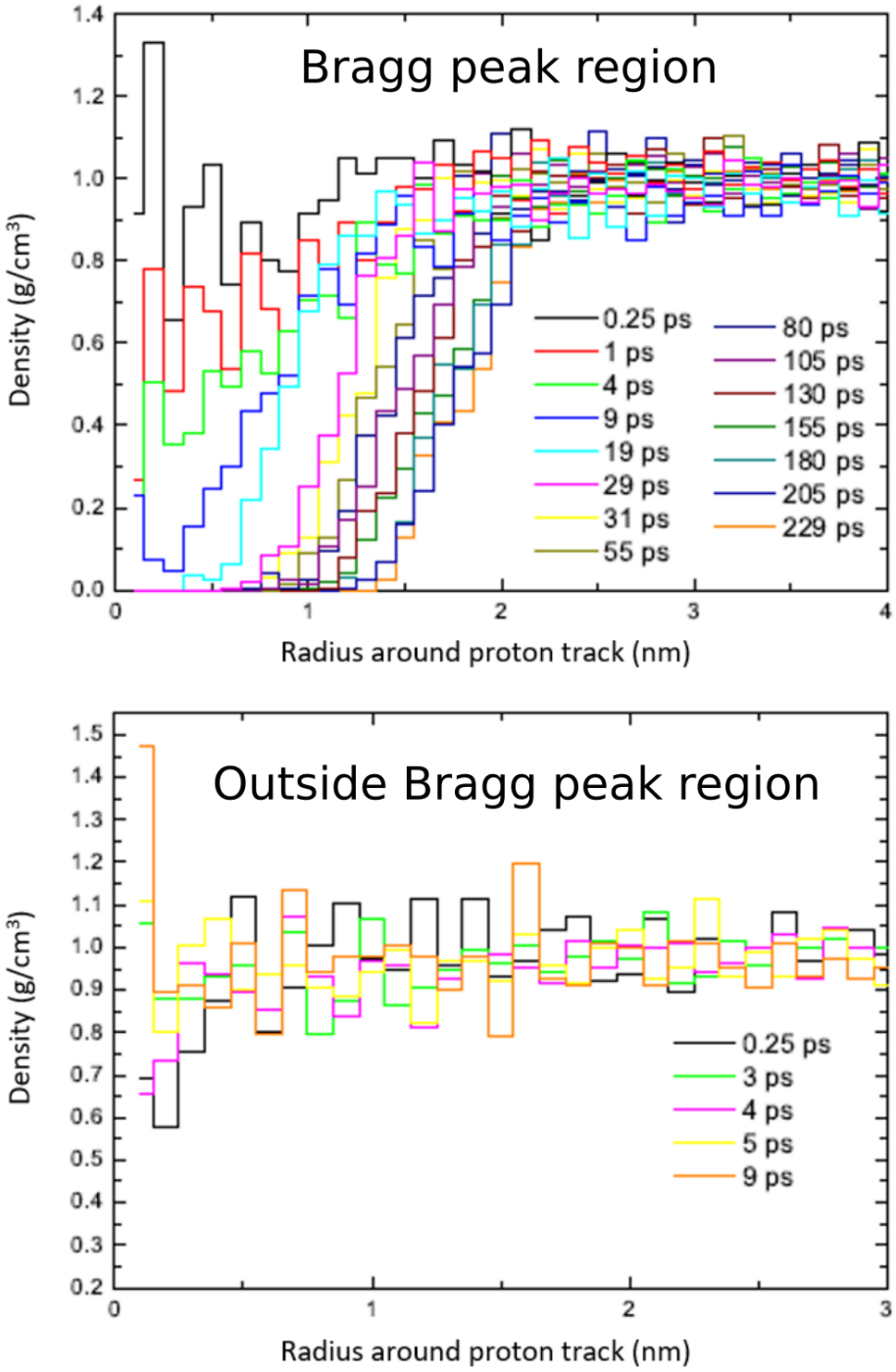

Figure 5.7: Classical Molecular Dynamics (MD) simulations showing (**top**) evidence of nanoscale cavity formation in the Bragg region of 80 keV protons and (**bottom**) negligible changes in the track region of 1 MeV protons in H_2O. Courtesy of P. de Vera.

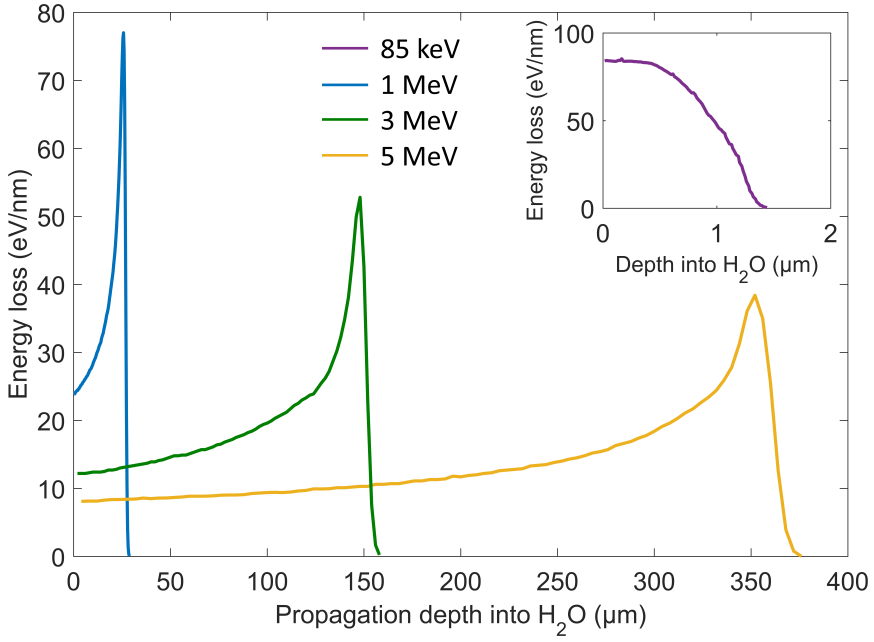

Figure 5.8: Comparing the linear energy transfer (energy loss) of protons in H_2O with different initial energies.

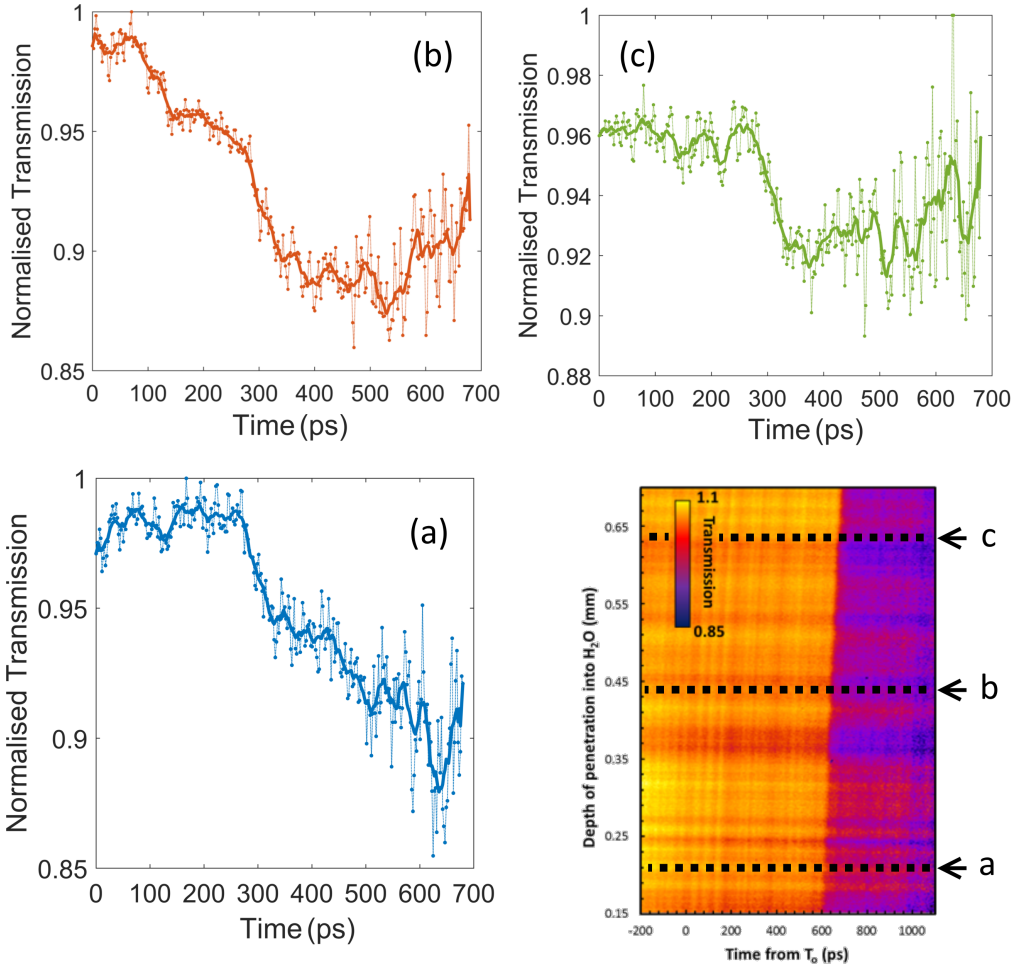

Figure 5.9: Lineouts taken at successive depths a, b and c showing the onset of opacity in the water sample. Rising time of the generated opacity due to solvated electrons gradually decreases with depth. At the lowest depths (a) the opacity takes >190 ps to reach a maximum, whereas (b) corresponds to 85 ps and (c) 50 ps.

Chapter 6

Radiation-induced Polarisation Effects in Lithium Niobate

The bulk of this thesis has outlined experimental observations of a transient opacity generated in various samples, both solid and liquid, from the interaction of ionising radiation. This work will discuss experimental observations of ionisation dynamics in lithium niobate ($LiNbO_3$). Although the core experimental technique is the same as previous chapters, the observed 'opacity' in $LiNbO_3$ is instead from changes in the polarisation of the probe due to dynamics within the crystal after irradiation. This chapter will discuss the observations made in lithium niobate, highlighting another application of the optical streaking technique.

6.1 Introduction

Lithium niobate crystals were first obtained from a melt solution in 1949 by Matthias and Remeika [106]. Investigations revealed that the material proved

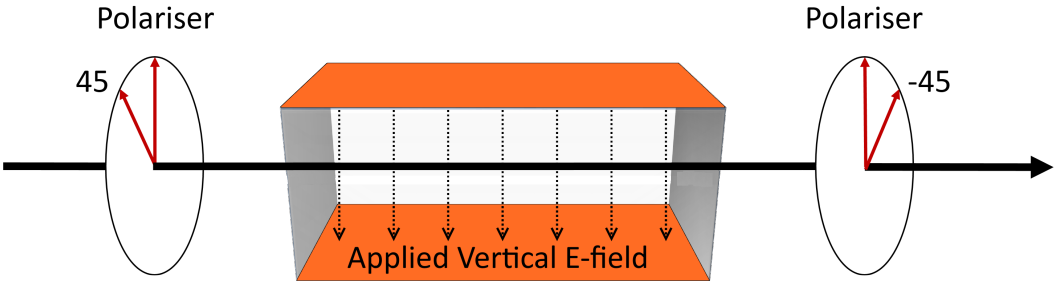

Figure 6.1: Schematic of a simple amplitude monitor. An electro-optic crystal such as $LiNbO_3$ is placed between two crossed polarisers. A voltage is applied to electrodes attached to the crystal controlling the exit polarisation of the light.

highly promising for use in optical applications. Today, lithium niobate ($LiNbO_3$) can be grown as large single crystals and is a material most often exploited for it's electro-optical properties, commonly used in telecommunications devices or as components in laser technology, such as the Pockels cell. When incident light is transmitted through an electro-optic crystal, the phase of the output light can be changed depending on the orientation of the crystal and the voltage applied to it – i.e. the refractive index of the crystal can be controlled electronically. In addition to the electro-optic effect, lithium niobate exhibits strong piezoelectric properties, which is the ability of the crystal to generate a charge via applied mechanical stress and the reverse, where an applied electric field will induce a deformation of the crystal. This section will briefly outline the electro-optic effect as it is relevant to the experimental observations discussed later in this chapter.

6.1.1 The Pockels Effect

First described 1906 by Friedrich Pockels. It is also known as the linear electro-optic effect, where the change in the refractive index n of a medium is directly proportional to the strength of the applied electric field E. This is due to a

movement of the constituent ions in the crystal. In general, the refractive index of an electro-optic material as a function of the applied electric field can be expressed in a Taylor's series [107]

$$n(E) = n - \frac{1}{2} r n_0^3 E - \frac{1}{2} \sigma n_0^3 E^2 + \dots \tag{6.1}$$

where n_0 is the unperturbed refractive index, r and σ are known as the electro-optic and stress coefficients respectively and are represented by a third-rank tensor which is dependent on the properties of the crystal. In $LiNbO_3$ this takes the form

$$\overrightarrow{r} = \begin{pmatrix} 0 & -r_{22} & r_{13} \\ 0 & r_{22} & r_{13} \\ 0 & 0 & r_{33} \\ 0 & r_{51} & 0 \\ r_{51} & 0 & 0 \\ -r_{22} & 0 & 0 \end{pmatrix} \tag{6.2}$$

typical values for r_{ij} lie between 1–100 $\mathrm{pm\,V^{-1}}$. In many electro-optic materials such as lithium niobate, the 3rd and higher terms in equation 6.1 are typically $\ll n_0$ and can be safely discarded, leaving

$$n(E) = n_0 - \frac{1}{2} r n_0^3 E \tag{6.3}$$

or, alternatively

$$\Delta n = -\frac{n_0^3}{2} r E \tag{6.4}$$

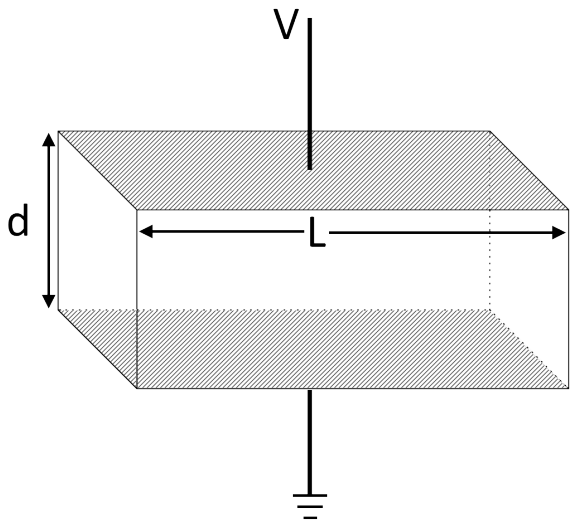

Figure 6.2: Schematic setup of an electro optic crystal for use as a transverse amplitude modulator. Adapted from [108].

As the electro-optic coefficient r is very small, even large electric fields on the order of $1\,\mathrm{MV\,m^{-1}}$ will only create refractive index change of about 0.01%. Looking at the phase change $\Delta\phi$ that is induced as a result of this, (e.g. in a wave polarised along x and y travelling in the z direction) the indices of refraction relevant to phase change are n_x and n_y. In a crystal similar to figure 6.1 the wave will experience a phase change [108]

$$\Delta\phi = \frac{2\pi L}{\lambda}(n_x - n_y) = \frac{L}{d}\frac{4\pi n_0^3 r_{22} V}{\lambda} \tag{6.5}$$

here L is the distance through which the wave propagates, V is the applied voltage and d is the distance across the crystal through which the voltage is applied (shown in figure 6.2). Additionally it is worth noting that the electro-optic coefficient will change depending on the crystal axis through which the field is applied. This together with the crystal dimensions contribute a large amount to the strength of field required to induce a phase change. Although

Δn is very small, simply due to the distance the wave will propagate a large phase change can still be induced (e.g. for a wavelength of 1053 nm, a refractive index change of 10^{-5} over a distance of 1 mm will produce a phase change of 2π). The operating speed of a typical electro-optic modulator is limited by both electrical capacitive effects of the crystal and also the time taken for the light to traverse the material. If the applied electric field varies significantly over the time taken for the optical wave to pass through the crystal then the wave will be subject to different electric fields and therefore phase changes.

6.2 Experimental Results

Initial investigation of the lithium niobate sample began using the nanosecond probing window. The resulting optical streak is shown in figure 6.3 with the lineout taken at 500 µm. Here an oscillating 'opacity' is observed over the entire duration of the probe pulse. Other than the periodic nature of the signal, there are a few key issues when applying the typical picture of opacity to this observation. Firstly, as the measured cut off energy of the protons was 10 MeV and the density of lithium niobate is much higher than the other samples investigated ($4.63\,\mathrm{g/cm^3}$ the direct opacity generated in the crystal would not exist further than $\approx 400\,\mu\mathrm{m}$ but can be seen at all observable depths in the crystal. A possible explanation for periodic nature of the signal was attributed to changes in polarisation of the probe beam, taking into account the efficiency of the spectrometer grating under S and P polarised light (parallel or perpendicular to grating surface respectively) as shown in figure 6.4. The initially P-polarised probe undergoes phase changes in the $LiNbO_3$ crystal while it is being irradiated. As the polarisation begins to rotate towards S, the signal drops due to the significantly reduced efficiency (about 30% compared to P-polarised light).

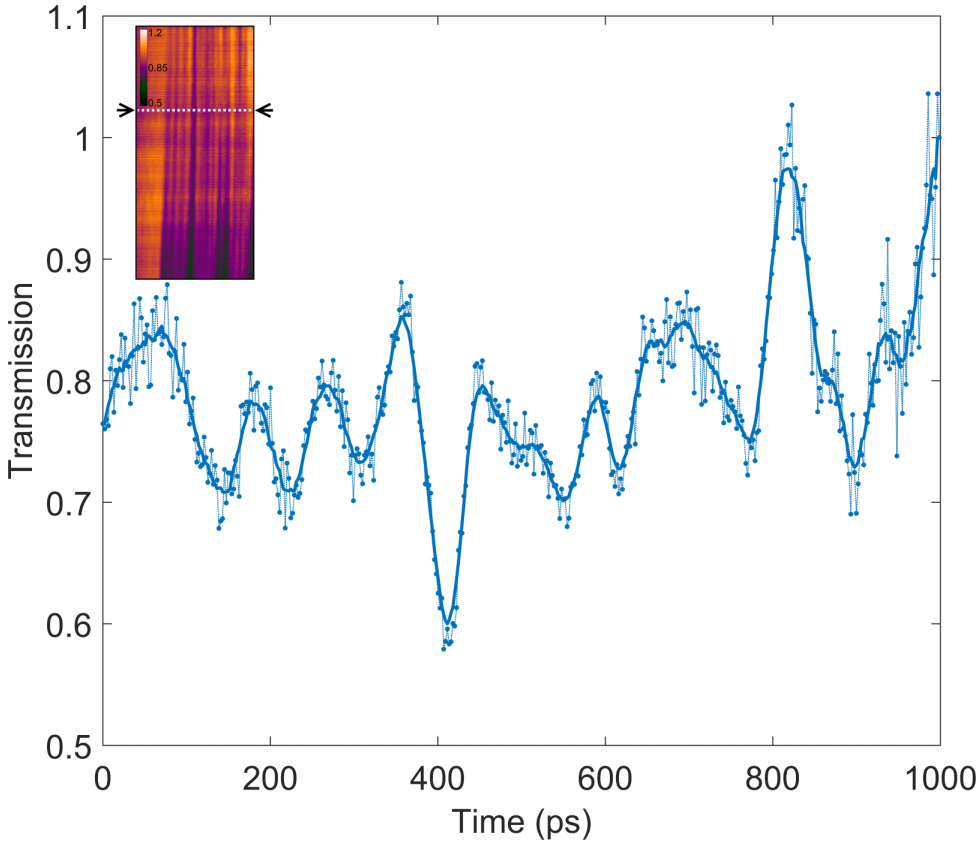

Figure 6.3: Experimentally obtained optical streaking data of ionisation dynamics in $LiNbO_3$. Inset image shows raw experimental data with lineout taken at 500 µm

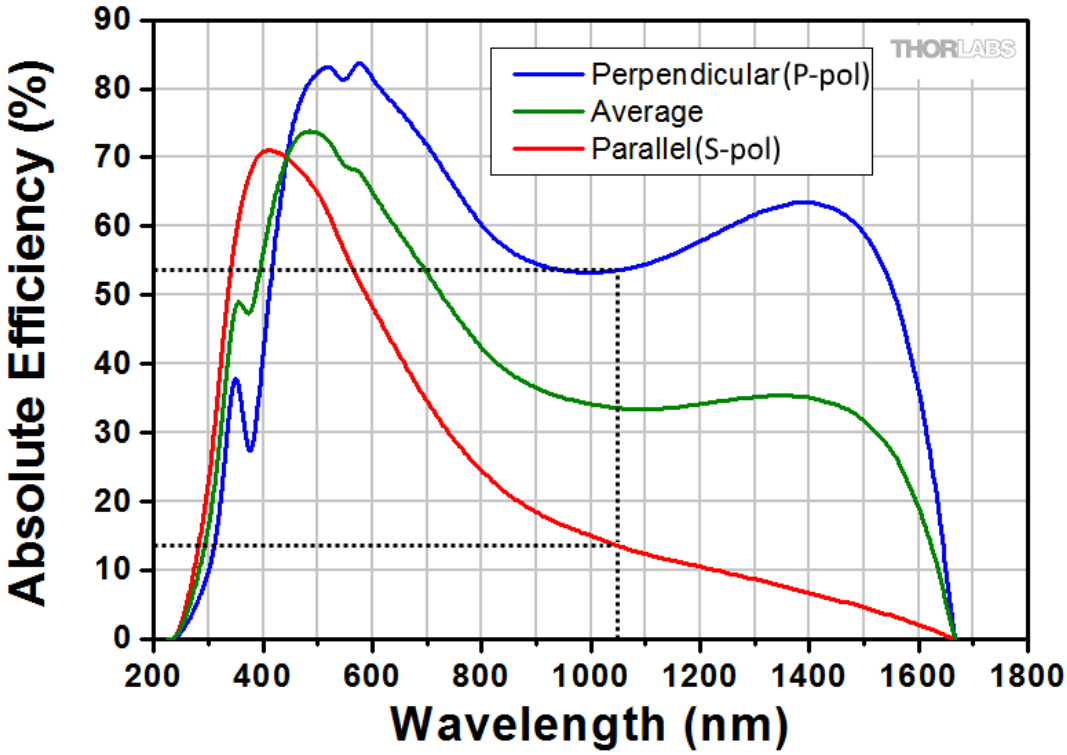

Figure 6.4: Grating efficiency at different polarisation states for a 1200 lines/mm diffraction grating blazed at 500 nm. From Thorlabs [109]

This oscillation then continues over the entire duration of the probe pulse.

6.2.1 Simultaneous Polarisation Measurements

To further investigate the polarisation rotation dynamics within irradiated $LiNbO_3$ modifications were performed to the probe line before the spectrometer. A polarising beamsplitting cube was placed in the probe line after the sample to separate the probe line into S and P components of polarisation that separately enter the spectrometer, resulting in two optical streaks on the CCD of the same interaction region. A half-wave plate placed in the probe line before the sample enables the state of polarisation to be defined before passing through the $LiNbO_3$. If the beam was P-polarised for example, signal will only appear in

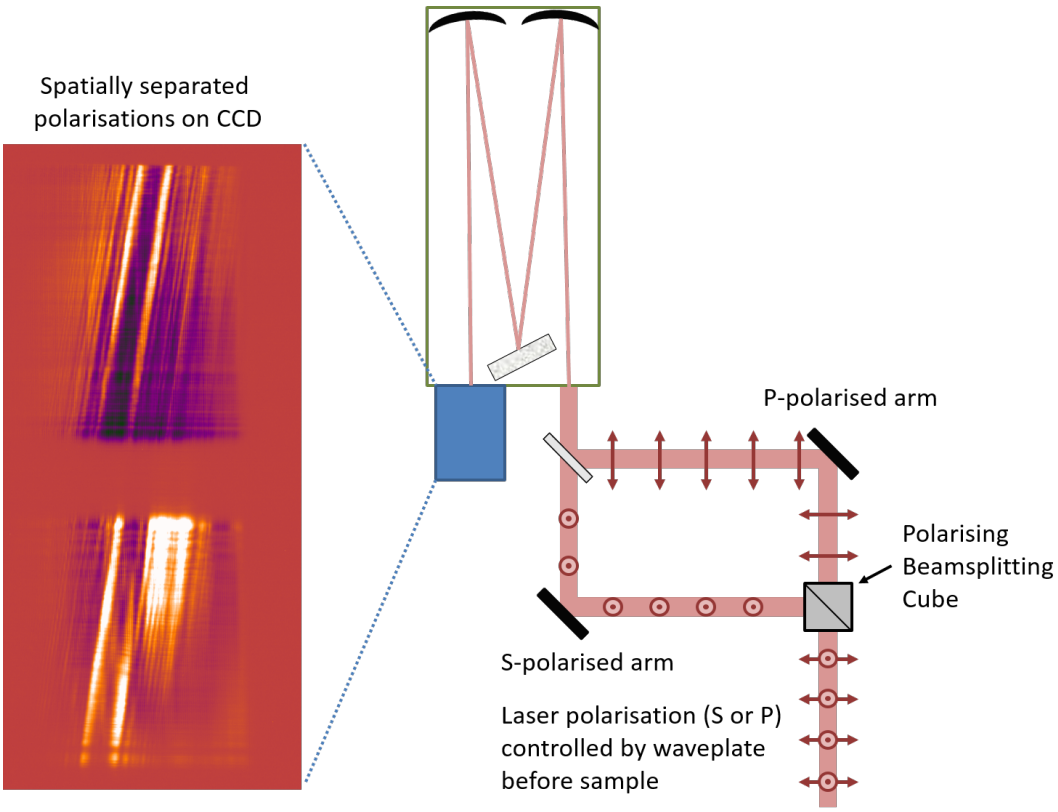

Figure 6.5: Sketch of modifications that were performed to the probe line before the spectrometer to investigate polarisation changes in lithium niobate. Laser polarisation was controlled using a half-wave plate placed before the sample. Depending on the incident polarisation, the probe will propagate down one of the arms and signal will only appear in the other if there is a change in polarisation caused by the $LiNbO_3$ crystal.

the S-polarised arm if there is a modification in the state of polarisation caused by the interactions within the lithium niobate.

This method provides a clearer indication of the state of polarisation of the probe and experimentally obtained images are shown in figure 6.6. There are a few key observations to highlight in this data. Firstly, as the probe has initial P-polarisation, signal does not appear in the S-arm until the transmission begins to drop in the P-polarised arm, indicating a complete rotation in the polarisation in the probe from S to P. Secondly, the initial oscillation in the transmission that varies between ±20% with a period of between 50 ps to 60 ps. Finally the much stronger drop in transmission with a period of around 300 ps where the signal drops to around 30% of the normal probe transmission through the sample. To identify the origin of these oscillations, the lithium niobate sample was replaced with one of the aerogel samples previously discussed in chapter 3. Here the arrival of both prompt X-rays/electrons and protons can be identified by the step like opacity features generated by the interaction of X-rays/electrons and protons. This can be directly compared to the $LiNbO_3$ sample. An overlay of the two lineouts taken at the same depth is shown in figure 6.7, this indicates that the initial high frequency oscillations are started by the arrival of the prompt X-ray/electrons from the TNSA interaction whereas the larger rotation in polarisation is initiated by the protons.

6.2.2 Electron/X-ray Contribution & Crystal Rotation

Placing 1 mm of Aluminium in front of the crystal to filter the proton energies resulted in a much smaller contribution of the proton signal leaving the initial high frequency component, this is shown in the top plot of figure 6.9. A similar signal is obtained by rotating the crystal as shown in figure 6.8. As outlined

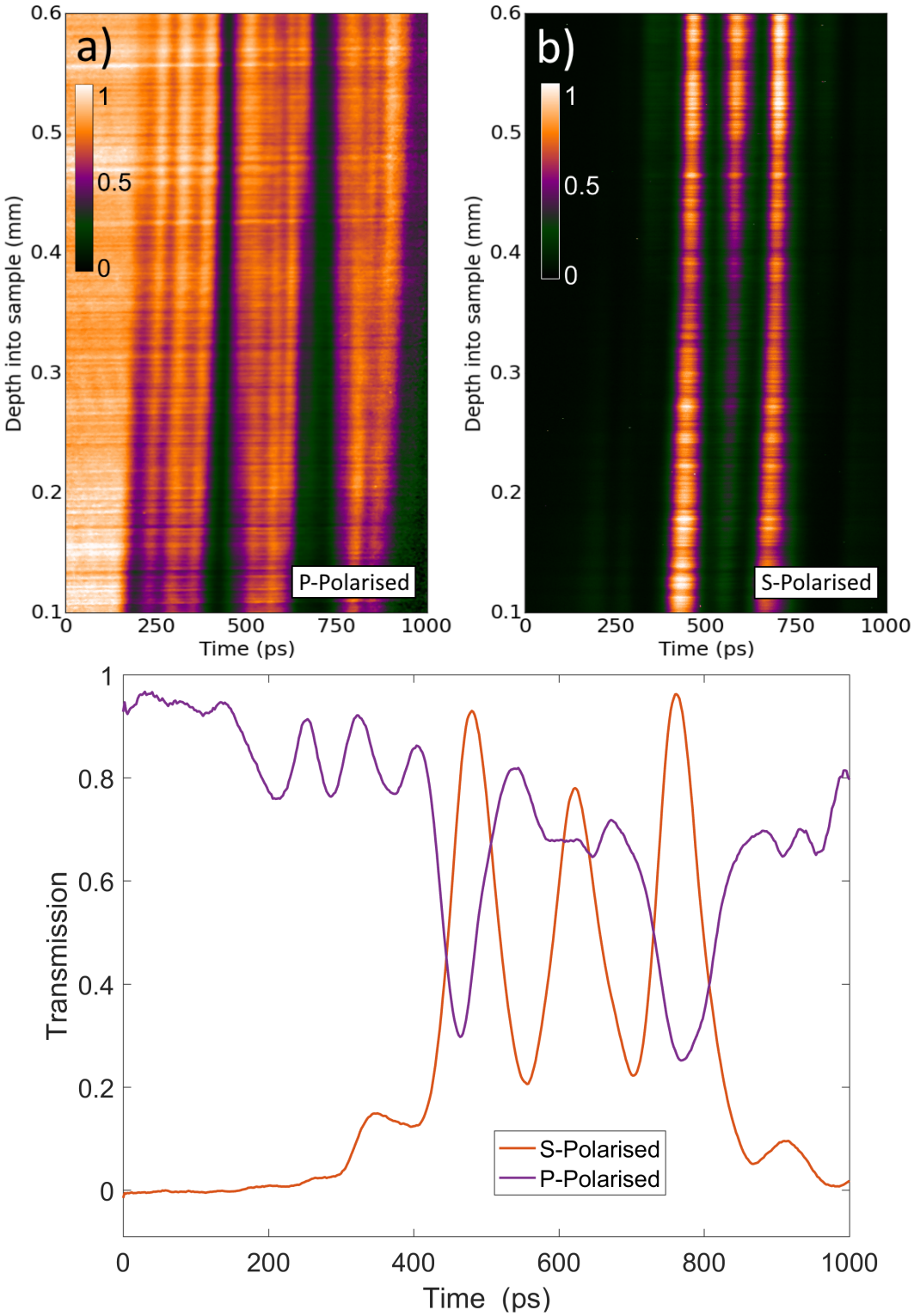

Figure 6.6: Optically streaked data showing radiation induced dynamics in Lithium Niobate with signal from (**a**) the P-polarised and (**b**) S-polarised arm. Lineout shows comparison in the two normalised signals taken at a depth of 470 µm in the sample.

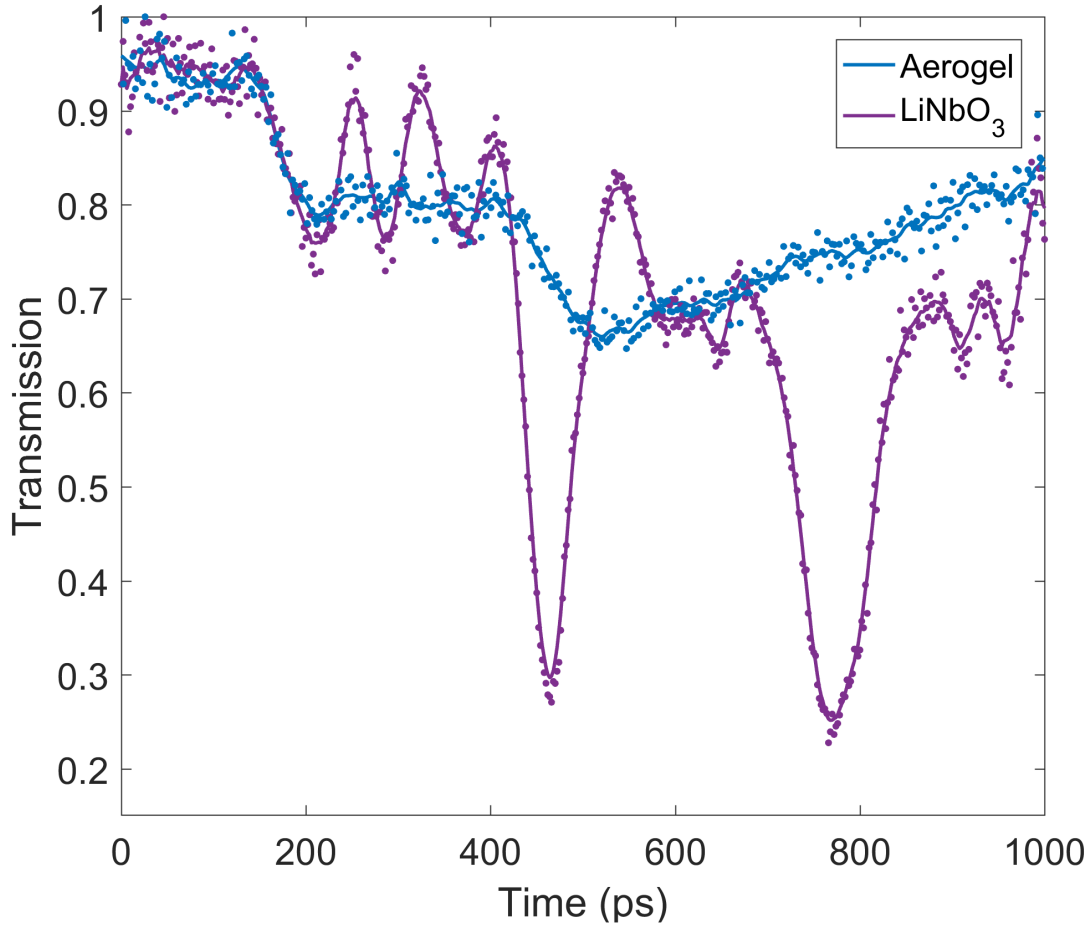

Figure 6.7: Optical streaking data for lithium niobate superimposed on data from an aerogel sample. This indicates that the small oscillations are initiated by the electrons and X-rays. The much larger and slower oscillations begin with the arrival of the proton pulse.

earlier in this chapter, the electro optic effect in lithium niobate has a strong dependence on the orientation of the crystal relative to the applied electric field (radiation direction) and light propagation. For the initial orientation of the crystal as in figure 6.8a, the propagation direction for the radiation was along the axis with the largest electro-optic coefficient ($\approx 30.8\,\mathrm{pm\,V^{-1}}$) resulting in the smallest electric field required to induce a phase change. Rotating the crystal so that the radiation is along another direction results in an increased field required to induce the same effect, possibly explaining the disappearance of the proton signal in the rotated $LiNbO_3$.

In addition to direct interaction with prompt X-rays and electrons. Intense laser-solid interactions are known to produce significant electromagnetic pulses [110, 111], with EMP amplitudes of hundreds of kilovolts per metre being directly measured [112]. These pulses, which result from high energy electrons hitting the wall of the target chamber can last hundreds of nanoseconds. While this has never been directly measured on the TARANIS system, the initial high frequency oscillations could originate from the EMP. So far we have observed the oscillations to still be present in the sample for several nanoseconds, much longer than the interaction time for the radiation. To conclusively investigate this, EMP sensors would need to be placed within the chamber to record the signal from EMP alongside the response of the lithium niobate. This is something that will be examined in future experiments.

6.3 Summary

This chapter has outlined an investigation into the polarisation rotation phenomena exhibited by lithium niobate crystals under irradiation. While this is still very much a work in progress, there has been a clear observation in changes

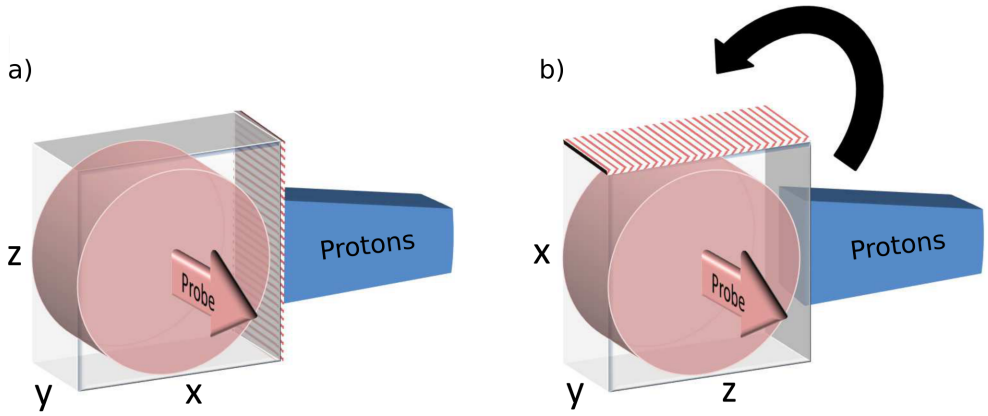

Figure 6.8: Schematic of $LiNbO_3$ sample geometry with crystal axis orientations labelled (x, y, z) Rotation of the crystal refers to a anticlockwise rotation of 90°performed along the axis of the probe beam. The radiation now travels parallel to the crystal z-axis.

in the state of polarisation of a probe as it passes through irradiated $LiNbO_3$. An hypothesis for the origin of this effect lies in the piezoelectric and electro-optic nature of the crystal. Electric fields induced through the interaction of these two types of radiation could lead to a deformation in the crystal, inducing a voltage in the material and activating the electro-optic properties. The picosecond timescale oscillations then could be a result of the strong piezoelectric response of lithium niobate. As the initial radiation initially deforms the crystal, the material will then expand and contract, inducing an electric field as it returns to an equilibrium state. Initial high frequency, low amplitude oscillations are seen to begin on arrival of the prompt electrons, followed by significantly larger oscillations induced by the proton pulse. Rotating the crystal so that the radiation travels down a less preferable direction however only appears to have affected the proton signal as the high frequency component remains. It is clear that significantly more investigation is required to confirm the origin of this effect. Ideas for future experiments will be discussed in chapter 7 alongside other possible avenues of research relating to the other chapters in this thesis.

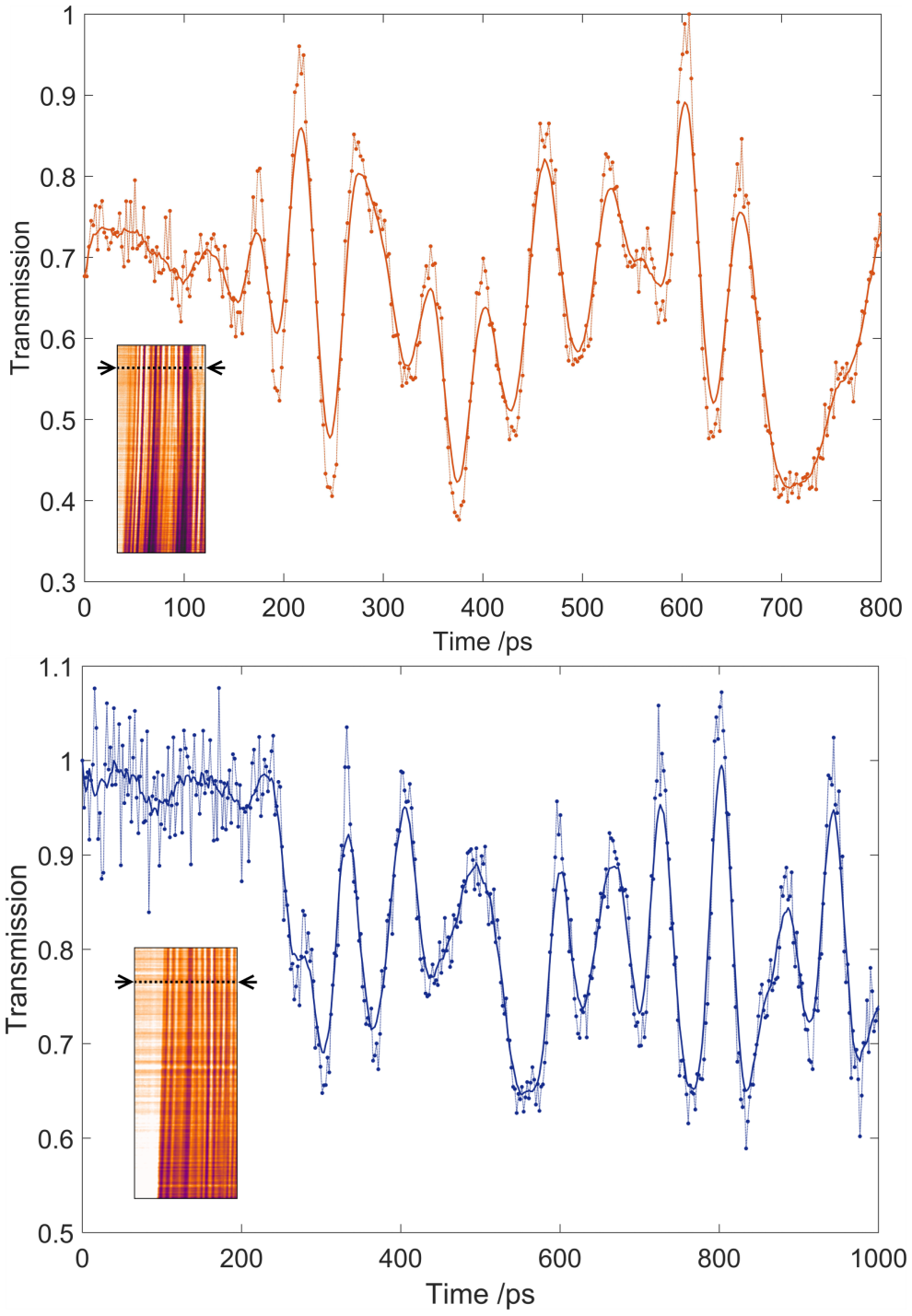

Figure 6.9: Experimentally obtained optical streak of ionisation dynamics in lithium niobate. **Top** Protons with energies up to 10 MeV have been blocked using a 1 mm thick piece of aluminium placed before the crystal. **Bottom** The crystal has been rotated anticlockwise around the probe axis as shown in figure 6.8.

Chapter 7

Conclusions and Outlook

This thesis has presented experimental results and observations of ionisation dynamics in a wide variety of samples. To recap, this chapter will summarise the main results and provide some outlook to future investigations within this area of research.

In chapter 3 the first experimental measurements of the proton pulse duration were performed through observation of a proton-induced opacity in SiO_2. The optical streaking technique was used to perform transient absorption spectroscopy in order to determine the lifetime of excited electrons in the conduction band. The proton pulse duration measurement in SiO_2 was enabled through the formation of self trapped excitons forming an ultrafast decay pathway for the excited electrons on the order of 150 fs. Proton pulses as short as 3.5 ± 0.7 ps were measured. Investigations on inhibiting the rapid diffusion of electrons generated by the steep energy gradients of the proton tracks was studied using silica aerogel samples. A relation between the density of the aerogel and recovery time of the opacity was found, whereby increasing the density decreased the lifetime of opacity in the sample as the electrons were less restricted in the

diffusion.

Chapter 4 introduced the concept of defects in the role of the recovery of opacity in borosilicate glass. The opacity was found to exist much longer than the previously observed proton pulse duration in SiO_2 with a decay constant of 550 ps. Previous photoexcitation experiments suggest that this long recovery can be interpreted as being due to occupied interstitial energy levels which prevent the rapid relaxation of the excited electron population.

Short-pulsed ion radiolysis of water was investigated in chapter 5. Here the absorption band of solvated electrons was probed directly using the 1053 nm probe to study their formation after interaction with ionising radiation. Significant difference in the formation times were observed when the water was irradiated with electron/X-ray radiation and protons. Classical MD simulations indicate the high LET of the proton radiation results in the formation of nanometre scale cavities around the proton track in the Bragg region. These cavities inhibit the formation of solvated electrons due to both the high initial kinetic energy imparted to the water molecules and the bulk movement of the water away from the proton track resulting in a delay in the trapping of free electrons generated by the ionising radiation and hence the beginning of the solvation process.

Chapter 6 provided the first look at alternative investigations that can be performed using the optical streaking technique. Instead of transient absorption spectroscopy of an induced opacity, changes in the polarisation state of the probe were examined due to radiation induced dynamics within lithium niobate. The polarisation of a probe pulse was observed to rotate between S and P states with a period of 130 ps due to proton interactions with the crystal. Additionally, a much smaller, high frequency oscillation was induced by the prompt electron and X-ray signal. Rotating the lithium niobate crystal essentially eliminated

the large oscillations induced by the protons, leaving behind the high frequency component – similar optical streaks were obtained using aluminium to filter the proton signal.

7.1 Suggestions for Future Work

The optical streaking technique has inherent flexibility which would enable further study of samples with only minor modifications to the experimental procedure. One change that would benefit the majority of investigations would be the move to femtosecond scale probe durations to observe radiation dynamics within the rising edge of the proton pulse. Moving to shorter probe pulse durations, either at other laser facilities or the planned TARANIS-X (10 fs) upgrade at QUB would additionally permit much higher resolution of features within the optical streak as the current major limit is the fully compressed 470 fs probe duration provided by TARANIS.

Investigation of a larger range of samples would be beneficial in understanding the material response that has been observed so far. For example, fused silica samples with controlled levels of impurities would enable direct examination of the effect of defect concentrations on a high-purity material. Additionally, studying different cuts of lithium niobate crystals could broaden understanding of the role of crystal orientation on polarisation dynamics.

As discussed in chapter 4, the energy level structure of a multicomponent glass such as soda-lime or BK7 contain many interstitial levels created by defects and electron trapping. Altering the wavelength of the probe through frequency conversion would enable specific absorption bands to be examined for various excited species or to closely examine exciton formation [113]. Frequency con-

version would also apply to the investigation of radiolysis in water to examine specific radiation products, such as of H_2 (400–500 nm), H_2O_2 and hydroxyl radicals at 300–400 nm [114].

References

[1] P. Maine, D. Strickland, P. Bado, M. Pessot, and G. Mourou, "Generation of ultrahigh peak power pulses by chirped pulse amplification," *IEEE Journal of Quantum electronics*, vol. 24, no. 2, pp. 398–403, 1988.

[2] G. A. Mourou, C. Barty, and M. D. Perry, "Ultrahigh-intensity laser: physics of the extreme on a tabletop," tech. rep., Lawrence Livermore National Lab., CA (United States), 1997.

[3] S. Backus, C. G. Durfee III, M. M. Murnane, and H. C. Kapteyn, "High power ultrafast lasers," *Review of scientific instruments*, vol. 69, no. 3, pp. 1207–1223, 1998.

[4] G. A. Mourou, T. Tajima, and S. V. Bulanov, "Optics in the relativistic regime," *REVIEWS OF MODERN PHYSICS*, vol. 78, pp. 309–371, APR-JUN 2006.

[5] T. Brabec and F. Krausz, "Intense few-cycle laser fields: Frontiers of nonlinear optics," *Reviews of Modern Physics*, vol. 72, no. 2, p. 545, 2000.

[6] C. Rödel, D. an der Brügge, J. Bierbach, M. Yeung, T. Hahn, B. Dromey, S. Herzer, S. Fuchs, A. G. Pour, E. Eckner, *et al.*, "Harmonic generation from relativistic plasma surfaces in ultrasteep plasma density gradients," *Physical review letters*, vol. 109, no. 12, p. 125002, 2012.

[7] B. Dromey, M. Zepf, A. Gopal, K. Lancaster, M. Wei, K. Krushelnick, M. Tatarakis, N. Vakakis, S. Moustaizis, R. Kodama, *et al.*, "High harmonic generation in the relativistic limit," *Nature physics*, vol. 2, no. 7, p. 456, 2006.

[8] A. Appleby and H. A. Schwarz, "Radical and molecular yields in water irradiated by. gamma.-rays and heavy ions," *The Journal of Physical Chemistry*, vol. 73, no. 6, pp. 1937–1941, 1969.

[9] J. A. LaVerne and H. Yoshida, "Production of the hydrated electron in the radiolysis of water with helium ions," *The Journal of Physical Chemistry*, vol. 97, no. 41, pp. 10720–10724, 1993.

[10] J. A. LaVerne, "Track effects of heavy ions in liquid water," *Radiation research*, vol. 153, no. 5, pp. 487–496, 2000.

[11] N. Chitose, Y. Katsumura, Z. Zuo, M. Domae, K. Ishigure, and T. Murakami, "Radiolysis of aqueous solutions with pulsed helium ion beams yield of (scn) 2-formed by scavenging oh as a function of scn-concentration," *Journal of the Chemical Society, Faraday Transactions*, vol. 93, no. 22, pp. 3939–3944, 1997.

[12] G. Baldacchino, "Pulse radiolysis in water with heavy-ion beams. a short review," *Radiation Physics and Chemistry*, vol. 77, no. 10, pp. 1218–1223, 2008.

[13] P. Baudrenghien and T. Mastoridis, "Longitudinal emittance blowup in the large hadron collider," *Nuclear Instruments and Methods in Physics Research Section A: Accelerators, Spectrometers, Detectors and Associated Equipment*, vol. 726, pp. 181–190, 2013.

[14] K. Krushelnick, E. Clark, Z. Najmudin, M. Salvati, M. Santala, M. Tatarakis, A. Dangor, V. Malka, D. Neely, R. Allott, *et al.*, "Multi-mev ion production from high-intensity laser interactions with underdense plasmas," *Physical review letters*, vol. 83, no. 4, p. 737, 1999.

[15] A. Robinson, M. Zepf, S. Kar, R. Evans, and C. Bellei, "Radiation pressure acceleration of thin foils with circularly polarized laser pulses," *New journal of Physics*, vol. 10, no. 1, p. 013021, 2008.

[16] M. Borghesi, "Laser-driven ion acceleration: State of the art and emerging mechanisms," *Nuclear Instruments and Methods in Physics Research Section A: Accelerators, Spectrometers, Detectors and Associated Equipment*, vol. 740, pp. 6–9, 2014.

[17] E. Clark, K. Krushelnick, M. Zepf, F. Beg, M. Tatarakis, A. Machacek, M. Santala, I. Watts, P. Norreys, and A. Dangor, "Energetic heavy-ion and proton generation from ultraintense laser-plasma interactions with solids," *Physical review letters*, vol. 85, no. 8, pp. 1654–1657, 2000.

[18] A. Maksimchuk, S. Gu, K. Flippo, D. Umstadter, and V. Y. Bychenkov, "Forward ion acceleration in thin films driven by a high-intensity laser," *Physical Review Letters*, vol. 84, no. 18, p. 4108, 2000.

[19] A. Subiel, V. Moskvin, G. H. Welsh, S. Cipiccia, D. Reboredo, P. Evans, M. Partridge, C. DesRosiers, M. P. Anania, A. Cianchi, *et al.*, "Dosimetry of very high energy electrons (vhee) for radiotherapy applications: using radiochromic film measurements and monte carlo simulations," *Physics in Medicine & Biology*, vol. 59, no. 19, p. 5811, 2014.

[20] S. Mangles, "An overview of recent progress in laser wakefield acceleration experiments," *arXiv preprint arXiv:1705.10588*, 2017.

[21] J. Faure, Y. Glinec, A. Pukhov, S. Kiselev, S. Gordienko, E. Lefebvre, J.-P. Rousseau, F. Burgy, and V. Malka, "A laser–plasma accelerator producing monoenergetic electron beams," *Nature*, vol. 431, no. 7008, p. 541, 2004.

[22] C. Geddes, C. Toth, J. Van Tilborg, E. Esarey, C. Schroeder, D. Bruhwiler, C. Nieter, J. Cary, and W. Leemans, "High-quality electron beams from a laser wakefield accelerator using plasma-channel guiding," *Nature*, vol. 431, no. 7008, p. 538, 2004.

[23] O. Lundh, J. Lim, C. Rechatin, L. Ammoura, A. Ben-Ismail, X. Davoine, G. Gallot, J.-P. Goddet, E. Lefebvre, V. Malka, *et al.*, "Few femtosecond, few kiloampere electron bunch produced by a laser–plasma accelerator," *Nature Physics*, vol. 7, no. 3, p. 219, 2011.

[24] A. Einstein, "Emission and absorption of radiation in quantum theory," *Deutch. Phys. Ges.*, vol. 18, pp. 318–323, 1916.

[25] T. H. Maiman, "Stimulated optical radiation in ruby," 1960.

[26] T. Tajima and G. Mourou, "Zettawatt-exawatt lasers and their applications in ultrastrong-field physics," *Phys. Rev. ST Accel. Beams*, vol. 5, p. 031301, Mar 2002.

[27] D. Strickland and G. Mourou, "Compression of amplified chirped optical pulses," *Optics communications*, vol. 55, no. 6, pp. 447–449, 1985.

[28] E. Brookner, "Phased-array radars," *Scientific American*, vol. 252, pp. 94–102, Feb. 1985.

[29] M. Perry, "Multilayer dielectric gratings," *Science and Technology Review*, pp. 24–33, 1995.

[30] V. Ginzburg, *The propagation of electromagnetic waves in plasmas*. International series of monographs on electromagnetic waves, Pergamon Press, 1970.

[31] W. Kruer, *The Physics of Laser Plasma Interactions*. Frontiers in physics, Avalon Publishing, 2003.

[32] F. Brunel, "Not-so-resonant, resonant absorption," *Physical Review Letters*, vol. 59, no. 1, pp. 52–55, 1987.

[33] P. Gibbon, *Short pulse laser interactions with matter*. Imperial College Press London, 2005.

[34] V. Malka, S. Fritzler, E. Lefebvre, M.-M. Aleonard, F. Burgy, J.-P. Chambaret, J.-F. Chemin, K. Krushelnick, G. Malka, S. Mangles, *et al.*, "Electron acceleration by a wake field forced by an intense ultrashort laser pulse," *Science*, vol. 298, no. 5598, pp. 1596–1600, 2002.

[35] S. Gitomer, R. Jones, F. Begay, A. Ehler, J. Kephart, and R. Kristal, "Fast ions and hot electrons in the laser–plasma interaction," *Physics of Fluids (1958-1988)*, vol. 29, no. 8, pp. 2679–2688, 1986.

[36] S. Wilks, A. Langdon, T. Cowan, M. Roth, M. Singh, S. Hatchett, M. Key, D. Pennington, A. MacKinnon, and R. Snavely, "Energetic proton generation in ultra-intense laser–solid interactions," *Physics of Plasmas (1994-present)*, vol. 8, no. 2, pp. 542–549, 2001.

[37] K. Markey, "Laser-ion acceleration–towards table top accelerators,"

[38] P. Mora, "Plasma expansion into a vacuum.," *Physical review letters*, vol. 90, p. 185002, May 2003.

[39] M. Passoni and M. Lontano, "One-dimensional model of the electrostatic ion acceleration in the ultraintense laser-solid interaction," *Laser and Particle Beams*, vol. 22, no. 2, pp. 163–169, 2004.

[40] A. Macchi, M. Borghesi, and M. Passoni, "Ion acceleration by superintense laser-plasma interaction," *Reviews of Modern Physics*, vol. 85, no. 2, p. 751, 2013.

[41] T. Cowan, J. Fuchs, H. Ruhl, A. Kemp, P. Audebert, M. Roth, R. Stephens, I. Barton, A. Blazevic, E. Brambrink, *et al.*, "Ultralow emittance, multi-mev proton beams from a laser virtual-cathode plasma accelerator," *Physical Review Letters*, vol. 92, no. 20, p. 204801, 2004.

[42] D. Jung, *Ion acceleration from relativistic laser nano-target interaction*. PhD thesis, lmu, 2012.

[43] L. Yin, B. Albright, B. Hegelich, and J. Fernández, "Gev laser ion acceleration from ultrathin targets: The laser break-out afterburner," *Laser and Particle Beams*, vol. 24, no. 02, pp. 291–298, 2006.

[44] L. Yin, B. Albright, D. Jung, R. Shah, S. Palaniyappan, K. Bowers, A. Henig, J. Fern, B. M. Hegelich, *et al.*, "Break-out afterburner ion acceleration in the longer laser pulse length regime," *Physics of Plasmas (1994-present)*, vol. 18, no. 6, p. 063103, 2011.

[45] T. Esirkepov, M. Borghesi, S. Bulanov, G. Mourou, and T. Tajima, "Highly efficient relativistic-ion generation in the laser-piston regime," *Physical review letters*, vol. 92, no. 17, p. 175003, 2004.

[46] M. Hegelich, S. Karsch, G. Pretzler, D. Habs, K. Witte, W. Guenther, M. Allen, A. Blazevic, J. Fuchs, J. Gauthier, *et al.*, "Mev ion jets from short-pulse-laser interaction with thin foils," *Physical review letters*, vol. 89, no. 8, p. 085002, 2002.

[47] A. Macchi, F. Cattani, T. V. Liseykina, and F. Cornolti, "Laser acceleration of ion bunches at the front surface of overdense plasmas," *Physical review letters*, vol. 94, no. 16, p. 165003, 2005.

[48] A. Lagzda, "Radiotherapy studies with very high energy electrons (vhee)." University of Manchester Accelerator group Christmas meeting, 2015.

[49] G. F. Brand, I. S. Falconer, M. I. Large, I. M. Sefton, J. Ulricks, G. C. Vorlicek, and M. M. Winn, *Atoms and Nuclei*. University of Sydney, 3 ed., 1993.

[50] ICRU, "Stopping powers and ranges for protons and alpha particles.," *Technical Report 60, International Commission on Radiation Units and Measurements*, 1993.

[51] W. D. Newhauser and R. Zhang, "The physics of proton therapy," *Physics in medicine and biology*, vol. 60, no. 8, p. R155, 2015.

[52] S. Tavernier, "Interactions of particles in matter," in *Experimental techniques in nuclear and particle physics*, pp. 23–53, Springer, 2009.

[53] J. F. Ziegler, M. D. Ziegler, and J. P. Biersack, "Srim–the stopping and range of ions in matter (2010)," *Nuclear Instruments and Methods in Physics Research Section B: Beam Interactions with Materials and Atoms*, vol. 268, no. 11, pp. 1818–1823, 2010.

[54] E. Podgorsak, "Radiation oncology physics," 2005.

[55] N. Itoh, D. M. Duffy, S. Khakshouri, and A. M. Stoneham, "Making tracks: electronic excitation roles in forming swift heavy ion tracks.," *Journal of physics. Condensed matter : an Institute of Physics journal*, vol. 21, p. 474205, Nov 2009.

[56] T. Dzelzainis, G. Nersisyan, D. Riley, L. Romagnani, H. Ahmed, A. Bigongiari, M. Borghesi, D. Doria, B. Dromey, M. Makita, *et al.*, "The taranis laser: A multi-terawatt system for laser-plasma investigations," *Laser and Particle Beams*, vol. 28, no. 03, pp. 451–461, 2010.

[57] D. Polli, D. Brida, S. Mukamel, G. Lanzani, and G. Cerullo, "Effective temporal resolution in pump-probe spectroscopy with strongly chirped pulses," *Physical Review A*, vol. 82, no. 5, p. 053809, 2010.

[58] I. Walmsley, L. Waxer, and C. Dorrer, "The role of dispersion in ultrafast optics," *Review of Scientific Instruments*, vol. 72, no. 1, pp. 1–29, 2001.

[59] E. Wigner, "On the quantum correction for thermodynamic equilibrium," *Physical review*, vol. 40, no. 5, p. 749, 1932.

[60] M. Taylor, M. Coughlan, G. Nersisyan, L. Senje, D. Jung, M. Borghesi, D. Riley, C. Lewis, M. Zepf, and B. Dromey, "Probing ultrafast proton induced dynamics in transparent dielectrics." 2016.

[61] P. Audebert, P. Daguzan, A. Dos Santos, J. Gauthier, J. Geindre, S. Guizard, G. Hamoniaux, K. Krastev, P. Martin, G. Petite, *et al.*, "Space-time observation of an electron gas in si o 2," *Physical review letters*, vol. 73, no. 14, p. 1990, 1994.

[62] H. Hosono, H. Kawazoe, and N. Matsunami, "Experimental evidence for frenkel defect formation in amorphous sio 2 by electronic excitation," *Physical Review Letters*, vol. 80, no. 2, p. 317, 1998.

[63] D. Grojo, M. Gertsvolf, S. Lei, T. Barillot, D. Rayner, and P. Corkum, "Exciton-seeded multiphoton ionization in bulk sio 2," *Physical Review B*, vol. 81, no. 21, p. 212301, 2010.

[64] S. Guizard, P. Martin, P. Daguzan, G. Petite, P. Audebert, J. Geindre, A. Dos Santos, and A. Antonnetti, "Contrasted behaviour of an electron gas in *mgo*, *al*2*o*3 and *sio*2," *EPL (Europhysics Letters)*, vol. 29, no. 5, p. 401, 1995.

[65] O. Osmani, H. Lebius, B. Rethfeld, and M. Schleberger, "Energy dissipation in insulators induced by swift heavy ions: A parameter study," *Laser and Particle Beams*, vol. 28, no. 02, pp. 229–234, 2010.

[66] O. Osmani, N. Medvedev, M. Schleberger, and B. Rethfeld, "Energy dissipation in dielectrics after swift heavy-ion impact: a hybrid model," *Physical Review B*, vol. 84, no. 21, p. 214105, 2011.

[67] A. Steinhoff, M. Florian, M. Rösner, G. Schönhoff, T. O. Wehling, and F. Jahnke, "Excitons versus electron-hole plasma in monolayer transition metal dichalcogenide semiconductors," *arXiv preprint arXiv:1705.05202*, 2017.

[68] A. Ferrari, P. R. Sala, A. Fasso, J. Ranft, O. Europenne, P. La, R. Nuclaire, A. Ferrari, P. R. Sala, A. Fass, and J. Ranft, "Fluka: a multi-particle transport code," in *CERN 2005-10 (2005), INFN/TC 05/11, SLAC-R-773*.

[69] T. Bhlen, F. Cerutti, M. Chin, A. Fass, A. Ferrari, P. Ortega, A. Mairani, P. Sala, G. Smirnov, and V. Vlachoudis, "The fluka code: Developments and challenges for high energy and medical applications," *Nuclear Data Sheets*, vol. 120, no. Supplement C, pp. 211 – 214, 2014.

[70] S. Guizard, P. Martin, G. Petite, P. D'Oliveira, and P. Meynadier, "Time-resolved study of laser-induced colour centres in," *Journal of Physics: Condensed Matter*, vol. 8, no. 9, p. 1281, 1996.

[71] J. McMurry, *Organic Chemistry with Biological Applications*. Cengage Learning, 2014.

[72] J. Greer, A. Korkin, and J. Labanowski, *Nano and Giga Challenges in Microelectronics*. Elsevier Science, 2003.

[73] G. Pacchioni, L. Skuja, and D. Griscom, *Defects in SiO2 and Related Dielectrics: Science and Technology*. Nato Science Series II:, Springer Netherlands, 2012.

[74] K. Tanimura, T. Tanaka, and N. Itoh, "Creation of quasistable lattice defects by electronic excitation in si o 2," *Physical review letters*, vol. 51, no. 5, p. 423, 1983.

[75] Y.-L. He and T. Xie, "Advances of thermal conductivity models of nanoscale silica aerogel insulation material," *Applied Thermal Engineering*, vol. 81, pp. 28–50, 2015.

[76] J. L. Gurav, I.-K. Jung, H.-H. Park, E. S. Kang, and D. Y. Nadargi, "Silica aerogel: synthesis and applications," *Journal of Nanomaterials*, vol. 2010, p. 23, 2010.

[77] R. Ciriminna, A. Fidalgo, V. Pandarus, F. Béland, L. M. Ilharco, and M. Pagliaro, "The sol–gel route to advanced silica-based materials and recent applications," *Chemical reviews*, vol. 113, no. 8, pp. 6592–6620, 2013.

[78] Schott, *BK7 Technical Safety Information*, Mar 2015. Rev. 5.

[79] F. Korte, S. Adams, A. Egbert, C. Fallnich, A. Ostendorf, S. Nolte, M. Will, J. P. Ruske, B. Chichkov, and A. Tuennermann, "Sub-diffraction limited structuring of solid targets with femtosecond laser pulses.," *Optics express*, vol. 7, pp. 41–9, Jul 2000.

[80] U. Natura and D. Ehrt, "Formation of radiation defects in silicate and borosilicate glasses caused by uv lamp and excimer laser irradiation," *GLASS SCIENCE AND TECHNOLOGY-FRANKFURT AM MAIN-*, vol. 72, pp. 295–301, 1999.

[81] D. Ehrt and P. Ebeling, "Radiation defects in borosilicate glasses," *Glass Technology-European Journal of Glass Science and Technology Part A*, vol. 44, no. 2, pp. 46–49, 2003.

[82] A. Horn, E. Kreutz, and R. Poprawe, "Ultrafast time-resolved photography of femtosecond laser induced modifications in bk7 glass and fused silica," *Applied Physics A*, vol. 79, no. 4-6, pp. 923–925, 2004.

[83] B. T. Do, M. C. Phillips, P. A. Miller, M. W. Kimmel, J. Britsch, and S.-H. Cho, "Properties of optical breakdown in bk7 glass induced by an extended-cavity femtosecond laser oscillator.," *Optics express*, vol. 17, pp. 2739–55, Feb 2009.

[84] E. W. Kreutz, A. Horn, and R. Poprawe, "Electron excitation in glasses and sapphire followed by time-and space-measuring tools," in *European Symposium on Optics and Photonics for Defence and Security*, pp. 239–244, International Society for Optics and Photonics, 2004.

[85] A. R. Bayly, "Optical properties of ion bombarded silica glass," *Radiation Effects*, vol. 18, no. 1-2, pp. 111–118, 1973.

[86] T. Van Dillen, M. Brongersma, E. Snoeks, and A. Polman, "Activation energy spectra for annealing of ion irradiation induced defects in silica

glasses," *Nuclear Instruments and Methods in Physics Research Section B: Beam Interactions with Materials and Atoms*, vol. 148, no. 1, pp. 221–226, 1999.

[87] C. Flynn, *Point defects and diffusion*. International series of monographs on physics, Clarendon Press, 1972.

[88] S. Elliott, *Physics of amorphous materials*. Longman Scientific & Technical, 1990.

[89] C. Kittel, *Introduction to Solid State Physics*. Wiley, 2004.

[90] T. Husband, "The sweet science of candymaking," *ChemMatters, October and November*, no. 2014, pp. 5–8, 2014.

[91] M. I. Ojovan and W. E. Lee, "Topologically disordered systems at the glass transition," *Journal of Physics: Condensed Matter*, vol. 18, no. 50, p. 11507, 2006.

[92] S. McKeever, *Thermoluminescence of Solids*. Cambridge University Press, 1985.

[93] N. F. Mott and E. A. Davis, *Electronic processes in non-crystalline materials*. OUP Oxford, 2012.

[94] R. A. Clark, *Intrinsic dosimetry: properties and mechanisms of thermoluminescence in commercial borosilicate glass*. PhD thesis, University of Missouri–Columbia, 2012.

[95] D. Griscom, G. Sigel Jr, and R. J. Ginther, "Defect centers in a pure-silica-core borosilicate-clad optical fiber: Esr studies," *Journal of Applied Physics*, vol. 47, no. 3, pp. 960–967, 1976.

[96] I. A. Shkrob and V. Tarasov, "On the structure of trapped holes in borosilicates," *The Journal of Chemical Physics*, vol. 113, no. 23, pp. 10723–10732, 2000.

[97] W. Shockley and W. Read Jr, "Statistics of the recombinations of holes and electrons," *Physical review*, vol. 87, no. 5, p. 835, 1952.

[98] G. Petite, P. Daguzan, S. Guizard, and P. Martin, "Ultrafast processes in laser irradiated wide bandgap insulators," *Applied surface science*, vol. 109, pp. 36–42, 1997.

[99] E. J. Hart and J. Boag, "Absorption spectrum of the hydrated electron in water and in aqueous solutions," *Journal of the American Chemical Society*, vol. 84, no. 21, pp. 4090–4095, 1962.

[100] B. C. Garrett, D. A. Dixon, D. M. Camaioni, D. M. Chipman, M. A. Johnson, C. D. Jonah, G. A. Kimmel, J. H. Miller, T. N. Rescigno, P. J. Rossky, *et al.*, "Role of water in electron-initiated processes and radical chemistry: Issues and scientific advances," *Chemical Reviews*, vol. 105, no. 1, pp. 355–390, 2005.

[101] J. A. Laverne, I. Stefani, and S. M. Pimblott, "Hydrated electron yields in the heavy ion radiolysis of water.," *The journal of physical chemistry. A*, vol. 109, pp. 9393–401, Oct 2005.

[102] F.-Y. Jou and G. R. Freeman, "Temperature and isotope effects on the shape of the optical absorption spectrum of solvated electrons in water," *Journal of Physical Chemistry*, vol. 83, no. 18, pp. 2383–2387, 1979.

[103] J. W. T. Spinks and R. J. Woods, "An introduction to radiation chemistry," 1990.

[104] A. V. Yakubovich, E. Surdutovich, and A. V. Solovyov, "Thermomechanical damage of nucleosome by the shock wave initiated by ion passing through liquid water," *Nuclear Instruments and Methods in Physics Research Section B: Beam Interactions with Materials and Atoms*, vol. 279, pp. 135–139, 2012.

[105] E. Surdutovich, A. V. Yakubovich, and A. V. Solov'yov, "Biodamage via shock waves initiated by irradiation with ions.," *Scientific reports*, vol. 3, p. 1289, 2013.

[106] A. M. Prokhorov and Y. S. Kuz'minov, *Physics and chemistry of crystalline lithium niobate*. Hilger, 1990.

[107] M. C. Teich and B. Saleh, "Fundamentals of photonics," *Canada, Wiley Interscience*, vol. 3, 1991.

[108] C. C. Davis, *Lasers and Electro-optics: Fundamentals and Engineering*. Cambridge University Press, 2 ed., 2014.

[109] Thorlabs, "1200 grooves/mm grating efficiency," 2017.

[110] M. J. Mead, D. Neely, J. Gauoin, R. Heathcote, and P. Patel, "Electromagnetic pulse generation within a petawatt laser target chamber," *Review of scientific instruments*, vol. 75, no. 10, pp. 4225–4227, 2004.

[111] D. Rusby, L. Wilson, R. Gray, R. Dance, N. Butler, D. MacLellan, G. Scott, V. Bagnoud, B. Zielbauer, P. McKenna, *et al.*, "Measurement of the angle, temperature and flux of fast electrons emitted from intense laser–solid interactions," *Journal of Plasma Physics*, vol. 81, no. 5, 2015.

[112] F. Consoli, R. De Angelis, L. Duvillaret, P. Andreoli, M. Cipriani, G. Cristofari, G. Di Giorgio, F. Ingenito, and C. Verona, "Time-resolved absolute measurements by electro-optic effect of giant electromagnetic pulses due to laser-plasma interaction in nanosecond regime," *Scientific reports*, vol. 6, p. 27889, 2016.

[113] C. Zhang, H. Wang, W. Chan, C. Manolatou, and F. Rana, "Absorption of light by excitons and trions in monolayers of metal dichalcogenide mo s 2: Experiments and theory," *Physical Review B*, vol. 89, no. 20, p. 205436, 2014.

[114] D. M. Chipman, "Absorption spectrum of oh radical in water," *The Journal of Physical Chemistry A*, vol. 112, no. 51, pp. 13372–13381, 2008.

Publications

Published

- M. Yeung, B. Dromey, S. Cousens, **M. Coughlan**, S. Rykovanov, C. Rödel, J. Bierbach, S. Kuschel, E. Eckner, M. Förster, G. Paulus & M. Zepf, Polarization gating in relativistic laser-solid interactions. *X-Ray Lasers*, DOI: 10.1007/978-3-319-19521-6_16. 2015.

- M. Yeung, J. Bierbach, E. Eckner, S. Rykovanov, S. Kuschel, A. Sävert, M. Förster, C. Rödel, G.G. Paulus, S. Cousens, **M. Coughlan**, B. Dromey, & M. Zepf, Noncollinear polarization gating of attosecond pulse trains in the relativistic regime, *Phys. Rev. Lett.*, 115:193903, 2015.

- B. Dromey, **M. Coughlan**, L. Senje, M. Taylor, S. Kuschel, B. Villagomez-Bernabe, R. Stefanuik, G. Nersisyan,L. Stella, J. Kohanoff, M. Borghesi, F. Currell, D. Riley, D. Jung, C.-G. Wahlström, C.L.S. Lewis & M. Zepf, Picosecond metrology of laser-driven proton bursts, *Nature Communications*, 7:10642 DOI: 10.1038/ncomms10642, 2016.

- M. Yeung, S. Rykovanov, J. Bierbach, L. Li, E. Eckner, S. Kuschel, A. Woldegeorgis, C. Rödel, A. Svert, G. G. Paulus, **M. Coughlan**, B. Dromey & M. Zepf, Experimental observation of attosecond control over relativistic electron bunches with two-colour fields, *Nature Photonics*, DOI: 10.1038/NPHOTON.2016.239, 2016.

- L. Senje, **M. Coughlan**, D. Jung, M. Taylor, G. Nersisyan, D. Riley, C. L. S. Lewis, O. Lundh, C.-G. Wahlström, M. Zepf, and B. Dromey, Experimental investigation of picosecond dynamics following interactions between laser accelerated protons and water, *Appl. Phys. Lett.*, 110-104102, 2017.

In Preparation

- **M. Coughlan**, L. Senje, M. Taylor, G. Nersisyan, D. Jung, H. Donnelly, N. Breslin, F. Currell, C.-G. Wahlström, L. Stella, J. Kohanoff, M. Zepf and B. Dromey, Ultrafast ion induced dynamics in borosilicate glass, 2017.
- **M. Coughlan**, L. Senje, M. Taylor, G. Nersisyan, D. Jung, H. Donnelly, N. Breslin, F. Currell, M. Zepf, B. Dromey, Electron solvation dynamics in H_2O during ultrafast pulsed-ion radiolysis, 2017.
- **M. Coughlan**, L. Senje, H. Donnelly, N. Breslin, G. Nersisyan, F. Currell, M. Zepf, B. Dromey, Ultrafast dynamics of lithium niobate irradiated by few-picosecond proton pulses, 2017.
- M. Taylor, **M. Coughlan**, G. Nersisyan, L. Senje, D. Jung, M. Borghesi, D. Riley, C.L.S Lewis, M. Zepf, B. Dromey, Probing ultrafast proton induced dynamics in transparent dielectrics, 2016.

Acknowledgements

This thesis has presented a summary of work that I been involved with over the last four years. Although I have produced the words to fill these pages, a thesis is never really the work of a single individual and I have been privileged these last few years to work with and get to know such a great group of people both inside and outside my research group. I would therefore like to take this opportunity to thank everyone that has contributed to my studies at QUB.

First and foremost I would like to thank my supervisor, Dr. Brendan Dromey, for his constant support and advice throughout this Ph.D., and sharing his knowledge relating to designing and implementing experiments, stressing that working sensibly is just as important as working hard. To Prof. Matt Zepf, for initially giving me the opportunity to start this Ph.D and join this group, for his advice and sharing his vast enthusiasm for science. The atmosphere they have created within their research group has made the past four years extremely enjoyable.

I also owe a great debt to Dr. Mark Yeung, whose incredible patience and knowledge enabled me to learn a great deal when on my first experiments starting out as a Ph.D student. I'd also like to thank Dr. Gagik Nersisyan for his tireless work on TARANIS, without his expertise, knowledge and assistance a great deal of the work presented here would just simply not have been possible.

To my fellow group members, both past and present; My special thanks go to Dr. Michael Taylor and Dr. Steven Cousens for their invaluable help over the years and warmly welcoming me when I first joined the group. Many thanks to Hannah Donnelly for her excellent choice of lab music and together with Nicole Breslin for their company during long hours in the lab, in the office and our yearly excursion over to the Ulster Museum. I wish you both the best of luck with the remainder of your studies. Their approach to all aspects of Ph.D life has made my time in the office, on experiments and travelling for conferences very enjoyable.

Also many thanks to Dr. Li Lu, Dr. Daniel Jung, Dr. Lovisa Senje and to the staff and students I have worked with at Queen's and over at the JETI laser system in Jena. I'm also grateful to the EPSRC for their financial support in funding this Ph.D.

Last but definitely not least I would like to thank my family, particularly my mum, who has always supported me in everything that I have done and I would not be who I am today if not for her. And to my father, who is never far from my thoughts and who I very much wish could have seen this work completed.